Calorimetric Efficiency of the DUNE Experiment

Supervisor:

Prof. Alessandro Gabrielli

Co-supervisor:
Dr. Matteo Tenti
Dr. Michele Pozzato

Submitted by:

Francesco Chiapponi

Abstract

The Deep Underground Neutrino Experiment is a long-baseline neutrino experiment which is under construction in the United States. It will be composed of a Near Detector system located a few hundred meters from the neutrino source at Fermilab and a far detector system composed of four multi-kt LArTPCs at Sanford Underground Research Facility in South Dakota.

The experiment will measure the leptonic CP violation phase of the PMNS matrix and discriminate the ordering of neutrino masses. Additional physics goals include detection of neutrinos from supernovae collapse and search for possible proton decay.

One component of the Near detector complex is the System for on-Axis Neutrino Detection apparatus, which includes GRanular Argon for Interaction of Neutrinos, a novel liquid Argon detector that aims at imaging neutrino interactions using scintillation light collected by optical system and read-out by SIPM matrix.

This thesis work aims at studying the GRAIN performances as a homogeneous calorimeter able to measure the energy deposited by charged particles in LAr through scintillation photons emitted along their path inside the vessel. The energy calibration of the liquid argon volume has required the development (and validation) of an efficient software for the detector response simulation to the arrival of scintillation photons. The spatial distribution of the calibration coefficient was analysed, finding a distribution of values peaked at 0.014 ± 0.003 MeV/photons. This fact allowed to consider a unique calibration coefficient for the LAr volume to obtain a preliminary energy resolution for the GRAIN detector.

Acknowledgements

Contents

Introduction

Since their discovery neutrino oscillations have become one of the most direct evidence of the fact that the Standard Model of particle physics is not a complete theory. The complementary use of multiple experimental channels and sources, exploiting either the solar and atmospheric neutrino fluxes or artificial ones produced by nuclear reactors or particle accelerators, has made it possible to determine many of the parameters related to neutrino masses. However, some of them have yet to be determined, such as the ordering of neutrino masses and the potential CP-violating phase of the neutrino mixing matrix, the latter of which would have a profound impact on the whole lepton sector of particle physics.

The Deep Underground Neutrino Experiment (DUNE) will be a next-generation neutrino oscillation Long Baseline accelerator experiment, leveraging innovative detector technologies and the most powerful neutrino beam available at the time of completion.

To achieve its goals, the international DUNE experiment, hosted by the U.S. Department of Energy's Fermi National Accelerator Laboratory (Fermilab) in Illinois, comprises three central components: a new, high-intensity neutrino source generated from a megawatt-class proton accelerator at Fermilab, a massive far detector (FD) situated 1.5km underground at the Sanford Underground Research Facility (SURF) in South Dakota, 1300 km away, and a composite near detector (ND) installed just downstream of the neutrino source.

The Near Detector (ND) complex will be composed of three detectors able to provide complementary information on the neutrino beam and to refine the interaction models that will be necessary to analyse the FD data. The ND will also be capable of conducting searches on neutrino interactions, including a wide range of measurements of neutrino cross sections, studies of nuclear effects, and searches for dark matter, providing high-granularity and resolution.

The System for on-Axis Neutrino Detection (SAND) will be the only one in the ND complex to be fixed in an on-axis position, from which it will monitor the neutrino beam flux. The detector will reuse the magnet and calorimeter from the KLOE experiment. For the inner volume, a system of trackers and an active LAr target is planned. The proposed LAr active target of the ND SAND detector, also known as GRAIN (GRanular Argon for Interaction of Neutrinos), aims to provide fast and granular vertex and track

identification capabilities, together with event energy reconstruction. These tasks will be carried out using only the scintillation light emitted by charged particles.

For this purpose, an optical detection system is being considered with the aim of providing a complete spatial and timing reconstruction of the events with a timescale of a few nanoseconds. Two solutions that are being developed for the optical readout system: the first employs optical lenses to focalise scintillation photons on the camera plane; the second, developed in Bologna, is based on the Coded Aperture Mask technique, in which event reconstruction will be possible through the combination of images from multiple Coded Aperture cameras with different viewpoints. In both cases, event reconstruction will be performed by a reconstruction algorithm based on a combinatorial approach: its output is a 3D neutrino event reconstruction in terms of the probability for each unit voxel of the GRAIN inner volume to be the source of a detected photon.

The aim of this thesis work is the estimation of the calorimetric efficiency of GRAIN using simulated neutrino events data. Such an investigation has not been done yet and will shed light on the effective energy measurement capability of GRAIN. The dissertation is organised as follows:

- Chapter 1 will give an overview of neutrino physics from a theoretical point of view, taking also a look at future prospects.

- Chapter 2 will describe the components and facilities of the DUNE experiment together with its physical objectives.

- Chapter 3 will describe the components of the SAND detector.

- Chapter 4 will describe the photon detection system and the principles of track reconstruction in GRAIN; it will describe the software and data used for the detector response simulations.

- Chapter 5 will outline the principles and features of calorimetric measurements in GRAIN and will present the results of the energy calibration.

Chapter 1

Neutrino Physics

1.1 Standard Model neutrinos

The Standard Model of particles physics is a gauge theory defined by the $SU(3) \times SU(2)_L \times U(1)_Y$ symmetry, with the subscripts L and Y indicating the left chirality of the particles and their hypercharge, respectively.

Whereas the strong sector $SU(3)$ symmetry remains unbroken and therefore is an exact symmetry at any energy level, the electroweak forces undergo spontaneous symmetry breaking via the Higgs mechanism, which reduces the symmetry of the model at low energies to $SU(2)_L \times U(1)_Y \rightarrow U(1)_Q$, with Q being the electric charge.

Figure 1.1 shows how fundamental particles are organised within the Standard Model. They are divided into bosons of spin 1 that mediate the interactions, the spin 0 Higgs boson and the fermions, quarks and leptons, organized in $SU(2)_L$ left-handed (LH) doublets and $U(1)_Y$ right-handed (RH) singlets.

Neutrinos are chargeless leptons that can interact only weakly, either via Neutral Current (NC) or Charged Current (CC) interactions, the first being mediated by Z^0 bosons, and the latter by $W^\pm$ bosons. For a quick overview of the history of neutrino discovery, read Appendix A.

Three types, or *flavours states*, of neutrinos and antineutrinos are currently known: electron-type, muon-type and tau-type (ν_e, ν_μ and ν_τ respectively). They are defined by the charged lepton to which they couple in weak charged-current interactions. Furthermore, the number of left-handed, and thus interacting, flavour neutrinos has been proven to be three. The study of the decay width of the Z^0 produced at LEP in e^+e^- collisions showed that the number of light neutrinos coupled to the neutral weak boson is [23]:

$$N_\nu = \frac{\Gamma_{inv}}{\Gamma_{\bar{\nu}\nu}} = 2.984 \pm 0.008$$

Flavour neutrino states take part in weak CC and NC processes described, to an
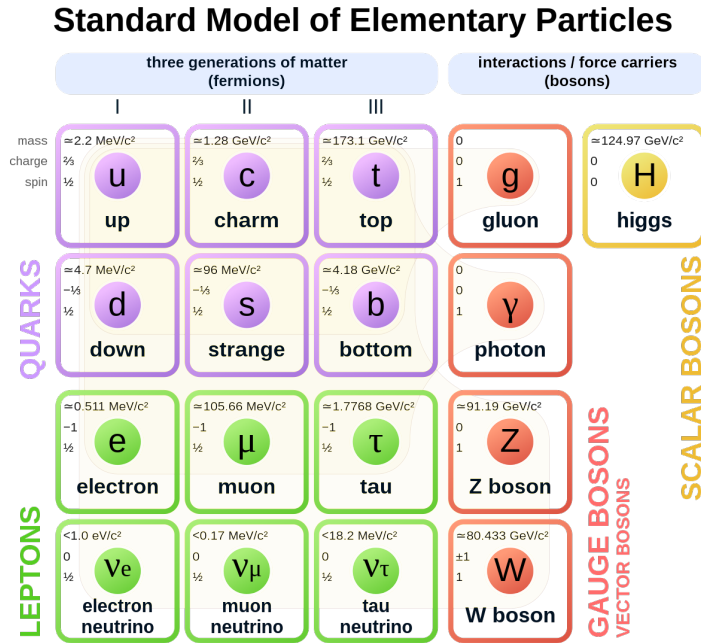
Standard Model of Elementary Particles

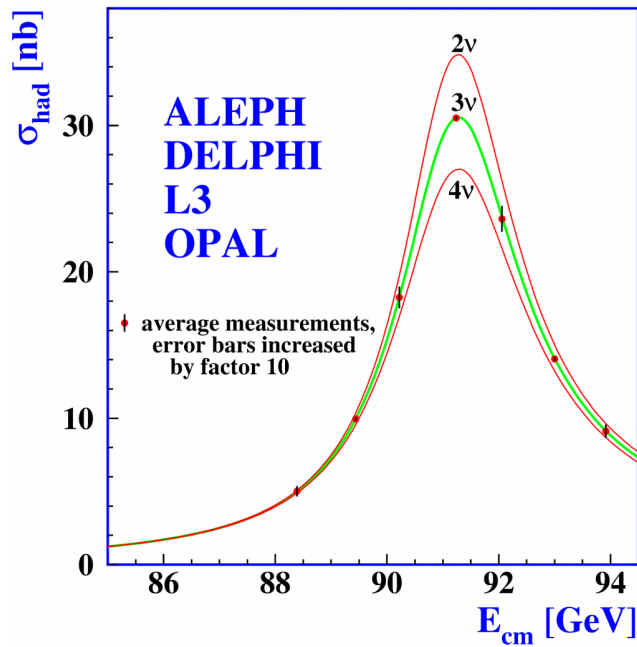Figure 1.1: Fundamental particles of the Standard Model

Figure 1.2: Comparison between experimental data from LEP and theoretical predictions of the total cross section for the production of hadrons as a function of the centre-of-mass energy for the 2, 3 and 4 neutrino families. [23]

impressive accuracy, by the Standard Model weak interaction Lagrangian terms [37]:

$$\mathcal{L}_I^{CC} = -\frac{g}{2\sqrt{2}} j_\alpha^{CC} W^\alpha + h.c., \qquad j_\alpha^{CC} = 2 \sum_{l=e,\mu,\tau} \bar{\nu}_{lL} \gamma_\alpha l_L \qquad (1.1)$$

$$\mathcal{L}_I^{NC} = -\frac{g}{2\cos\theta_W} j_\alpha^{NC} Z^\alpha, \qquad j_\alpha^{NC} = 2 \sum_{l=e,\mu,\tau} \bar{\nu}_{lL} \gamma_\alpha l_L \qquad (1.2)$$

Due to parity violation in weak interactions, only left-handed particles l_L, ν_{lL} or right-handed anti-particles $\bar{l}_L$, $\bar{\nu}_R$ participate to the interaction. For this reason, only LH neutrinos and RH antineutrinos have been introduced in the SM.

1.2 Theory of neutrino oscillations

Neutrino oscillations were first proposed by Bruno Pontecorvo in the late 1950s, who later suggested that $\nu_e \to \nu_\mu$ oscillations were possible in the Sun. This intuition was later confirmed by the Homestake experiment [8], and at present it is at the basis of the solution of the solar neutrino problem.

The discovery of neutrino oscillations has established one of the core aspects of neutrino physics: that neutrinos have a non-zero mass. Indeed, flavour mixing and thus oscillations require neutrino mass terms, which are not foreseen by the SM. Appendix B reviews the main mechanisms predicted to be at the origin of the generation of neutrino masses.

Neutrino oscillations are a quantum mechanical phenomenon that is due to neutrinos being produced via charged current interactions as flavour states, which are a linear superposition of mass eigenstates. This makes possible that a neutrino produced with a specific flavour can later be measured to have a different flavour. The experimental discovery of this new behaviour in 1998 is evidence that the Standard Model is not a complete theory [61].

1.2.1 Three flavours oscillations in vacuum

The 3 orthonormal flavour eigenstates ν_α (where $\alpha = e, \mu, \tau$) are connected to 3 orthonormal mass eigenstates ν_i via a unitary mixing matrix U [61]:

$$\nu_\alpha = \sum_{i=1}^{3} U_{\alpha i} \nu_i \quad \nu_i = \sum_\alpha U_{\alpha i}^* \nu_\alpha \qquad (1.3)$$

The matrix, in the case of 3 neutrino flavours is the PMNS matrix. If we are dealing with Dirac neutrinos, it is characterised by three mixing angles $\theta_{12}, \theta_{23}, \theta_{13}$ and the Dirac

charge-parity (CP) symmetry violating phase δ. In the standard parametrization it has the form

$$U^D = \begin{pmatrix} c_{13}c_{12} & c_{13}s_{12} & s_{13}e^{-i\delta} \\ -c_{23}s_{12} - s_{23}c_{12}s_{13}e^{i\delta} & c_{23}c_{12} - s_{23}s_{12}s_{13}e^{i\delta} & c_{13}s_{23} \\ s_{23}s_{12} - c_{23}c_{12}s_{13}e^{i\delta} & -s_{23}c_{12} - c_{23}s_{12}s_{13}e^{i\delta} & c_{13}c_{23} \end{pmatrix} \quad (1.4)$$

where $c_{ij} \equiv cos(\theta_{ij})$ and $s_{ij} \equiv sin(\theta_{ij})$.

If instead neutrinos are Majorana particles, two additional phases α_1 and α_2 enter in the mixing matrix

$$U^M = U^D S^M(\alpha) \quad (1.5)$$

where

$$S^M(\alpha) = \begin{pmatrix} e^{i\alpha_1} & 0 & 0 \\ 0 & e^{i\alpha_2} & 0 \\ 0 & 0 & 1 \end{pmatrix} \quad (1.6)$$

These two complex phases $\alpha_{1,2}$ however cannot be measured in neutrino oscillation experiments. The mass eigenstates ν_i show a time dependence:

$$\nu_i(t) = e^{-iE_i t}\nu_i \quad (1.7)$$

with $E_i = \sqrt{\vec{p}^2 + m_i^2}$ in natural units (i.e. c=1). If we now consider a flavour state $\nu_\alpha(t)$ which represents a neutrino of definite flavour created at t=0 ($\nu_\alpha(0) = \nu_\alpha$), from eq. 1.3 and 1.7 the time evolution of this state is given by:

$$\begin{aligned} \nu_\alpha(t) &= \sum_i U_{\alpha i} e^{-iE_i t}\nu_i \\ &= \sum_\beta \left(\sum_i U_{\alpha i}^* e^{-iE_i t} U_{\beta i} \right) \nu_\beta \end{aligned} \quad (1.8)$$

The amplitude of the transition $\nu_\alpha \to \nu_\beta$ is then:

$$\mathcal{A}_{\nu_\alpha \to \nu_\beta}(t) = \langle \nu_\beta | \nu_\alpha(t) \rangle = \sum_i U_{\alpha i}^* U_{\beta i} e^{-iE_i t} \quad (1.9)$$

The transition probability is given by the square of the modulus of the amplitude:

$$P_{\nu_\alpha \to \nu_\beta}(t) = \left| \mathcal{A}_{\nu_\alpha \to \nu_\beta}(t) \right|^2 = \sum_{i,j} U_{\alpha i}^* U_{\beta i} U_{\alpha j} U_{\beta j}^* e^{-i(E_i - E_j)t} \quad (1.10)$$

Due to their tiny masses, neutrinos are always ultra-relativistic ($p \gg m$) and we can approximate in natural units:

$$E_i = \sqrt{\vec{p}^2 + m_i^2} \simeq p + \frac{m_i^2}{2p} \simeq E + \frac{m_i^2}{2E}; \quad t \simeq L \quad (1.11)$$

9
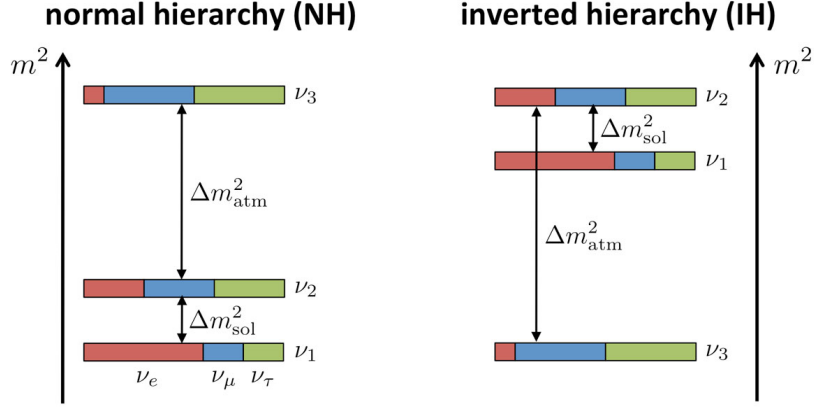
Figure 1.3: Neutrino mass eigenstates possible orderings in normal (left) and inverted (right) hierarchy. The flavour composition of the three states is shown by dividing the bars into colors: red for ν_e, blue for ν_μ and green for ν_τ [28].

with L being the distance travelled by the neutrino. The probability then can be written as:

$$P_{\nu_\alpha \to \nu_\beta}(L, E) = \sum_{i,j} U^*_{\alpha i} U_{\beta i} U_{\alpha j} U^*_{\beta j} \exp\left(-i\frac{\Delta m^2_{ij}L}{2E}\right) \tag{1.12}$$

where $\Delta m^2_{ij} = m^2_i - m^2_j$.

From eq. 1.12 it is possible to derive the probability that starting with ν_α one still detects the same flavour at a distance L, called *survival probability*:

$$P_{\nu_\alpha \to \nu_\alpha}(L, E) = 1 - 4\sum_{k>j} |U_{\alpha k}|^2 |U_{\alpha j}|^2 sin^2\left(\frac{\Delta m^2_{kj}L}{2E}\right) \tag{1.13}$$

The total transition probability, namely the probability of observing a change in flavour, is given by $1 - P_{\nu_\alpha \to \nu_\alpha}$.

As can be seen from eq. 1.12 the oscillation depends on Δm^2_{ij}, three mixing angles θ_{ij} and the Dirac CP violation phase δ. It also depends on the L/E ratio, which is one of the main features that define the different types of neutrino oscillation experiments.

Concerning neutrino mass eigenvalues, from experimental results two scenarios are possible: the so-called *normal* and *inverted ordering*. In normal ordering, neutrino mass eigenvalues are ordered $m_1 < m_2 < m_3$, while in inverted ordering $m_3 < m_1 < m_2$ (Fig. 1.3).
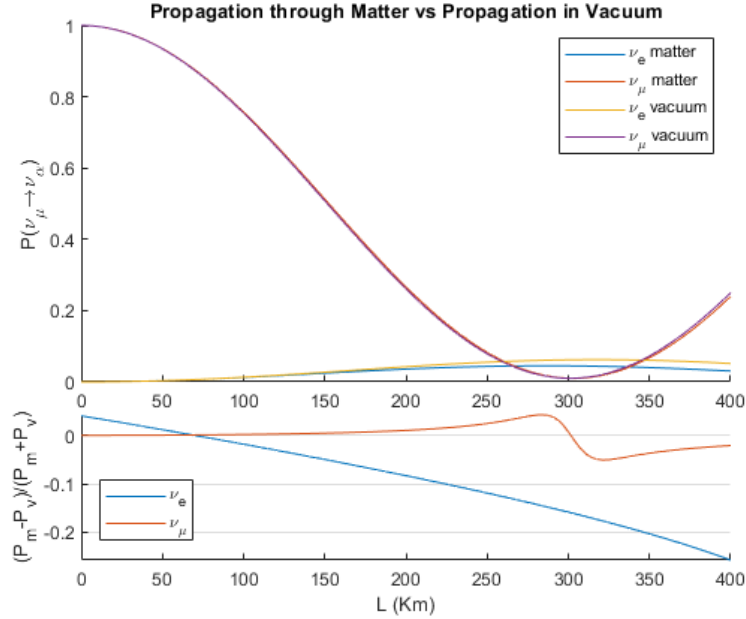
Figure 1.4: Difference between neutrino oscillation amplitude probability for a propagation in vacuum and inside (homogeneous) matter.

Propagation in matter

When neutrinos travel through matter, they can coherently interact with electrons and nuclei in the medium and their oscillation probability is modified. This effect is called the MSW effect, from the names of the physicists Mikhaev, Smirnov and Wolfenstein, who first noticed it [60, 53].

The MSW effect has origin from the fact that ν_e are the only neutrino flavour that can take part both in charged current interactions, and NC elastic interactions with electrons, while ν_μ and ν_τ can only have NC interactions with electrons. This introduces an extra potential in the Hamiltonian of the electron neutrinos:

$$V_e = \pm\sqrt{2}G_F N_e \tag{1.14}$$

where N_e is the electron number density in the medium, G_F is the Fermi constant and the sign is positive for neutrinos and negative for antineutrinos. This difference can be seen in Figure 1.4.

1.2.2 CP symmetry violation

Since all mixing angles are not null, if the Dirac phase δ is different from 0 or π, neutrino oscillations are CP violating phenomena. This introduces an asymmetry in the behaviour

of neutrinos and antineutrinos leading to a difference in the probability of $\nu_\alpha \to \nu_\beta$ with respect its CP conjugate $\bar{\nu}_\alpha \to \bar{\nu}_\beta$. An observable for such effects would then be the CP asymmetry $P(\nu_\alpha \to \nu_\beta) - P(\bar{\nu}_\alpha \to \bar{\nu}_\beta)$, for $\alpha \neq \beta$ and $\alpha, \beta = e, \mu, \tau$. It is shown in Figure 1.5
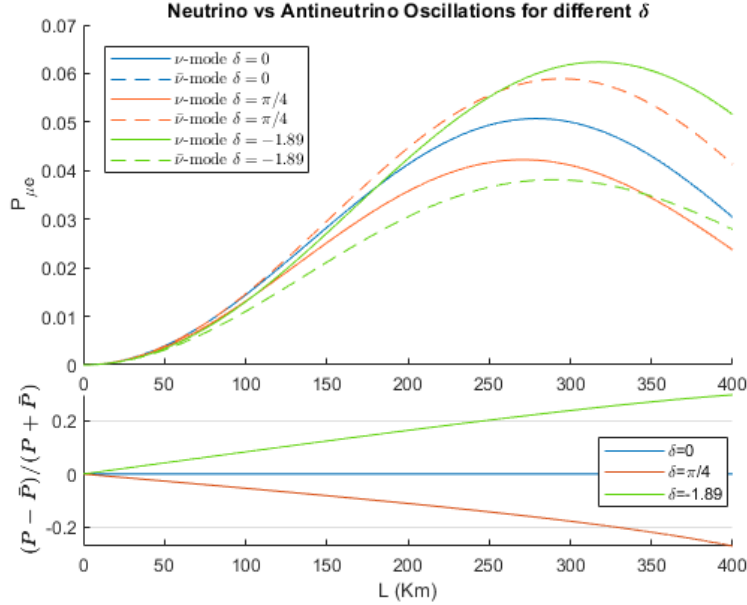
Figure 1.5: Asymmetry in neutrino oscillations due to the CP-violating phase. The neutrino energy is $E = 0.6\,\text{GeV}$

1.3   Neutrino oscillation experiments

Neutrino oscillation experiments are built in order to retrieve the PMNS parameters and the mass-squared difference. This can be done through the measurement of neutrino fluxes at the production and at the detection points, allowing the computation of the oscillation probability $P(\nu_\alpha \to \nu_\beta)$. It is possible to make a first subdivision between different neutrino oscillation experiments, depending on which probability the experiment is trying to measure:

- **Appearance experiments**: these experiments measure the presence of neutrino flavours that are not present in the initial composition of the flux.

- **Disappearance experiments**: these experiments measure the survival probability of neutrino flavours generated at the production point, comparing the initial and final flux.

A further distinction can be made upon the different origins of neutrinos. Experiments using different neutrino sources are sensitive to different sets of parameters. The most relevant ones are:

- **Solar neutrinos**: neutrinos generated in thermonuclear reactions in the core of the Sun. Solar neutrino experiments are sensitive to the Δm_{12}^2 squared mass difference and to $sin2\theta_{12}$, which for this reason are referred to as the *solar* mass difference and the *solar* mixing angle. These experiments can be divided into radiochemical experiments, such as Homestake, Gallex/GNO [12, 15] and Sage, which exploit the Inverse Beta Decay reaction of solar neutrino with ^{37}Cl, ^{71}Ga and ^{71}Ge respectively, and Cherenkov experiments such as Kamiokande and Super-Kamiokande [22, 11], together with SNO [5, 6]. The main advantage of the Kamiokande detector is the real-time nature of the neutrino interactions viewed in the active fiducial volume, together with the possibility to reconstruct direction and energy, since neutrino elastic scattering processes preserve directionality. The data collected by solar neutrino experiments showed the existence of the so called *solar neutrino problem*, a deficit in the number of neutrinos arriving from the Sun between 1/2 and 2/3 with respect to the predictions of the SSM, measured by the earlier radiochemical experiments. The important result of SNO was the that the combined tau and mu fluxes were found to be two times more intense than the ν_e one and that the total flux was in agreement with the predictions from the SSM. This is shown in Figure 1.6.

- **Atmospheric neutrinos**: neutrinos produced form the decay of mesons resulting from cosmic ray interactions with the atmosphere. K and π decays give mainly ν_μ's while μ decay gives both ν_μ's and ν_e's. It is possible to distinguish two types of experimental set-up to detect atmospheric neutrinos. Experiments such as Soudan2 and Macro use iron calorimeters, constituted of layers of iron, acting as a passive material and active plastic scintillators layers, which are able to track electromagnetic showers produced by $e^\pm$ or long muon tracks. The Super Kamiokande experiment instead exploit Cherenkov emission. A large tank of water of the order of 1 ton is surrounded by photomultipliers; analysing the rings produced by Cherenkov light it is possible to discriminate the flavour of the incoming neutrino. The measurements of the iron calorimeters performed in the 80's and 90's observed a noticeable ν_μ deficit, later confirmed in 1998 by Super Kamiokande, which showed that while the electron events had no reduction, the muon events had a deficit of almost 50% for up-going neutrinos. The results can be explained considering the fact that the neutrino oscillation phenomena driven by the parameters Δm_{23}^2 and θ_{23} that for this reason are often referred to as *atmospheric* oscillation parameters.

- **Reactor neutrinos**: mainly $\bar{\nu}_e$, produced by the beta decay of fission fragments in nuclear power plants. Reactor experiments can measure the disappearance prob-

ability of the $\bar{\nu}_e$ and are usually sensitive to small values of Δm^2 due to the low energy spectrum of the neutrinos. Among reactor experiments, we can count Long Baseline Experiments, like KamLAND, and Short Baseline Experiments such as Daya Bay, Double Chooz, and RENO. The latter are also sensitive to the measurement of the θ_{13} mixing angle. In the next future reactor experiment will be a key player in determining neutrino mass ordering and precision measurement of θ_{12}, Δm_{32}^2, and Δm_{31}^2 to sub-percent level.

- **Accelerator neutrinos**: the neutrino beam is produced from decays of pions and kaons (mainly), generated from a proton beam hitting a target. Among accelerator experiments, K2K (KEK to Kamioka) in Japan and MINOS at Fermilab were the first to confirm the atmospheric oscillation results. The successor of K2K, T2K (Tokai to Kamioka) used a muon neutrino ($E \simeq 0.6\,\mathrm{GeV}$) beam and, together with the NoVA experiment, was able to perform precision measurements on atmospheric parameters $\sin 2\theta_{23}$ and Δm_{31}^2, in both appearance and disappearance channels. T2K in particular strongly constrained the range of values of the CP-violating phase δ, excluding values of 0 and π at the 95% confidence level (see Figure 1.7).

For a more complete description of neutrino oscillation experiments the reader may have a look at Appendix C.

1.3.1 Experimental results

In the previous subsections, we reviewed the different experimental neutrino data samples, discussing their dominant sensitivity to one or two oscillation parameters. However, every data sample also offers subleading sensitivities to other parameters as well. Although the information they can provide about such parameters may be limited, in combination with the rest of the data samples, relevant information can emerge. This constitutes the main philosophy behind global analyses of neutrino oscillation data: joint analyses that try to exploit the complementarity of the different experiments to improve our knowledge of the neutrino oscillation parameters. In the table below are shown the results of a combined analysis of neutrino oscillation data in the framework of the
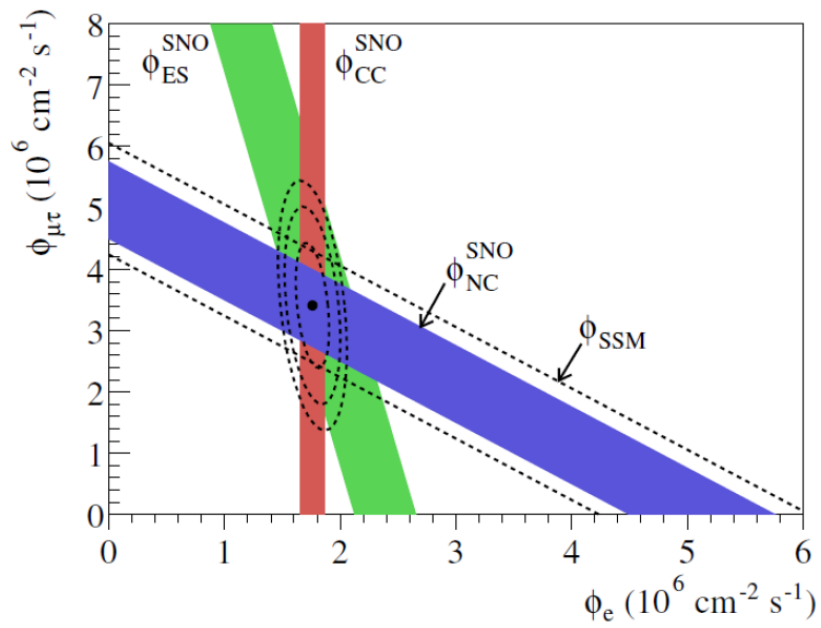
Figure 1.6: Flux of muon and tau neutrinos $\Phi_{\nu\tau}$ over electron neutrino Φ_e as measured by SNO. The three coloured bands correspond to the three possible interactions: electron scattering ES (green); charged current CC (red); neutral current NC (blue). The dashed band gives the prediction from the SSM which is in agreement with the NC measurements [18].
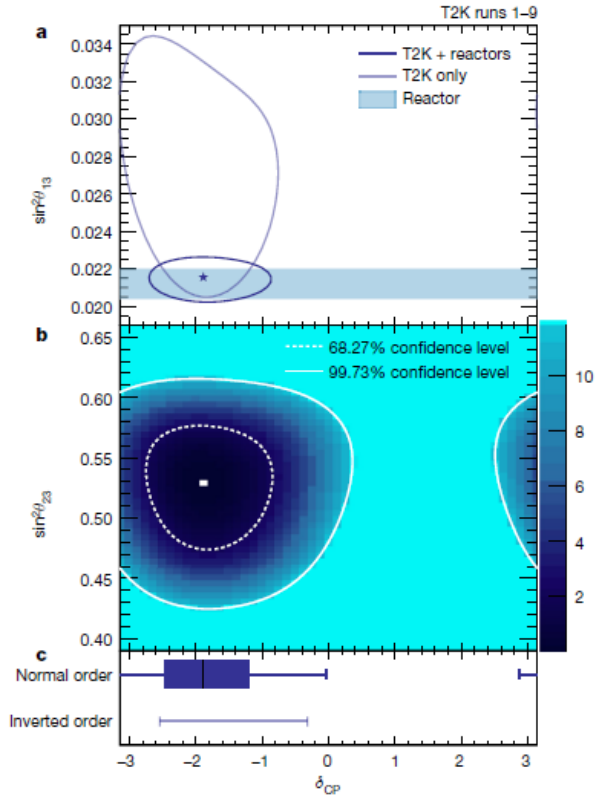
Figure 1.7: 68 and 99% C.L. allowed regions at the **(a)** δ_{cp} - $\sin 2\theta_{13}$ and **(b)** δ_{cp} - $\sin 2\theta_{23}$ plane. Plotted results are obtained from the T2K experiment alone or combining data with reactor experiments [36].
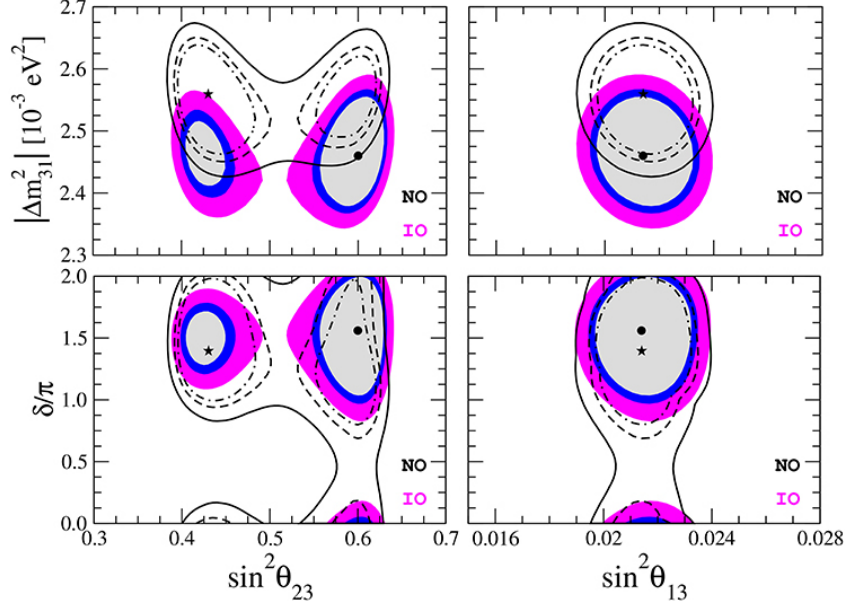
Figure 1.8: Allowed regions at 90, 95, and 99% C.L. in the planes $\sin 2\theta_{23}$ - Δm_{31}^2, $\sin 2\theta_{13}$ - Δm_{31}^2, $\sin 2\theta_{23}$ - δ_{cp} and $\sin 2\theta_{23}$ - δ_{cp} for NO (lines) and IO (colored regions). The star indicates the global best fit point, corresponding to normal ordering, while the circle indicates the local minimum in inverted ordering [17].

three-flavour neutrino oscillation scheme, a similar overview is also offered by Figure 1.8.

|	Normal Ordering	Inverted Ordering
$\sin^2 \theta_{12}/10^{-1}$	$3.10^{+0.13}_{-0.12}$	$3.10^{+0.13}_{-0.12}$
$\theta_{12}/°$	$33.82^{+0.78}_{-0.76}$	$33.82^{+0.78}_{-0.76}$
$\sin^2 \theta_{23}/10^{-1}$	$5.58^{+0.20}_{-0.33}$	$5.63^{+0.19}_{-0.26}$
$\theta_{23}/°$	$48.3^{+1.2}_{-1.9}$	$48.6^{+1.1}_{-1.5}$
$\sin^2 \theta_{13}/10^{-2}$	$2.241^{+0.066}_{-0.065}$	$2.261^{+0.067}_{-0.064}$
$\theta_{13}/°$	$8.61^{+0.13}_{-0.13}$	$8.65^{+0.13}_{-0.12}$
$\delta_{CP}/°$	222^{+38}_{-28}	285^{+24}_{-26}
$\Delta m_{21}^2/10^{-5} eV^2$	$7.39^{+0.21}_{-0.20}$	$7.39^{+0.21}_{-0.20}$
$\Delta m_{32}^2/10^{-3} eV^2$	$2.449^{+0.032}_{-0.030}$	$-2.509^{+0.032}_{-0.032}$

The results reported are not conclusive yet, and we will have to wait for the next generation of experiments to fully answer fundamental questions:

1. The determination of the absolute mass of neutrinos;

2. The measurement of CP asymmetries in the leptonic field;

17

3. The determination of the mass ordering (normal or inverted);

4. The determination of neutrino origin *i.e.* Dirac or Majorana.

Some of the future experiments devoted to this purpose (among others), such are DUNE, JUNO, or RENO-50.

Chapter 2

The DUNE experiment

The international DUNE experiment, hosted by the Fermi National Accelerator Laboratory (Fermilab) of the US Department of Energy, is divided into three central components (Figure 2.1):

1. a new, high-intensity neutrino source generated from a megawatt-class proton accelerator at Fermilab;

2. a massive Far Detector (FD) situated 1.5 km underground at the Sanford Underground Research Facility (SURF) in South Dakota;

3. a composite Near Detector (ND) installed just downstream of the neutrino source.

The Long-Baseline Neutrino Facility (LBNF) project, also hosted by Fermilab, provides the beamline and civil construction for the DUNE experiment. The organization and management of LBNF is separate from that of the experiment; its design and construction are organized as a U.S. DOE/Fermilab project incorporating international partners.

2.1   The Long-Baseline Neutrino Facility (LBNF)

The LBNF beamline at Fermilab will deliver the world's most intense neutrino beam to near and far detection centres in an on-axis configuration. The upgrade to the Proton Improvement Plan II (PIP-II), a leading-edge, superconducting, linear proton accelerator under construction at Fermilab, will deliver between 1.0 and 1.2MW of proton beam power from the Fermilab Main Injector to LBNF, which will focus the proton beam in a wide energy band of 60 GeV to 120 GeV. The secondary particles produced when the beam strikes the target are focused by a set of magnetic horns and sent toward the far detector passing through a 200 m long decay pipe, where they are allowed to decay to generate the neutrino beam. At the end of the decay pipe, an absorber pile removes the residual hadrons. The focusing structure is optimised to provide a wide band neutrino
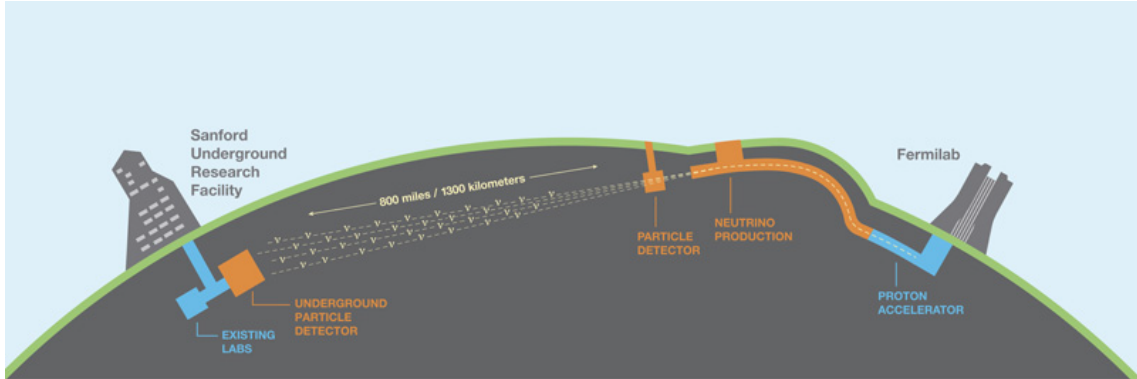
Figure 2.1: Configuration of the LBNF beamline at Fermilab, in Illinois, and the DUNE detectors in Illinois and South Dakota, separated by 1300 km [31].
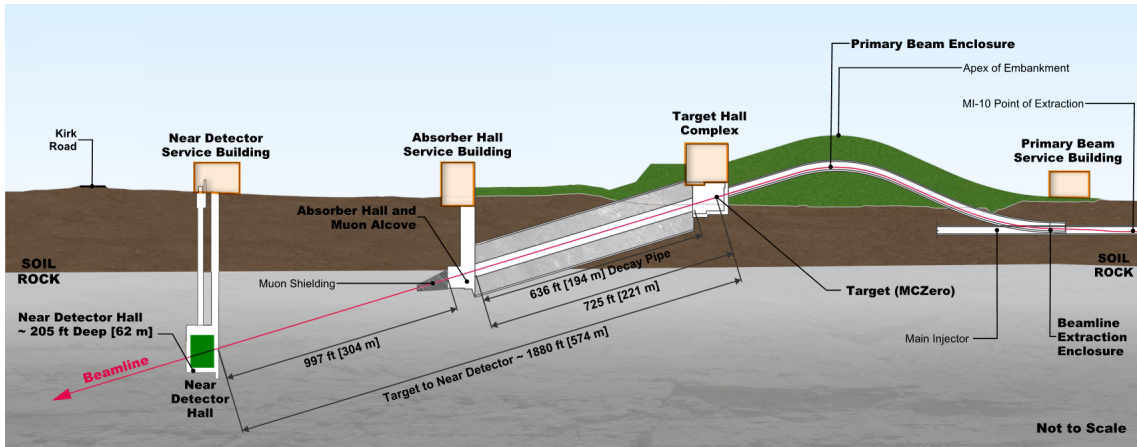
Figure 2.2: Neutrino beamline and DUNE near detector hall at Fermilab in Illinois [31].

beam with an energy range between 0.5 and 5 GeV so as to cover the first and second neutrino oscillation maxima, which for a 1300 km baseline are approximately 2.4 and 0.8 GeV. A schematic layout of the beamline is shown in Figure 2.2.

Inverting the horn current polarity both ν_μ or $\bar{\nu}_\mu$ beams with small contamination of ν_e, $\bar{\nu}_e$ and "wrong sign" muon neutrinos can be produced. The expected neutrino unoscillated fluxes at FD site with the 120 GeV proton beam are shown in Figure 2.3, both for the horn positive and negative current polarity.

The general specifications of the primary beam and the characteristics of the beam are listed in Table 2.1, corresponding to the parameters expected following the PIP-II [35] upgrade.

Parameter	Values	
Energy	60 GeV	120 GeV
Protons per cycle	7.5×10^{13}	7.5×10^{13}
Spill duration	1.0×10^{-5}sec	1.0×10^{-5}sec
Protons on target per year	1.9×10^{21}	1.1×10^{21}
Cycle time	0.7 sec	1.2 sec
Beam Power	1.03 MW	1.2 MW
Beam size at target	1.5 to 1.7 mm	
$\Delta p/p$	11×10^{-4} 99% (28×10^{-4} 100%)	
Beam divergence (x,y)	17 to 15 μrad	

Table 2.1: Summary of principal primary proton beam design parameters and characteristics [33].

2.2 The DUNE detectors

2.2.1 Far Detector reference design

The DUNE FD will consist of four LArTPC detector modules, each with a LAr mass in the sensitive region of the cryostat (fiducial mass) of at least 10 kt, installed approximately 1.5 km underground. Each LArTPC fits inside a cryostat of internal dimensions 15.1 m(w) $\times$ 14.0 m(h) $\times$ 62.0 m(l) that contains a total LAr mass of approximately 17.5 kt.

DUNE is planning and currently developing two LArTPC technologies: single-phase (SP) in which all detector elements inside the cryostat are immersed in liquid; and dual-phase (DP), in which some components operate in a layer of gaseous argon above the liquid.

Single Phase detector module

In the SP technology, ionization charges drift horizontally in the LAr under the influence of a strong E field of 500 V/cm towards a vertical anode, where they are read out. This design requires very low-noise electronics to achieve readout with a good signal-to-noise (S/N) ratio because no signal amplification occurs inside the cryostat. This technology was pioneered in the ICARUS project and is the one used for Fermilab's currently operating MicroBooNE detector. Figure 2.4 shows the operating principle of an SP LArTPC.

As can be seen in Figure 2.5 an SP module is instrumented with three module-length (58 m) anode planes constructed from 6 m high by 2.3 m wide anode plane assemblies (APAs). Each APA consists of an aluminum frame with three layers of active wires,
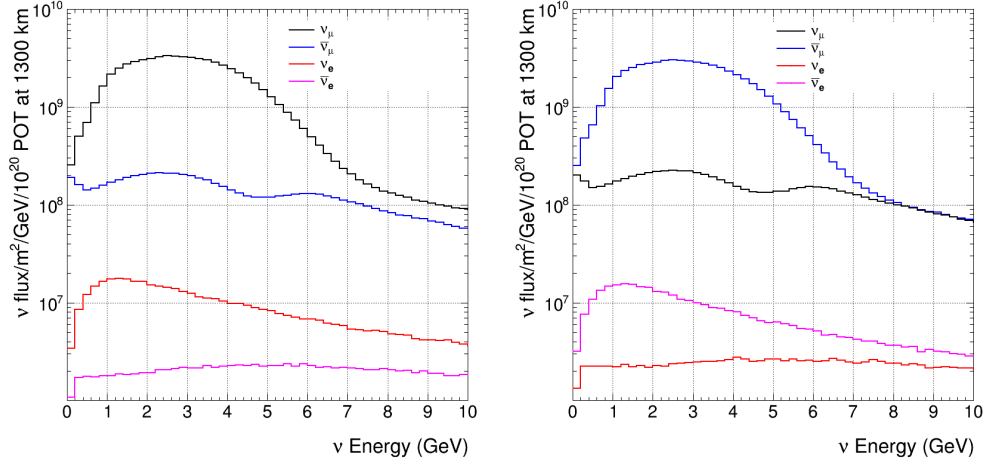
Figure 2.3: Neutrino (left) and antineutrino (right) Fluxes at the Far Detector as a function of energy in the absence of oscillations with the horns focusing positive particles. In addition to the dominant ν_μ ($\bar{\nu}_\mu$) flux, the minor components are also shown [33].
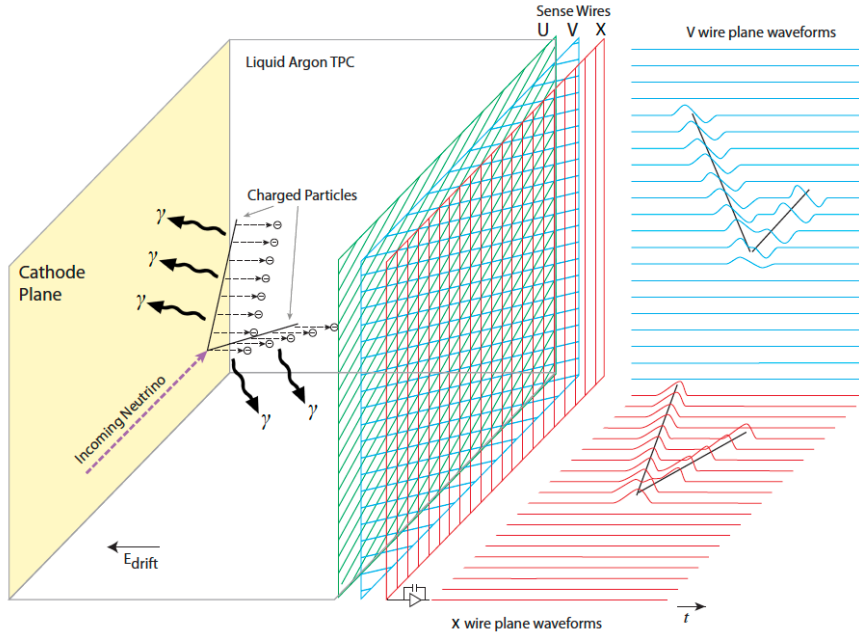
Figure 2.4: The general operating principle of the SP LArTPC. Negatively charged ionization electrons from the neutrino interaction drift horizontally opposite to the E field in the LAr and are collected on the anode, which is made up of the U, V and X sense wires. The right-hand side represents the time projections in two dimensions as the event occurs [31].
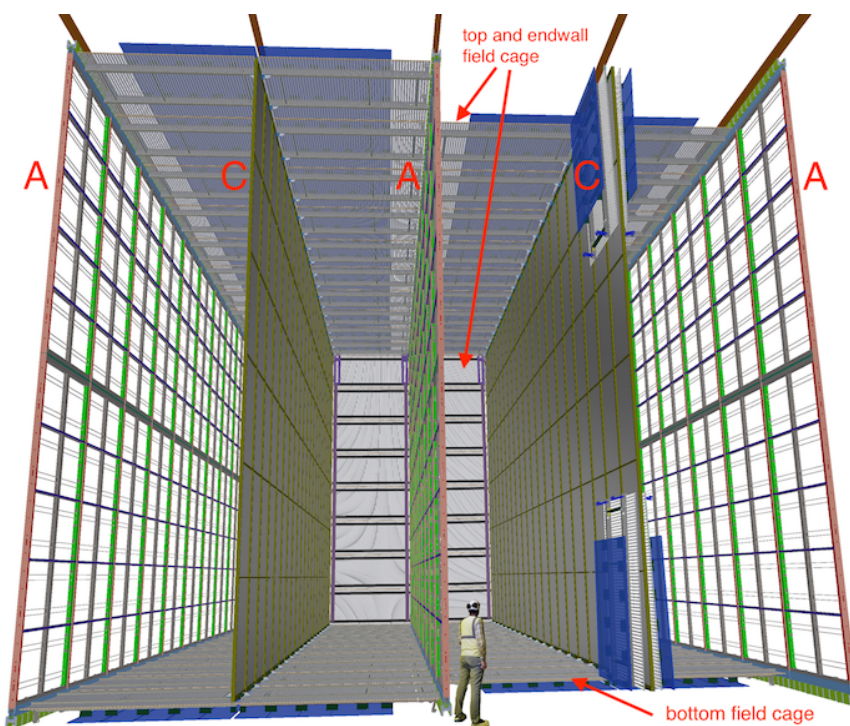
Figure 2.5: A 10 kt DUNE FD SP module, showing the alternating 58.2 m long (into the page), 12.0 m high anode (A) and cathode (C) planes, as well as the field cage (FC) that surrounds the drift regions between the anode and cathode planes [31].

strung at angles chosen to reduce ambiguities in event reconstruction, that form a grid on each side of the APA. Two APAs are vertically stacked to cover the entire height of the active volume of the TPC. 25 of these stacks are placed side by side to form an anode plane that occupies the whole active volume length.

Double Phase detector module

The DP operating principle is very similar to that of the SP. Even if this technology is less mature than the SP one, it offers several advantages. Charged particles that traverse the active volume of the LArTPC ionise the medium, while also producing scintillation light. The ionisation electrons drift, in this case vertically, along an E field towards an extraction grid just below the liquid-vapour interface (see Figure 2.6). After reaching the grid, an E field stronger than the 500 V/cm drift field extracts the electrons from the liquid up into the gas phase, where they encounter micro-pattern gas detectors, called LEMs, with high-field regions in which they are amplified. The amplified charge is then collected and recorded on a 2D anode. An array of photomultiplier tubes (PMTs) coated with a wavelength-shifting material sits below the cathode to record the time (t0)
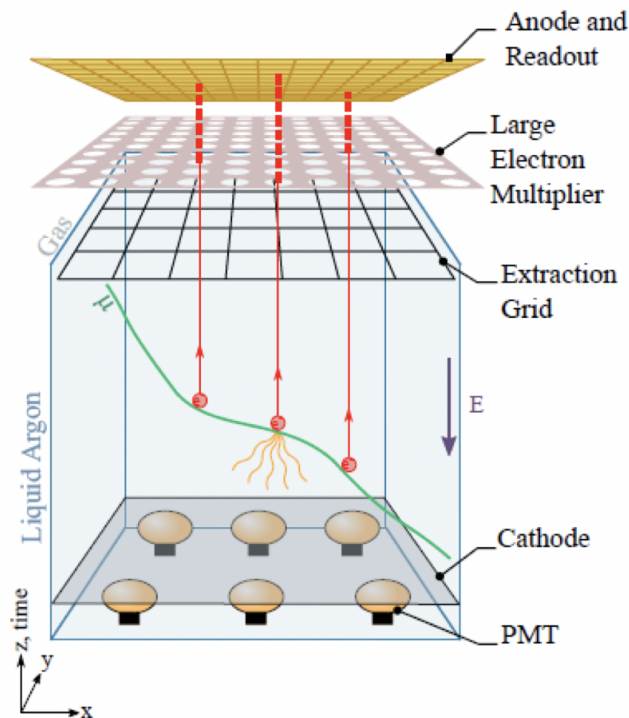
Figure 2.6: Operating principle of the DP read-out.

and pulse characteristics of incident light. Figure 2.7 displays a possible design for the dual-phase LArTPC design module of the FD.

The gain achieved in the gas reduces the stringent requirements on the electronics noise, and the overall design increases the possible drift length, which, in turn, requires a correspondingly higher voltage. Although the SP design has multiple drift volumes, the DP module design allows a single, fully homogeneous LAr volume with a much longer drift length.

2.2.2 Near Detector reference design

The Near Detector will be located at Fermilab 574 m downstream of the neutrino beam source and will consist of three elements: two movable subdetectors, a LArTPC (called ArgonCube) and the Multipurpose Detector (MPD), which aim to measure neutrino flux and energy spectrum at off-axis positions, and a fixed one, System for On-Axis Neutrino Detection (SAND) (see Figure 2.8).

The ND will serve as the control of the experiment, restricting systematic errors and measuring the initial unoscillated ν_μ and ν_e energy spectra (and those of the corresponding antineutrinos). The two movable detectors will use the Ar as target material to

24
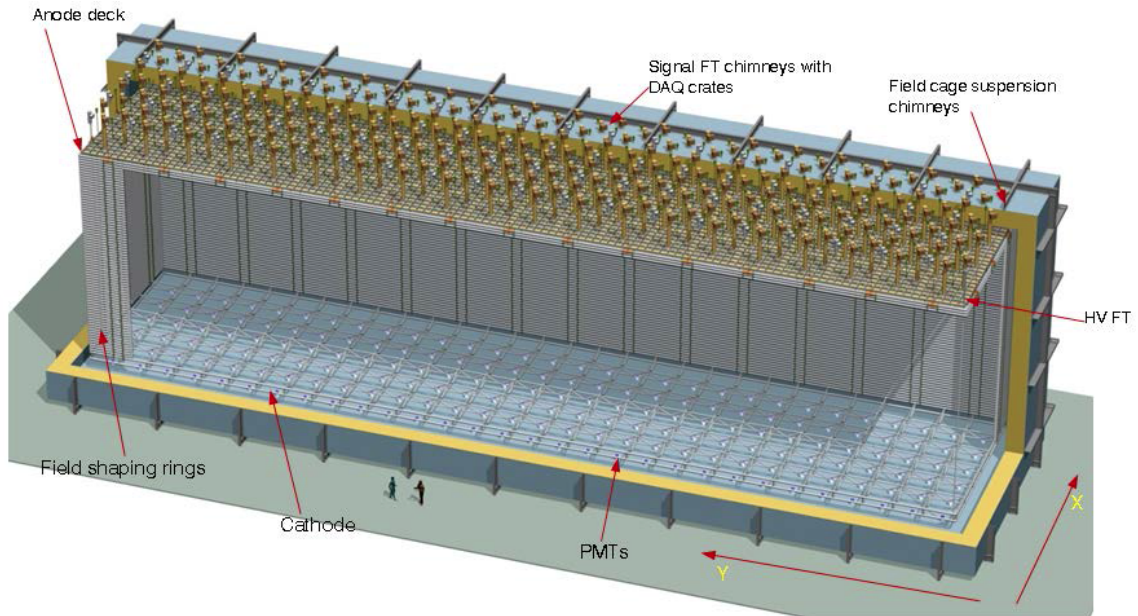
Figure 2.7: Representation of a possible dual-phase LArTPC design module of the Far Detector.
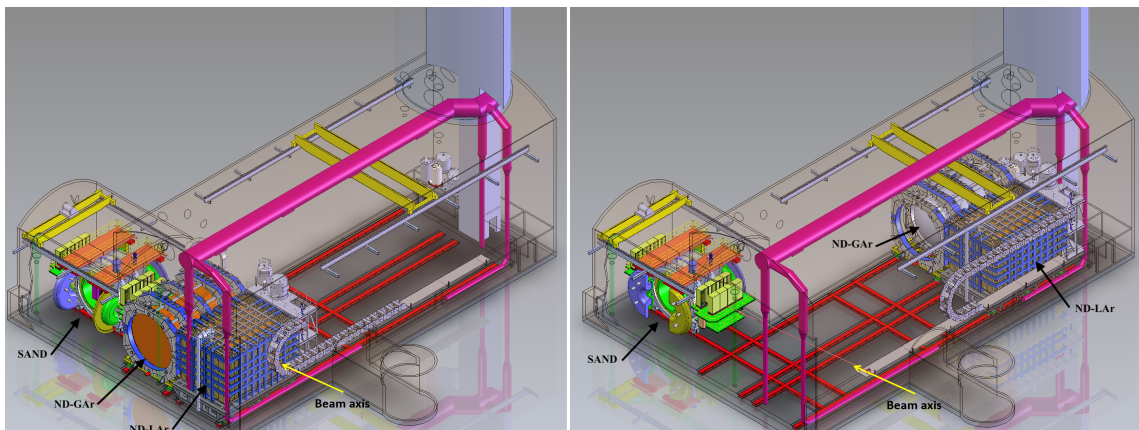
Figure 2.8: Representation of the Near Detector hall, with component detectors all in the on-axis configuration(left) and with the ND-LAr and ND-GAr in an off-axis configuration (right) [32].
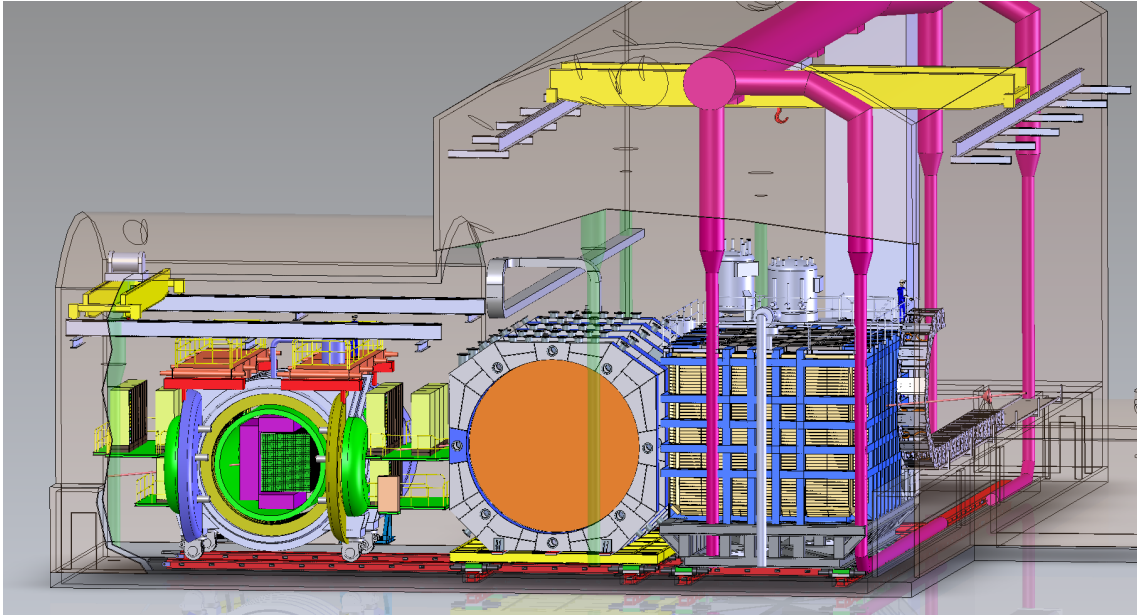
Figure 2.9: DUNE ND. The axis of the beam enters from the right. Neutrinos first encounter the LArTPC (right), the MPD (center), and then the on-axis beam monitor (left).

reduce the systematics uncertainties on the neutrino cross-section.

ArgonCube

ArgonCube will consist of several identical modules in a common tank of liquid Argon; each of them includes two different TPCs with a 0.33 m drift length, two independent pixel charge readout planes, and light detection systems. See Figure 2.10 for more clarification. This detector has the same target nucleus and uses the same fundamental detection principles as the FD, reducing the sensitivity to nuclear effects and the systematic uncertainties driven by the detector in the extraction of the oscillation signal in the FD. The LArTPC is large enough to provide high statistics ($1 \times 10^8 \nu_\mu$-CC events/year on axis) and a sufficient volume to provide containment of the hadronic system. The tracking and energy resolution, combined with the fiducial mass of ArgonCube, will allow for the measurement of the flux in the beam using several techniques, including the rare process of $\nu - e^-$ scattering. This detector alone begins to lose acceptance for muons above $\sim 0.7\,\mathrm{GeV/c}$ due to lack of containment.
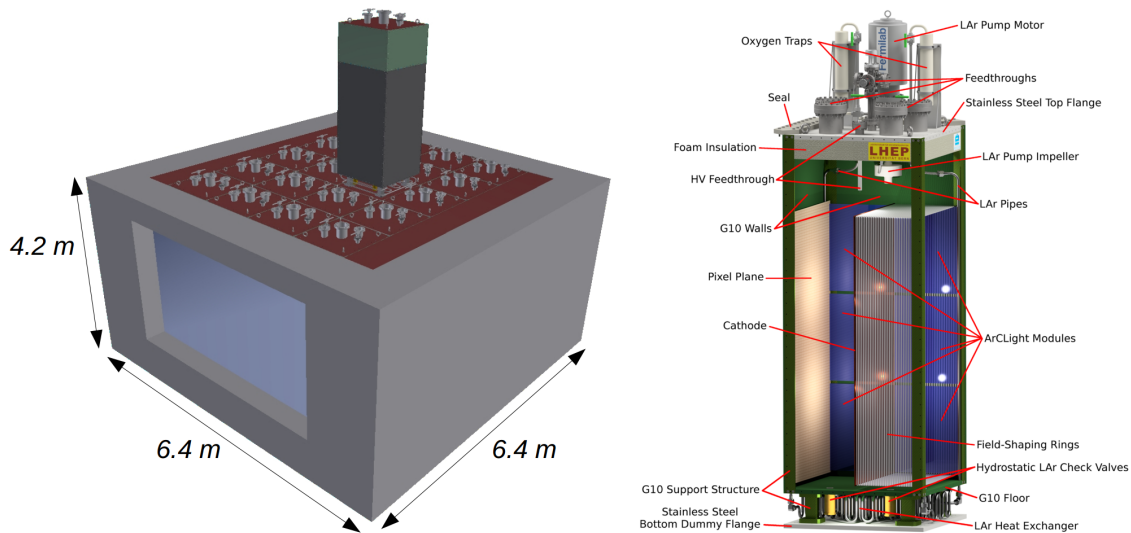
Figure 2.10: Representation of the design of ArgonCube (left) and of one of its module (right).

Multipurpose Detector

The MPD is placed downstream of the ArgonCube detector; It consists of a high pressure gaseous time projection chamber (HPgTPC) surrounded by an electromagnetic calorimeter (ECAL) in a 0.5 T magnetic field, provided by a superconductive magnet. The high-pressure gaseous argon TPC runs at 10 atmospheres and provides a lower-density medium with excellent tracking resolution to momentum analyse the muons from LArTPC. In addition, neutrinos interacting with the argon in the MPD constitute a large, independent sample of ν-Ar interactions that can be studied with a very low momentum threshold for charged particle tracking, excellent tracking resolution, nearly uniform angular coverage, and with systematic uncertainties that differ from the liquid detector.

The misidentification of pions as knocked-out protons (or vice versa) can cause a significant misreconstruction of the neutrino energy and/or a mistake in the event type classification. This effect can become quite significant at the lower-energy second oscillation maximum. The gas detector will play an important role in understanding how often the FD and LArTPC make this mistake, since pions are rarely misidentified as protons in the high pressure gaseous argon TPC.

ND-LAr and ND-GAr can move to take data at positions off the beam axis. This capability is referred to as the DUNE Precision Reaction-Independent Spectrum Measurement (DUNE-PRISM). As the detectors move off-axis, generally together, the incident neutrino flux spectrum changes, with the mean energy dropping and the spectrum becoming narrower. The data taken at different off-axis angles will allow for the decon-

volution of the neutrino flux and interaction cross section, as well as the mapping of the reconstructed versus true-energy response of the detector.

SAND

The final component of the DUNE ND suite is a magnetised beam monitor called the System for On-Axis Neutrino Detection (SAND). This device monitors the flux of neutrinos going to the FD from an on-axis position, where it is much more sensitive to variations in the neutrino beam. For a more complete description of this detector, read Chapter 3.

2.2.3 Requirements

The general expression for the number of events for a process X, both in the Near and Far detectors is:

$$N_X(E_{rec}) = \int_{E_\nu} dE_\nu \Phi(E_\nu) P_{osc}(E_\nu) \sigma_X(E_\nu) R_{phys}(E_\nu, E_{vis}) R_{det}(E_{vis}, E_{rec}) \qquad (2.1)$$

where Φ is the incoming neutrino flux, σ_X is the cross section of the process on a given nucleus, R_{phys} is the physics response introduced by nuclear smearing and R_{det} is the detector acceptance for the final state particles. E_ν, E_{vis} and E_{res} are the true neutrino energy, the total energies of the visible final-state particles, and the final reconstructed energy. In order to unfold the main terms of the expression, different detectors and nuclear targets must be used. For this reason, a capable Near Detector complex is mandatory. In particular, a precise beam-monitor detector is needed. The System for on-Axis for Neutrino Detection (SAND), which composes the DUNE Near Detector system, has as major task the continuous beam monitoring and the precise determination of its energy spectrum. In this way, the ND will provide constraints on all systematic uncertainties relevant to the oscillation analysis. The basic requirement is that the combined systematics be smaller than the correspondent statistical uncertainties.

2.3 DUNE's scientific program

The scientific goals behind the DUNE experiment are grouped into a *primary scientific program* and an *ancillary scientific program* [31].

The primary program aims to answer some open questions in neutrino and astroparticle physics:

- Confirmation of the CP-violation in the leptonic sector, which could provide a possible explanation of the matter-antimatter asymmetry in the Universe;

- Determination of the neutrino mass ordering;

- Achievement of precision measurements of three-flavour neutrino oscillations;

- Search for proton decay, which would represent a confirmation of the GUT theories;

- Detection and measurement of the ν_e flux of a core-collapse supernova, which should shed light on the nature of this astrophysical event.

The ancillary science programme instead consists of a series of objectives that the experiment has not specifically planned to achieve, but that could nevertheless enabled by the facility's design:

- BSM physics research through neutrino flavour transition measurements;

- Neutrino oscillation measurements using atmospheric neutrinos;

- Research on neutrino interaction physics through measurements of neutrino cross sections, studies of nuclear effects, and nucleon structure measurements.

2.3.1 Sensitivities and systematics

The ν_μ energy spectrum measured at the Near detector is used to predict both the ν_μ and ν_e expected spectra at the Far Detector site: $N_{FD}^{expected}(\nu_\mu)$ and $N_{FD}^{expected}(\nu_e)$ [34]. The observed spectrum of neutrino events is the product of beam flux Φ, detector efficiency ϵ, and neutrino interaction cross section σ.

$$N_{ND}^{data}(\nu_\mu) = \Phi_{ND}(\nu_\mu) \otimes \epsilon_{ND}(\nu_\mu) \otimes \sigma_{ND}(\nu_\mu) \tag{2.2}$$

This formula however has to be corrected in order to correctly extrapolate the spectra observed in the ND to the Far Detector. In fact, have to be considered:

- **Differences in the beam flux between ND and FD**, Φ_{FD}/Φ_{ND}. The Near Detector, being closer to the neutrino beamline than the Far Detector, sees an extended neutrino source. A Monte Carlo simulation is used in order to correct these differences.

- **Differences in the Near and Far Detector efficiencies**, $\epsilon_{FD}/\epsilon_{ND}$. These uncertainties are due to the different event selection efficiencies and the imperfect modeling of the energy scales of Near and Far Detectors. The possibility to have identical detectors allows to cancel uncertainties in the extrapolation for ν_μ signal prediction. For ν_e signal prediction instead there are residual uncertainties which arise from the different criteria used to select ν_e and ν_μ candidate events.

- **Differences in the interactions of neutrinos in the Near and Far detectors**, σ_{FD}/σ_{ND}. Concerning ν_μ, if the Near and Far Detectors have the same target nucleus these differences are canceled. Wherease, when the nu-mu signal in the ND is used to predict the ν_e (ν_τ) signals in the FD, the uncertainties arising from differences in ν_e (ν_τ) interactions dominate.

Summing all up, the expected signals in the FD are given by:

$$N_{FD}^{data}(\nu_\mu) = N_{ND}^{data}(\nu_\mu) \otimes \frac{\Phi_{FD}(\nu_\mu)}{\Phi_{ND}(\nu_\mu} \otimes P(\nu_\mu \to \nu_\mu) \otimes \frac{\epsilon_{FD}(\nu_\mu)}{\epsilon_{ND}(\nu_\mu)} \otimes \frac{\sigma_{FD}(\nu_\mu)}{\sigma_{ND}(\nu_\mu)} \qquad (2.3)$$

$$N_{FD}^{data}(\nu_e) = \underbrace{N_{ND}^{data}(\nu_\mu) \otimes \frac{\Phi_{FD}(\nu_\mu)}{\Phi_{ND}(\nu_\mu} \otimes P(\nu_\mu \to \nu_e) \otimes \frac{\epsilon_{FD}(\nu_e)}{\epsilon_{ND}(\nu_\mu)} \otimes \frac{\sigma_{FD}(\nu_e)}{\sigma_{ND}(\nu_\mu)}}_{\text{expected signal events}}$$

$$+ \underbrace{N_{ND}^{data}(\nu_e) \otimes \frac{\Phi_{FD}(\nu_e)}{\Phi_{ND}(\nu_e)} \otimes P(\nu_e \to \nu_e) \otimes \frac{\epsilon_{FD}(\nu_e)}{\epsilon_{ND}(\nu_e)} \otimes \frac{\sigma_{FD}(\nu_e)}{\sigma_{ND}(\nu_e)}}_{\text{beam } \nu_e \text{ events}} \qquad (2.4)$$

$$+ \text{NC background extrapolated from } N_{ND}^{data}(\nu_e)$$

$$+ \nu_\tau \text{ background extrapolated from } N_{ND}^{data}(\nu_\mu)$$

The main sources of uncertainties are estimated looking at similar experiments, such as MINOS and T2K, and are thought to be:

- **Beam flux uncertainties**: they are related to the precision with which the absolute normalisation and shape of the different components of the neutrino beam will be measured by the ND. The ND has been designed to significantly improve performance relative to the current generation of high-intensity flux neutrino detectors.

- **ν_μ energy-scale uncertainty**: since the spectrum of ν_μ events in the ND is used to predict the ν_e appearance signal at the FD, the uncertainty on ν_μ energy-scale is propagated as an uncertainty on the ν_e appearance signal.

- **Absolute ν_e energy-scale uncertainty**: in order to obtain the desired mass-ordering and CP-violation sensitivity an accurate measurement of the ν_e appearance signal shape is necessary. The measurement of the absolute energy-scale of ν_e depends on the detector response and it is expected to be an important systematic uncertainty in the DUNE oscillation analysis.

- **Simulation uncertainties**: these type of uncertainties refer primarily to uncertainties in the neutrino-target nucleus interaction in the Near and Far Detectors.

Source of Uncertainty	MINOS Absolute/ν_e	T2K ν_e	LBNE ν_e	Comments
Beam Flux after N/F extrapolation	3%/0.3%	2.9%	2%	MINOS is normalization only. LBNE normalization and shape highly correlated between ν_μ/ν_e.
Detector effects				
Energy scale (ν_μ)	7%/3.5%	included above	(2%)	Included in LBNE ν_μ sample uncertainty only in three-flavor fit. MINOS dominated by hadronic scale.
Absolute energy scale (ν_e)	5.7%/2.7%	3.4% includes all FD effects	2%	Totally active LArTPC with calibration and test beam data lowers uncertainty.
Fiducial volume	2.4%/2.4%	1%	1%	Larger detectors = smaller uncertainty.
Neutrino interaction modeling				
Simulation includes: hadronization cross sections nuclear models	2.7%/2.7%	7.5%	$\sim 2\%$	Hadronization models are better constrained in the LBNE LArTPC. N/F cancellation larger in MINOS/LBNE. X-section uncertainties larger at T2K energies. Spectral analysis in LBNE provides extra constraint.
Total	5.7%	8.8%	3.6 %	Uncorrelated ν_e uncertainty in full LBNE three-flavor fit = 1-2%.

Figure 2.11: Dominant systematics on the ν_e appearance channel for T2K and MINOS and the ones expected in the LBNE experiment, the preliminary name used for DUNE [9].
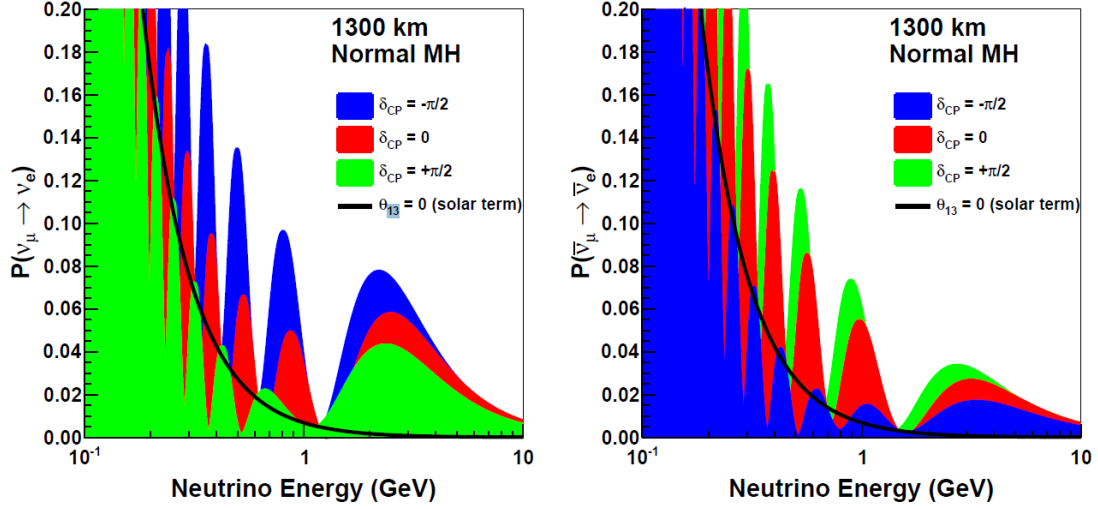
Figure 2.12: The appearance probability at a baseline of 1300 km, as a function of neutrino energy for different values of δ_{CP}, assuming Normal Ordering. The black line indicates the oscillation probability if θ_{13} were equal to zero. This situation is the one faced by the DUNE FD, since it will be at about $\sim 1300\,\mathrm{km}$ from the neutrino source.

2.3.2   Neutrino mass ordering and CP-violation

The DUNE experiment will determine the ordering of the neutrino mass and the CP-violation measuring probability of $\nu_\mu \to \nu_e$ and $\bar{\nu}_\mu \to \nu_e$ oscillation. In particular, the oscillation probability of $\nu_\mu \to \nu_e$ through matter in a constant density approximation is, at first order [47]:

$$
\begin{aligned}
P(\nu_\mu \to \nu_e) \simeq{} & \sin^2\theta_{23}\sin^2 2\theta_{13}\frac{\sin^2(\Delta_{31}-aL)}{(\Delta_{31}-aL)^2}\Delta_{31}^2 \\
& + \sin 2\theta_{23}\sin 2\theta_{13}\sin 2\theta_{12}\frac{\sin(\Delta_{31}-aL)}{(\Delta_{31}-aL)}\Delta_{31}\frac{\sin(aL)}{aL}\Delta_{21}\cos(\Delta_{31}+\delta_{CP}) \\
& + \cos^2\theta_{23}\sin^2 2\theta_{12}\frac{\sin^2(aL)}{(aL)^2}\Delta_{21}^2
\end{aligned}
$$

(2.5)

where $\Delta_{ij} = \Delta m_{ij}^2 L/4E_\nu$, $a = G_F N_e/\sqrt{2}$, G_F is the Fermi constant, N_e is the number density of electrons in Earth, L is the beamline in Km, and E_ν is the neutrino energy in GeV (see Figure 2.12). When the $\bar{\nu}_\mu \to \nu_e$ channel is considered, both δ_{CP} and a switch signs: in this way a neutrino-antineutrino asymmetry $\mathcal{A}$ is introduced both by CPV (δ_{CP}) and the matter effect (a).

$$
\mathcal{A} = \mathcal{A}_{CP} + \mathcal{A}_{matter} = \frac{P(\nu_\alpha \to \nu_\beta) - P(\bar{\nu}_\alpha \to \bar{\nu}_\beta)}{P(\nu_\alpha \to \nu_\beta) + P(\bar{\nu}_\alpha \to \bar{\nu}_\beta)}
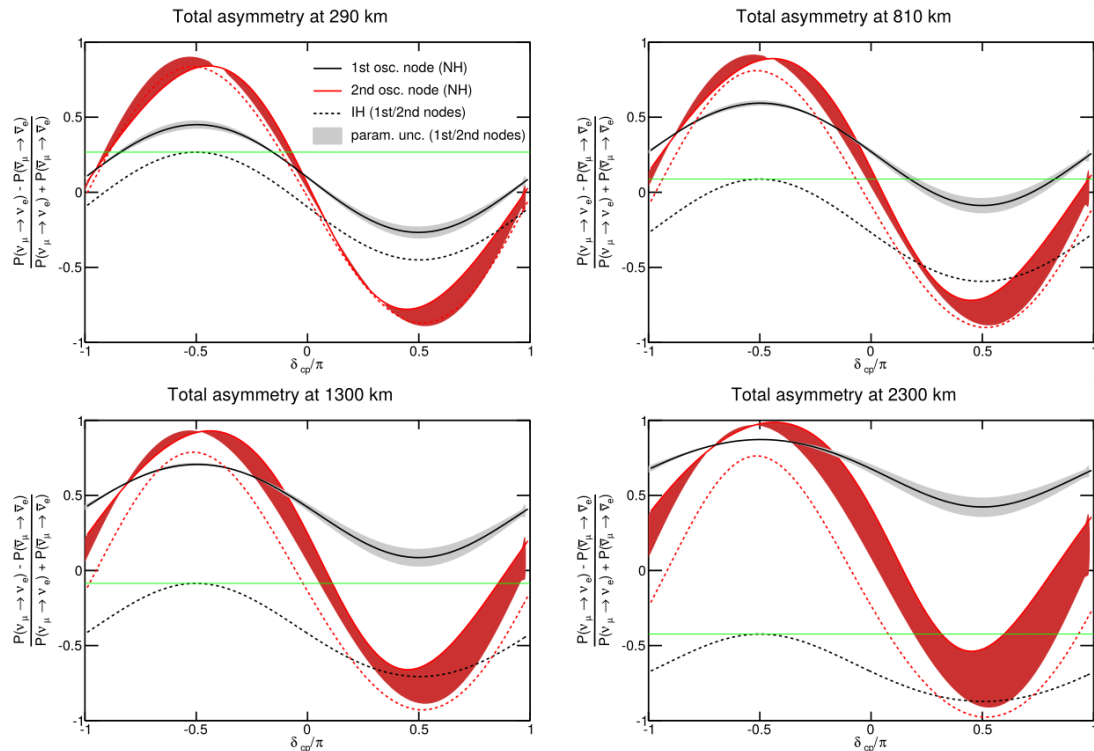$$

(2.6)

Figure 2.13: Total $\nu/\bar{\nu}$ asymmetries as a function of δ_{CP}/π for four different baselines. The black (red) lines indicate the asymmetries at the first (second) node, the full ones being for NH and the dashed ones for IH [19].

The origin of the matter effect asymmetry is simply the presence of electrons and the absence of positrons in the Earth. In the few-GeV energy range, the asymmetry from the matter effect increases with the baseline as the neutrinos pass through more matter; therefore, an experiment with a longer baseline will be more sensitive to the neutrino mass ordering. For baselines longer than 1200 km, the degeneracy between the asymmetries from matter and the CPV effects can be resolved. This can be understood looking at the two types of asymmetries; we can approximate their dependencies from the baseline length and neutrinos energy near the peaks of oscillation probability as:

$$\mathcal{A}_{CP} \propto L/E \tag{2.7}$$
$$\mathcal{A}_{matter} \propto L \times E \tag{2.8}$$

Figure 2.13 shows the total neutrino-antineutrino asymmetry $\mathcal{A}$ at the first (black) and second (red) oscillation peak, as a function of δ_{CP} for four different values of L.

Expected significance for mass ordering and δ_{CP} measurements

The evaluation of the sensitivity of the DUNE experiment is performed checking the compatibility of a particular oscillation hypothesis with the data using the likelihood for Poisson-distributed data:

$$\chi^2 = -2\ln\mathcal{L} = \sum_i^{N_{bins}} \left[M_i - D_i + D_i \ln\frac{D_i}{M_i} \right] \tag{2.9}$$

where M_i is the MC expectation in bin i and D_i is the observed value.

Comparing the theoretical spectra with the expectation in case of null hypothesis we can obtain the sensitivity in the neutrino MO and CP-violation measurements, in terms of $\Delta\chi^2$

$$\Delta\chi^2_{ordering} = \Delta\chi^2_{opposite} - \Delta\chi^2_{true} \tag{2.10}$$
$$\Delta\chi^2_{CPV} = \min\left[\Delta\chi^2_{CP}(\delta_{CP} = 0, (\delta_{CP} = \pi)\right] \tag{2.11}$$

The aim of the DUNE experiment is to determine neutrino MO with significance of $\sqrt{\Delta\chi^2} > 5$ for all possible values of δ_{CP}. This will require an exposure of 200-400 kt·MW·yr, corresponding to 7 years of data collection. Figure 2.14 shows the expected significance as a function of exposure, expressed in kt·MW·yr, while Figure 2.15 illustrates the variation of significance as a function of δ_{CP}.

2.3.3 Measurements of oscillation parameters

The DUNE experiment will improve sensitivity on the key parameters concerning $\nu_\mu - \nu_\mu$ and $\nu_\mu - \nu_e$ transitions:

- $\sin^2\theta_{23}$ and the octant of θ_{23};

- δ_{CP};

- $\sin^2\theta_{13}$;

- Δm^2_{31}.

The sensitivity to these parameters as a function of exposure is plotted in Figure 2.16.

The determination of the octant of the mixing angle θ_{23} is still an open question. The problem is whether or not its value is exactly 45°, producing maximal mixing between mass eigenstates 2 and 3. The latest results of T2K, in fact, leave both lower ($< 45°$) and upper ($> 45°$) octant scenarios open, depending on the mass hierarchy being considered. A value of θ_{23} being exactly 45 ° would hint at new not yet considered symmetries, while, for example, an excess in the upper octant of the order of the Cabibbo angle would point
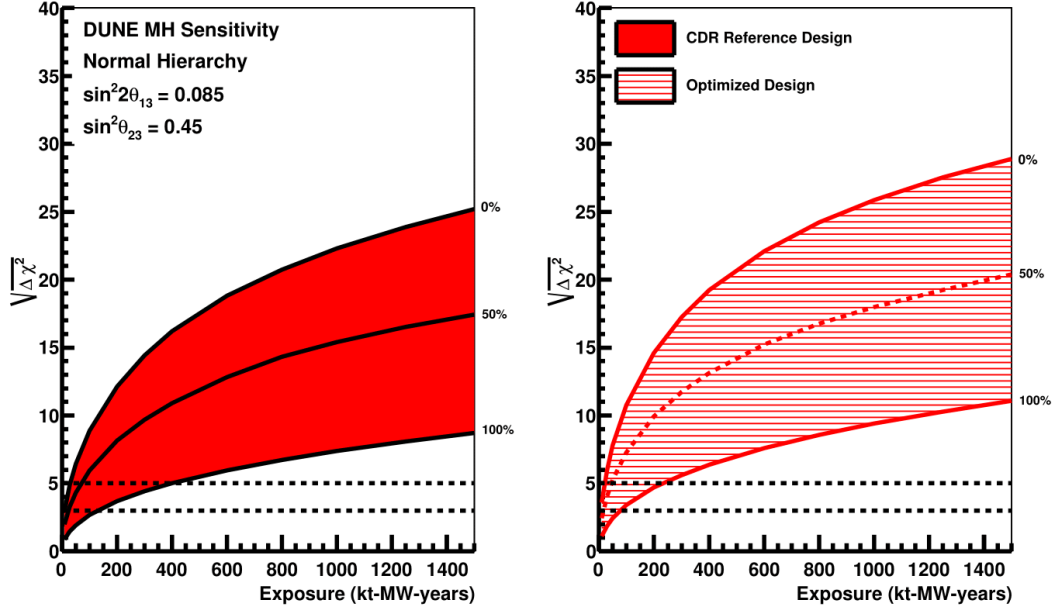
Figure 2.14: The minimum significance for the determination of mass ordering for the 100%, 50%, 0% of the δ_{CP} as a function of exposure, assuming NO.
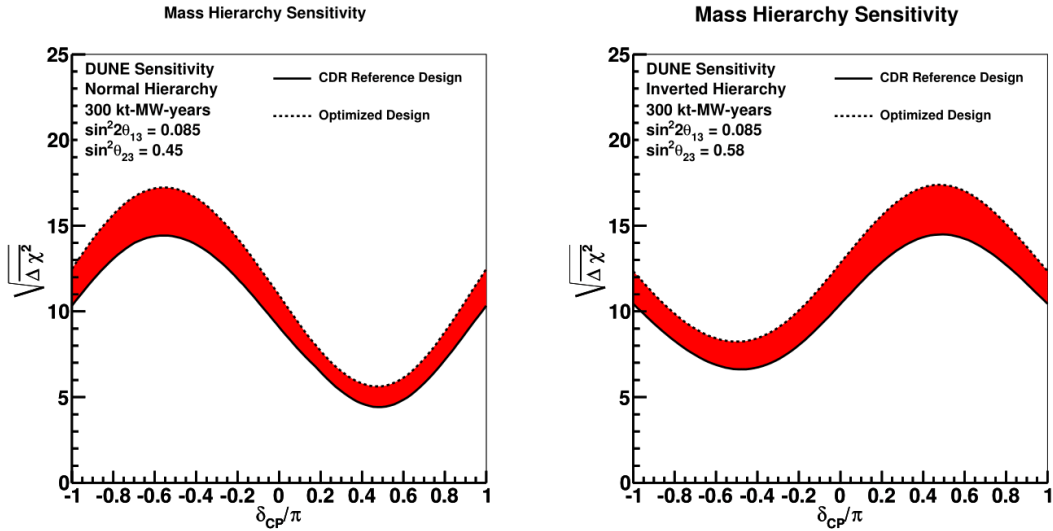
Figure 2.15: MO significance as a function of δ_{CP} for a 300 kt·MW·yr exposure. The red band is due to different beam designs.
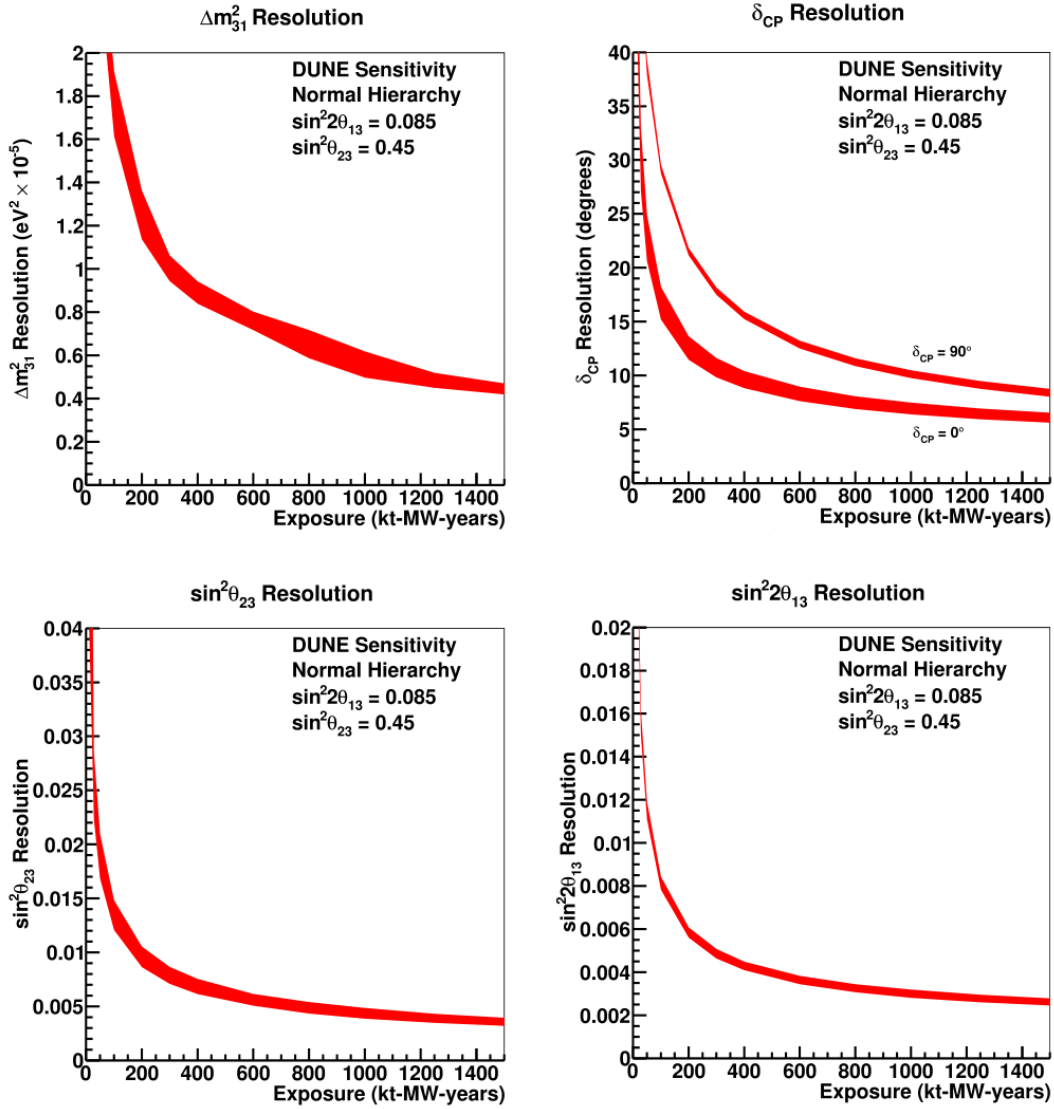
Figure 2.16: Resolution as a function of exposure for Δm_{31}^2 (upper left), δ_{CP} (upper right), $\sin^2\theta_{23}$ (bottom left) and $\sin^2\theta_{13}$ (bottom right). The red area represents the range in sensitivity due to differences in beam design.

Figure 2.17: Octant sensitivity as a function of θ_{23}. The yellow areas indicate the 1σ and 3σ intervals for the value of θ_{23} from recent global fits. The green area represents the range in sensitivity due to differences in beam design and δ_{CP} value [9].
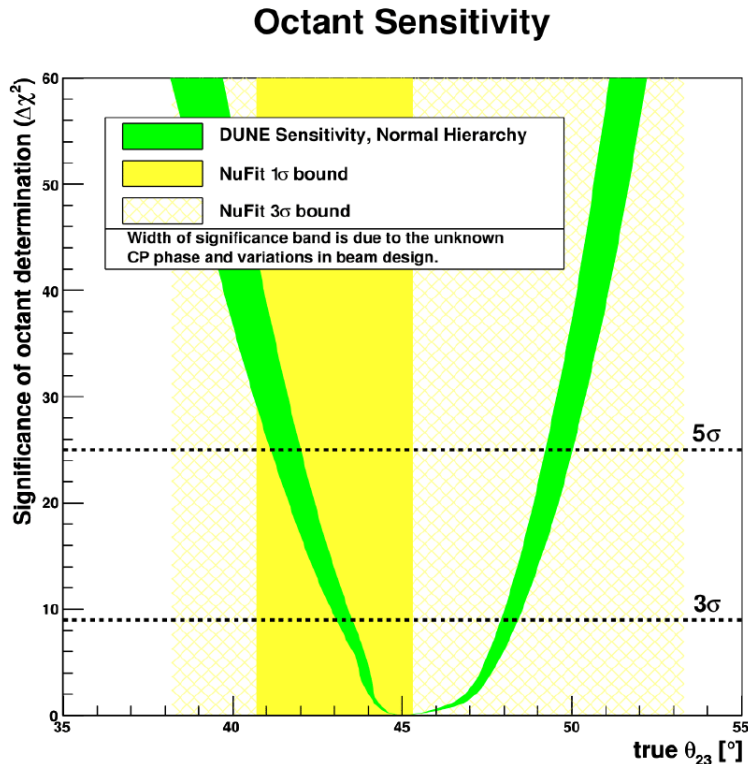
in the direction of quark-lepton universality models. The octant of θ_{23} will be determined combining the oscillation measurements of $\nu_\mu \to \nu_e$ and $\nu_\mu \to \nu_\mu$, which depend both on $\sin^2\theta_{23}$. The sensitivity to the octant as a function of θ_{23} is plotted in Figure 2.17. It is defined as

$$\Delta\chi^2_{octant} = \left| \chi_{\theta_{23}^{test}>45^\circ} - \chi_{\theta_{23}^{test}<45^\circ} \right| \tag{2.12}$$

2.3.4   Proton decay measurements

Proton decay is predicted by almost all Grand Unified Theories (GUTs), together with barion number violation. The detection of this process would be one of the only viable experimental strategies to probe these theories: the unification scale in fact is in excess of about 10^{15}GeV with respects to energies accessible to accelerator experiments.

The non-detection of proton decay instead sets proton life-time constraints and progressively rules out theories based on their predictions.
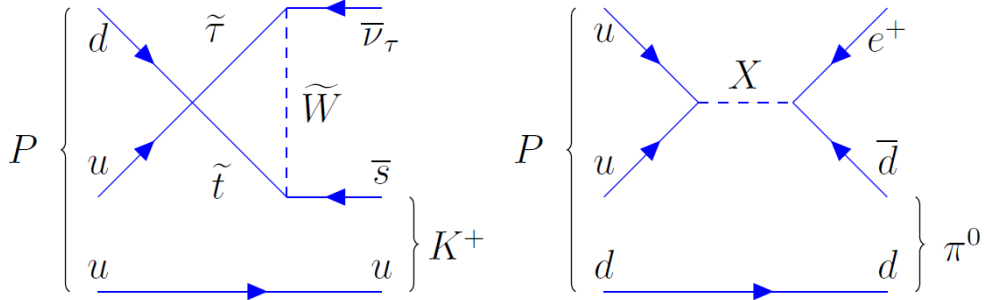
37

Figure 2.18: Feynman diagrams for two major proton decay modes: the main decay for SUSY GUTs $p^+ \to K^+\bar{\nu}$ (left) and the main decay for gauge-mediation GUTs $p^+ \to e^+\pi^0$ (right) [9].

Given the scale of energy deposition in the few hundred MeV to few GeV range, a detector optimised for neutrino oscillation physics at long baselines is naturally well suited for sensitive searches for nucleon decay. Furthermore, DUNE will have the capability to detect two dominant proton decay modes (see Figure 2.18):

$$p^+ \to K^+\bar{\nu} \tag{2.13}$$
$$p^+ \to e^+\pi^0 \tag{2.14}$$

Since Kaons have an especially high ionization rate the first decay mode is especially interesting for large LArTPCs, where Kaons would be detected with great efficiency using liquid Argon technologies. The second mode instead is better detectable by water Cherenkov experiments because the mass of the proton is converted into the electromagnetic shower energy of the positron and the photons from the decay of π^0. In Figure 2.19 several key nucleon decay channels relevant for DUNE are illustrated, along with existing experimental limits.

2.3.5   Supernova neutrino measurements

During its experimental life, estimated in ~ 20 yr, DUNE should have a 40% chance of observing neutrinos from a core collapse Supernova in the Milky Way. This would be of great importance for our understanding of this astrophysical phenomenon, which has only been confirmed in its basic characteristics by the observation of neutrino events from SN1987, a supernova in the Large Magellanic Cloud, 50 kpc away.

Supernovas also promise an extremely varied environment to study neutrino oscillation, with their initial flavour composition being strictly linked to the expanding shock and turbulence. In this case the oscillation patterns would be very different for NH and IH and furthermore, the oscillations of neutrinos and anti-neutrinos would also mani-

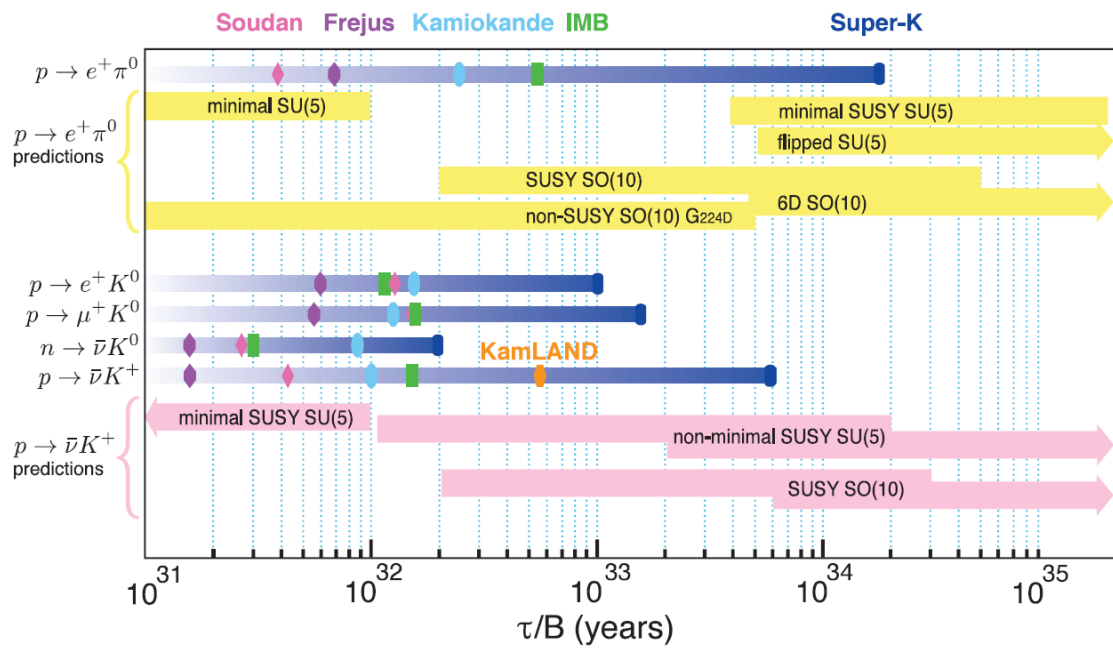Figure 2.19: Summary of nucleon decay experimental lifetime limits from past or currently running experiments for several modes, and the model predictions for the lifetimes in the two modes $p^+ \to e^+\pi^0$ and $p^+ \to K^+\bar{\nu}$. The limits shown are 90% confidence level (CL) lower limits on the partial lifetimes, τ/B, where τ is the total mean life and B is the branching fraction [13].
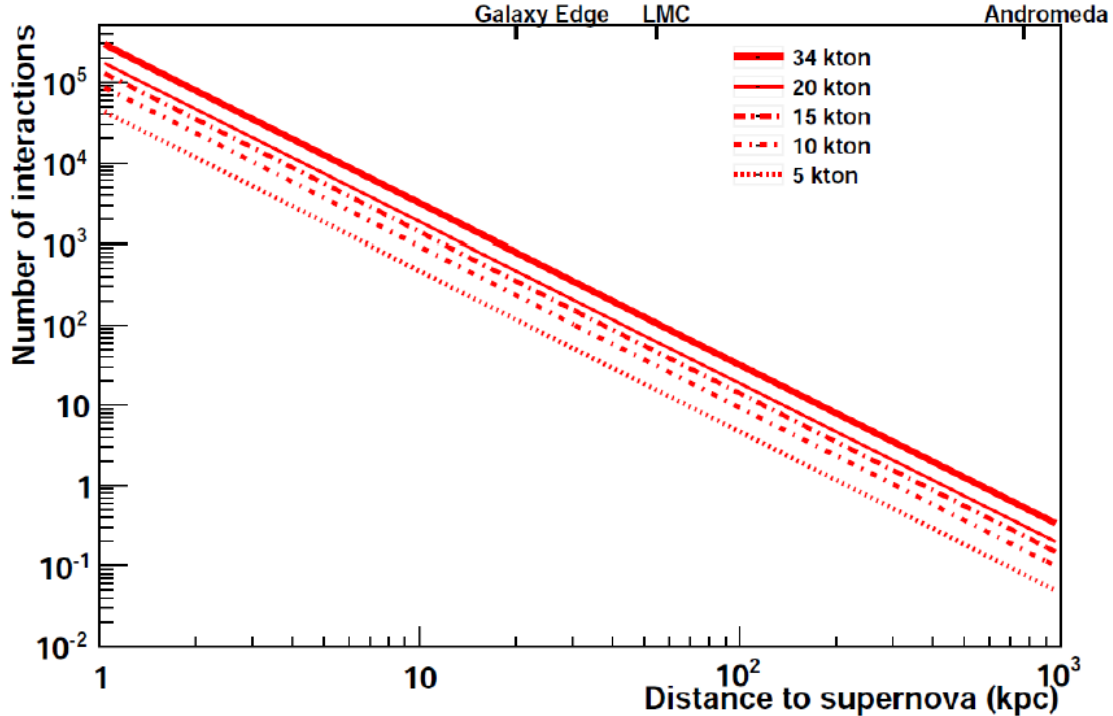
Figure 2.20: Number of core-collapse neutrino events in LAr detector as a function of distance to the supernova for different detector masses.

fest rather differently, making the observation of both with high statistics of particular interest.

Currently, experiments searching for neutrinos from a core-collapse supernova are sensitive primarily to $\bar{\nu}$'s. On the other hand, the DUNE detector will be very sensitive to the ν_e component of the flux, via the absorption interaction

$$\nu_e + {}^{40}\text{Ar} \longrightarrow e^- + {}^{40}\text{K}^*$$ (2.15)

This interaction can be identified via the coincidence of the electrons with the gamma product by the de-excitation of the ${}^{40}\text{K}^*$. Figure 2.20 illustrates the behaviour the number of signal events, which scales with mass and the inverse square of distance.

2.3.6 Oscillation physics with atmospheric neutrinos

Thanks to its large target mass and to its underground location, DUNE will be able to study atmospheric neutrino oscillations. Since the atmospheric sample contains ν's of all flavours over a vast range of energy and path lengths, including some for which matter
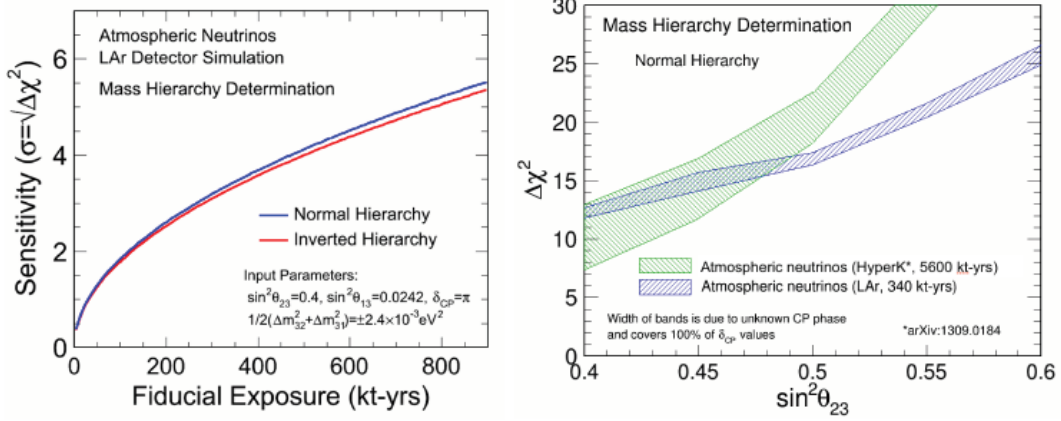
Figure 2.21: MO sensitivity as a function of exposure (left) and of the true value of θ_{23} (right) using atmospheric neutrinos. The sensitivities of the Hyper-Kamiokande experiment sensitivities are also shown for comparison.

effects are relevant, all oscillation parameters could be measured, ordering a very useful complementary program to the main accelerator one. In Figure 2.21 (right) the MO sensitivity as a function of the exposure time is shown; it is practically independent from δ_{CP} making possible to resolve some ambiguities in the mass ordering measurements made with neutrino beams.

2.3.7 Near Detector scientific program

The ND will also have a physics program of its own, independent of the FD. This programme will include measuring neutrino interactions to explore the two pillars of the standard model: electroweak physics and quantum chromodynamics. It will also explore physics beyond the standard model, searching for non-standard interactions, sterile neutrinos, dark photons, and other exotic particles.

Chapter 3

System for on-Axis Neutrino Detection

3.1 Detector components

The aim of SAND is to be a compact and multipurpose detector capable of providing calorimetry and precision tracking measurements on events produced on different materials such as Argon and Hydrogen. It will be composed by:

- a superconducting solenoid magnet, reused from the KLOE experiment;

- an electromagnetic calorimeter (ECAL), reused from the KLOE experiment;

- a low-density tracker based on Straw Tube Technology ;

- the GRAIN detector.

3.1.1 The superconducting magnet

The SAND detector will employ the existing superconducting magnet operated in the K_L^0 LOng Experiment (KLOE). The magnet was designed in conjunction with its iron yoke to produce $0.6\,\mathrm{T}$ over a $4.3\,\mathrm{m}$ long, $4.8\,\mathrm{m}$ diameter inner volume. The coil was located inside a cryostat positioned inside the return yoke (see Figure 3.1). The cooling of the coil is performed by thermo-siphoning cycles: gaseous He at $5.2\,\mathrm{K}$ was injected at $3\,\mathrm{bar}$ (absolute pressure) from the cryogenic plant and liquefied through Joule-Thomson valves into a liquid He reservoir in thermal contact with the coil. Current leads are directly cooled by liquid He, while the radiation shields are cooled by gaseous He at $70\,\mathrm{K}$ from the cryogenic plant.
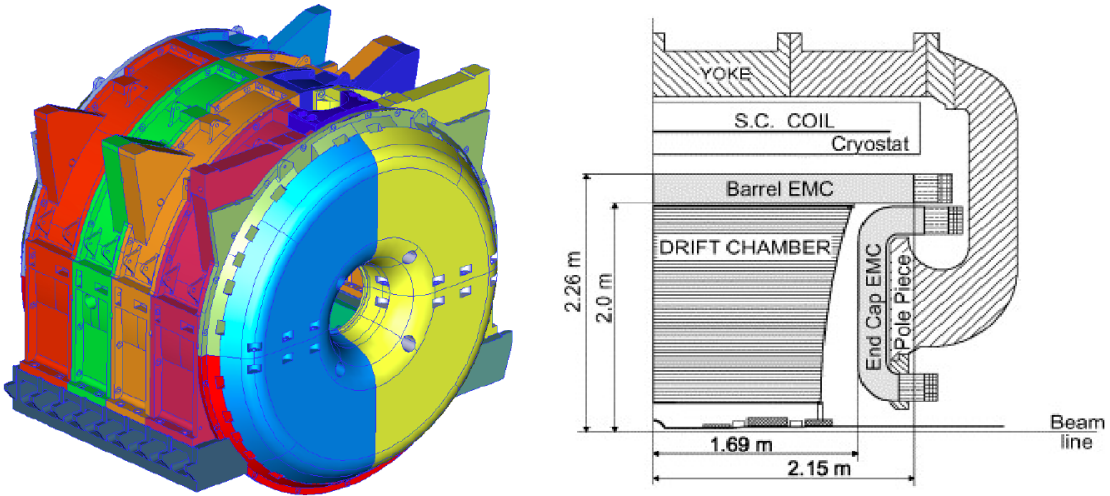
Figure 3.1: The KLOE detector: (left) 3D engineering CAD model of the magnet and (right) vertical cross section [14].

3.1.2 The electromagnetic calorimeter

The ECAL is a lead scintillating fiber sampling calorimeter, which offers a time resolution below the ns range, excellent energy resolution and 4π hermeticity. As can be seen in Figure 3.2, the calorimeter is cylindrical and is located inside the KLOE magnet, close to the coil cryostat. Two additional calorimeters (endcaps) ensure hermeticity. The barrel consists of 24 modules, each of which is 4.3 m long, 23 cm thick and trapezoidal in cross-section, with bases of 52 and 59 cm. Each end-cap consists of 32 vertical modules that are 0.7–3.9 m long and 23 cm thick. The calorimeter weight is about 100 t and the read-out system includes 4880 phototubes. Due to the large overlap of the barrel and endcaps, the KLOE calorimeter does not have an inactive gap at the interface between those components.

All ECAL modules are stacks of approximately 200 grooved, 0.5 mm thick, lead foils with 200 layers of cladded 1 mm diameter scintillating fibers, glued together with a special epoxy compatible with the fiber materials. The average density is $5\,\text{g/cm}^3$; the radiation length is $\sim 1.5\,\text{cm}$; and the total thickness of the calorimeter is ~ 15 radiation lengths. Each module is read at both ends by phototubes through a light guide to match the circular photo-cathodes. The read-out divides the calorimeter module in five layers: the first four are 4.4 cm thick while the last one is 5.2 cm thick. The readout segmentation gives an r-Φ (in the case of the barrel) or x-z (in the case of the endcaps) readout resolution of $1.3\,\text{cm}$ $(4.4/\sqrt{12}\,\text{cm})$.

The energy and time resolution of the calorimeter were evaluated in the commissioning and running phases of KLOE and were found to be

43
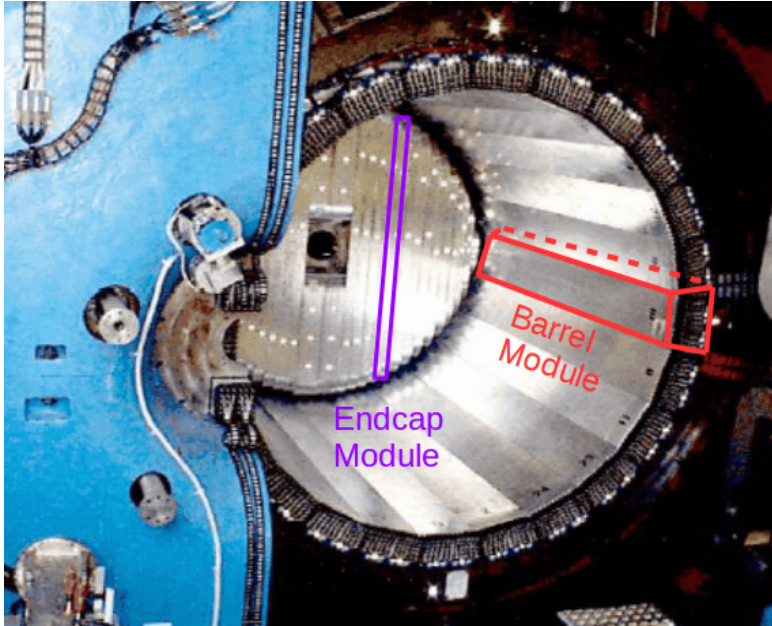
Figure 3.2: A view of the KLOE calorimeter. The far endcap is closed and ECAL modules can be seen as vertically oriented slabs. The barrel ECAL modules are slabs that have a trapezoidal cross-section and that run along the barrel. [14].

- Energy resolution: $\sigma/E = 5\%/\sqrt{E(\mathrm{GeV})}$
- Time resolution: $\sigma = 54/\sqrt{E(\mathrm{GeV})}\,\mathrm{ps}$

3.1.3 Straw Tube Tracker

The Straw Tube Tracker (STT) has been designed to:

1. Provide a high resolution in momentum, angle and space, thorough high granularity of the detector, maintaining at the same time a low density and an overall thickness of about one radiation length X_0 to minimise secondary interactions;

2. Provide a large target for neutrino interactions, with a fiducial mass of about 5 t;

3. Offer a range of different target materials;

4. Offer particle identification capability for e, π, K, p, μ;

In order to fulfill the first two requirements, apparently in contrast with each other, the neutrino target have been separated from the tracking system. To achieve the goal of keeping the detector transparent to secondary particles, the target is spread over the detector in smaller modules.

44

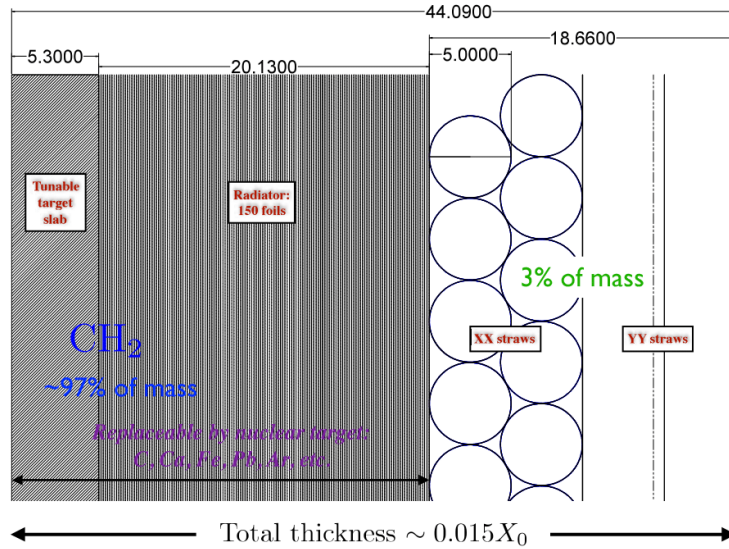Figure 3.3: Drawing of a compact STT module including three main elements (left to right): (a) a polypropylene CH_2 target; (b) a radiator with 119 polypropylene foils for $e^\pm$ ID through Transition Radiation process; (b) four straw layers XXYY (beam along z axis and B field along x axis).

The detector will be installed so that neutrino beam enters through the side of the barrel, perpendicular to the magnetic field. A system using STT, stacked in ortogonal XY planes will fill most of the magnetic volume, and the planes will be interleaved with compact CH_2 and C modules, to add mass and act as an additional target for neutrino interactions.

Looking at a single CH_2 module, it is composed of:

- a solid polypropylene (CH_2) target slab, 5.3 mm thick;

- a radiator of 150 CH_2 polypropylene foils, 15 μm thick, interposed with 120 μm air gaps. The radiator is configured in such a way as to guarantee a correct electron identification;

- 4 straw tube layers, XXYY, glued together with a straw diameter of 5 mm. It has mylar walls with total thickness of 20 μm and 70 nm Aluminium coating, Tungsten wire with 20 μm diameter and 20 nm Gold coating.

The tubes will be filled with a gas mixture of Xe/CO_2 (70/30) with an internal pressure of 1.9 atm. Figure 3.3 shows a representation of a standard module.

One of the most important feature of the STT modules is the possibility to remove the radiator and to substitute the CH_2 slab with a different nuclear target; a broad range
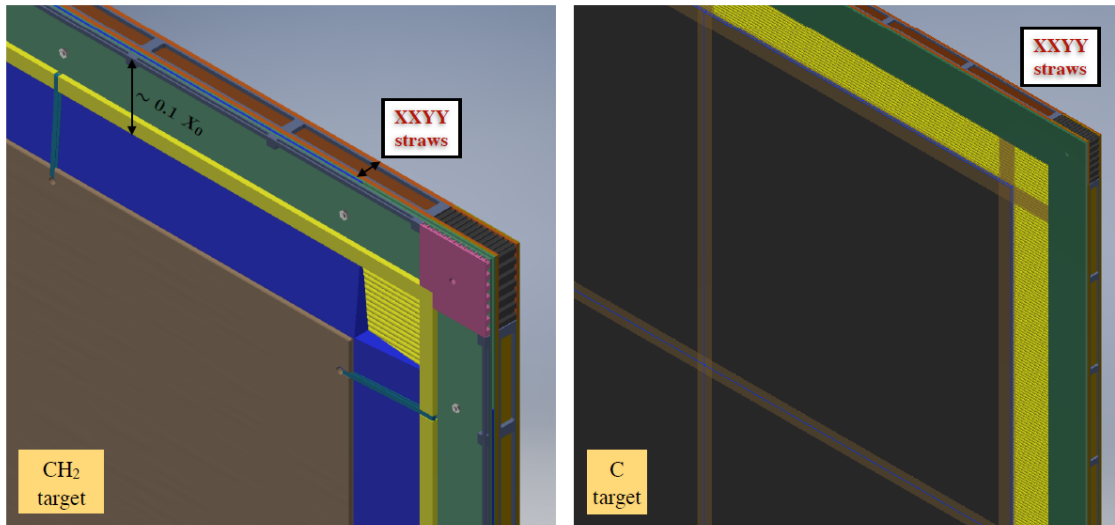
Figure 3.4: Left picture: Detailed 3D engineering CAD model of one STT module equipped with CH_2 target slab (in brown color) and radiator (in blue color). Right picture: Engineering CAD model of of one STT module equipped with graphite target (in black color). The tracking part is composed of four straw layers XXYY and is the same as in the CH_2 module on the left [32].

of target materials like C, Ca, Fe, Pb, etc. in fact can be installed in place of the target radiator, provided that they can be manufactured in the form of thin planes. Figure 3.4 shows the corresponding design of two STT modules equipped with CH_2 and graphite targets.

In summary, the STT design is overall very well equipped to meet the physics goals set for SAND. It provides a very good spatial ($< 200\,\mu$m), angular (~ 2 mrad), momentum ($\sim 3\%$) and timing resolutions, while also offering good particle identification by exploiting both the ionization dE/dx and TR for the e/π separation. The use of polypropylene targets together with the graphite ones allows the study of the neutrino interaction with hydrogen through the statistical subtraction technique. The study of neutrino interaction with hydrogen is very useful since it is free of nuclear effects which impact the neutrino interactions on other nuclei.

3.1.4 The GRAIN detector

The GRAIN detector consists of a LAr volume with a mass of the order of 1t instrumented with optical system in order to read-out the scintillation light by means of arrays of SIPMs. Currently, both Hadamard matrix and lenses are options for the optical system. The design of the cryostat is still under study and it is guided by the conflicting

requirements of reducing the material exiting particles have to cross and of sustain the LAr mass. The exact position and size of the LAr target are currently under discussion; however, recent designs suggest a volume positioned upstream, almost in direct contact with the ECAL (see Figure 4.1).

3.2 Physics program

3.2.1 Reducing the systematic uncertainties for the neutrino oscillation studies

In order to constrain the systematic uncertainties relevant for the neutrino oscillation analysis, all the varaibles that enter in eq. 2.1 need to be decoupled and measured independently:

- $\Phi(E_\nu)$: flux measurements benefit from detectors with low-density tracker materials, in order to achieve high resolution and precise neutrino energy scale measurements. SAND will be able to measure the fluxes for all (anti)neutrino flavours with high accuracy.

- $R_{phys}(E_{vis}, E_{rec})$: having in the same detector both Ar and lighter targets helps to disentangle the physics response function from R_{det}. SAND is able to constraint the physics response function thanks to the presence the LAr target and of Hydrogen target in the STT, for which $R_{phys} = 1$.

- $\sigma_X(E_\nu)$: the cross-section measurements require to have in the Near Detector the same target of the Far Detector, in this case the LAr. Once the flux is precisely measured, the cross section on Argon can be evaluated by using the large sample of interactions provided by GRAIN. The cross-section measurements need the knowledge of R_{phys} and R_{det}.

- $R_{det}(E_{vis}, E_{rec})$: the only way to evaluate the FD response factor is through measurements performed in a ND based on the same technology (LAr). Determining the $\sigma_X R_{phys}$ product is possible in SAND due to the presence of a variety of different nuclear targets.

The determination of R_{phys} separately from σ_X in STT is possible by defining a set of kinematic variables sensitive to nuclear smearing effects: the use of CC interaction samples allows us to compare the distributions of these kinematic variables from events in Ar and H targets. Comparing the measurement of $\sigma_X R_{phys}$ and the constraints on R_{phys} offered by SAND with the measurements made in the LAr ND ArgonCube makes it possible to unfold R_{det} in liquid Argon and validate the predictions for the FD.

3.2.2 Precise measurements and searches for new physics

Precise measurements in the electroweak sector

Due to SAND capabilities, it will be possible to precisely determine the weak mixing angle $\sin^2\theta_W$ in (anti)neutrino deep inelastic scattering (DIS). The strategy for measuring $\sin^2\theta_W$ will take advantage of the ratio of neutrino NC and CC DIS interactions:

$$R_\nu = \frac{\sigma_{NC}^\nu}{\sigma_{CC}^\nu}. \tag{3.1}$$

Thanks to the STT tracking capability, it will be possible to efficiently identify the ν_e CC interactions and separate the NC interactions from the CC ones, which will allow for a significant reduction in systematic uncertainties. A precision of 0.35% on $\sin^2\theta_W$ seems be achievable through ν-N DIS interactions.

Another independent way to measure $\sin^2\theta_W$ exploits the NC $\nu_e - e$ elastic scattering. This channel is not affected by hadronic uncertainties but it is limited by the low statistics due to its small cross section. Through the usage of this channel the $\sin^2\theta_W$ value can be find out from the ratio:

$$R_{\nu e} = \frac{\sigma(\bar\nu_\mu e \to \bar\nu_\mu e)}{\sigma(\nu_\mu e \to \nu_\mu e)} \tag{3.2}$$

in which the systematic uncertainties that arise from the electrons selection and identification cancel out [52]. The $\nu(\bar\nu)$-H interactions are used to measure the ν_μ and $\bar\nu_\mu$ fluxes, needed to determine $R_{\nu e}$. SAND can measure $\nu - e$ elastic events with small background (which can be calibrated in situ with data).

One possible way to increase the statistics consists in a combined analysis of the events collected in SAND and in the ND LArTPC detector. In fact, the STT reduces the systematic uncertainties while the LArTPC increases the statistics. With this method, and considering $\nu - e$ interactions, seems possible to achieve for $\sin^2\theta_W$ an overall relative precision of 1% or better.

Furthermore, since DIS and the $\nu - e$ channels are characterized by different scale of momentum transferred, they represents an excellent tool to test the running of the value of $\sin^2\theta_W$ in a single experiment.

Isospin Physics, Nucleon Structure and QCD tests

The availability of large statistics of neutrino-hydrogen interactions in SAND allows for the testing of isospin sum rules, including the Adler sum rule [2], which gives the isospin of the target, and the Gross-Llewyn-Smith(GLS) sum rule [46].

SAND will also offer a precise calibration of the energy scale uncertainties together with an excellent precision in the determination of both neutrino and antineutrino fluxes.

These peculiar feature will allow for a measurement of the structure functions and cross-sections with an accuracy comparable to the one achievable in electron-scattering experiments.

Due to the statistics and the energy reachable in DUNE, the $\nu - \bar{\nu}$ data collected by SAND could be used to perform global QCD analysis, in order to study the parton distribution functions, perturbative and non-perturbative corrections in a wide range of the transfered momenta Q^2 and Bjorken x variable. The presence of H and other various nuclear targets (Ar, C) allows to separate valence and sea quark distributions, d and u quark distributions, the strange quark s and $\bar{s}$ distributions.

Neutrino-nucleus interaction studies

Thanks to its modular structure the STT allows for the integration of many different nuclear targets. In this way, and by measuring structure functions, form factors and cross-sections, it is possible to study how the nucleon structure is modified inside a heavy nucleus. It is also important to study the final state interactions, since they can introduce a significant smearing in the reconstruction of the kinematic variables of final-state particles.

Searches for New Physics

All the precision measurements described in the previous paragraphs are potentially sensitive to many Beyond the Standard Model (BSM) effects, which would produce deviations from the SM predictions. For example, the excellent electron identification capability and resolution of the STT make SAND very suitable to test the low energy anomaly found by the MiniBooNE experiment. Among the various possible explanation that could be tested in order to understand the origin of this anomaly, which includes both SM and BSM physics, there is the oscillation into sterile neutrinos. This could be done measuring the CC ratios for both neutrinos and antineutrinos $R_{e\mu} = (\nu_e N \rightarrow e^- X)/(\nu_\mu N \rightarrow \mu^- X)$ and $\bar{R}_{e\mu} = (\bar{\nu}_e N \rightarrow e^+ X)/(\bar{\nu}_\mu N \rightarrow \mu^+ X)$ together with the NC/CC ratio $R_{\nu(\bar{\nu})p}$ as a function of L/E. These measurements would be sensitive to both appearance and disappearance anomalies in all four neutrino spectra.

In addition the SAND has an excellent sensitivity to the appearance of ν_τ, which could result from both sterile neutrino oscillations or BSM interactions. The detector can further improve the sensitivity of the ND complex to searches for Dark Sector physics including for example heavy sterile neutrinos, axions, dark photons, WIMPs and many others.

Chapter 4

The GRAIN detector

The GRAIN active liquid argon target will consist of a vessel containing $\mathcal{O}(1t)$ of Liquid Argon located in the upstream part of the magnetised volume of SAND. Its main role is to put constraints on nuclear effects and to provide a complementary Ar target permanently located on-axis for cross-calibration. Figure 4.1 shows two views of GRAIN, inside the inner volume of SAND. The LAr target will be $\sim 1X_0$ thick along the beam direction in order to reduce energy loss, showering, and multiple scattering of particles that will enter the downstram STT and calorimeter detectors.

The cryostat walls will be made of carbon fiber composite material reinforced by thin internal aluminium foils. The exact positioning, size and shape of the active target are still in the process of optimization.

The novelty of GRAIN is its ability to reconstruct neutrino interactions using *only scintillation light*. It will be instrumented with an optical detection system to collect Liquid argon scintillation photons which are emitted in a narrow band centered around 128 nm, known as Vacuum Ultra Violet (VUV) light.

4.1 The GRAIN design

In this section, the relevant dimensions and parameters of the GRAIN LAr active target are presented.

The inner volume of the cryostat has a width (along the x axis) of 130 cm, with elliptical sides (in the $y - z$ plane) 147.6 cm high and 47.5 cm long, respectively along the y and z axes. The direction of the neutrino beam in the simulations is along the positive z-axis. A scheme of the inner volume of the GRAIN is shown in Figure 4.2.
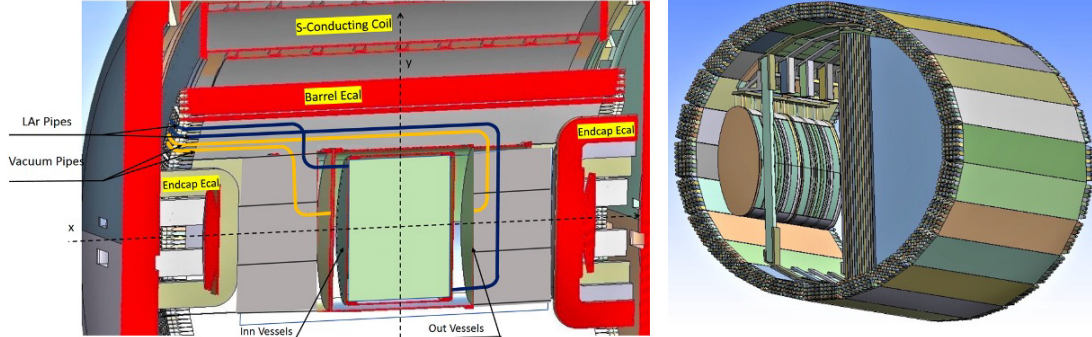
Figure 4.1: Left picture: cutaway view of the inner volume of SAND, showing the position and vessel structure of GRAIN. Right picture: view of the inner volume detectors of SAND with the KLOE calorimeter and an STT module on the right. The GRAIN cryostat is on the left. The neutrino beam comes from the left, perpendicularly to the axis of the cylinder.
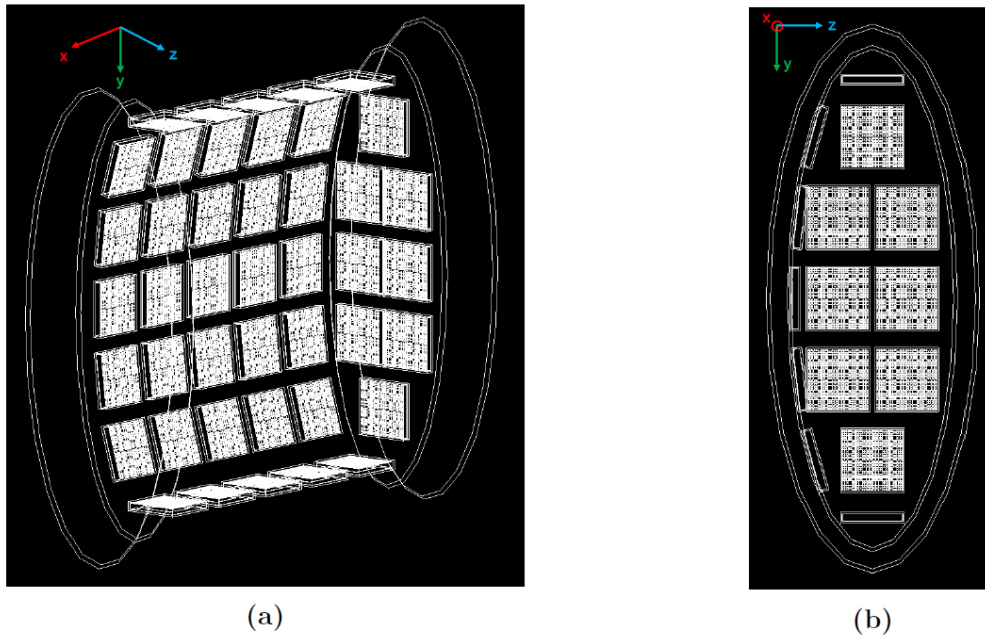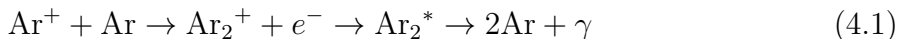

Figure 4.2: Frontal (a) and side (b) views of the GRAIN geometry. The chosen disposition of the cameras maximises their number. In (a) the front-facing side is cut to allow a better view of the inner volume. The neutrino beam direction is along the positive z-axis. The front facing side has been cut for better viewing.

51

4.1.1   Scintillation in LAr

LAr scintillation photons are emitted in the Vacuum Ultra Violet in a 10 nm band centred around 127 nm with a time profile made by two components with very different characteristic decay times, a fast one in the nanosecond range and a slower one in the microsecond range.

The passage of ionising particles in LAr produces pairs of positively charged argon ions (Ar^+) and free electrons and also produces excited atoms (Ar^*). When they couple to neutral Ar atoms, ionized Ar_2^+ or excited Ar_2^* argon dimers are produced. The first one eventually recombines with a thermalised electron producing Ar_2^*. In both processes (recombination and excitation), the decay of the final state results in the emission of vacuum ultraviolet (VUV) photons.

$$Ar^+ + Ar \rightarrow Ar_2^+ + e^- \rightarrow Ar_2^* \rightarrow 2Ar + \gamma \tag{4.1}$$

$$Ar^* + Ar \rightarrow Ar_2^* \rightarrow 2Ar + \gamma \tag{4.2}$$

Ar_2^* has two possible states, a singlet ($^1\Sigma_u^+$) and a triplet ($^3\Sigma_u^+$) state. The singlet transition to the ground state Ar_2 has a short decay time $\tau_{fast} \sim 6$ ns, while the triplet transition to the same ground state is allowed only because of spin-orbit coupling and has a much longer lifetime $\tau_{slow} \sim 1.6\,\mu$s.

The scintillation photon yield of LAr depends on the ionizing particle type and on the Linear Energy Transfer (LET). The highest photon yield is reached by relativistic heavy nuclei, from Ne to La. Low LET light particles (e^-, p) have a slightly reduced photon yield because a fraction of the ionisation electrons escape from recombination.

The optical properties of this medium are not well known yet: controversial measurements or calculations exist for the refractive index or the Rayleigh scattering length at the LAr emission wavelength. Table 4.1 gives a brief overview of current knowledge of these parameters. Two recent experimental observations in particular can not be easily explained with the current understanding of the LAr scintillation process. The DUNE Collaboration has reported a clear dependence of the lifetime of the triplet state $^3\Sigma_u^+$ of the Ar_2^* dimer on the applied electric field [51]. Scintillation light was produced by a sample of cosmic muons that crossed the 4-ton prototype of the dual-phase DUNE detector [7], in which light was detected with an array of five 8" photomultipliers (Hamamatsu R5912-02Mod) coated with TPB [56], to convert 127 nm photons to 430 nm and the electric field was varied between 0 and 600 V/cm.

The second experimental evidence is related to the doping of LAr with small concentrations of xenon. As can be seen from Figure 4.3 reported that adding a few tens of ppm of xenon to LAr has the effect of shifting the wavelength of the triplet component from 127 nm to 174 nm, shortening the signal from few μs to hundreds of ns and enhancing the Light Yield (LY). The enhancement of LY can not be explained by an higher quantum efficiency of the wavelength shifter (TPB) for 174 nm than for 127 nm, since it has been measured to be almost the same [27] and should be attributed to an increase of the LAr

Parameter	Value	Measured/Calculated by:
Refractive index n	1.37	(calc.)[43]
	1.47 ± 0.07	(calc.)[45]
Attenuation length (cm)	66 ± 3	(exp.)[55]
	52 ± 7	(exp.)[24]
	> 110	(exp.)[1]
Rayleigh scattering length (cm)	90	(calc.)[43]
	55 ± 5	(calc.)[45]

Table 4.1: Summary of the current knowledge of the optical properties for liquid argon at its scintillation wavelength, from calculations (calc.) and measurements (exp.). The wide range of values for the Rayleigh scattering length is related to the spread in values of the refractive index [16].

photon yield. These two effects point to quenching processes of the triplet states and to an hidden amount of light which has not been described before. The effect produced by LAr doping with Xe can have important consequences for light detection: it helps to increase the photon detection efficiency in the case of both lenses and masks.

The scintillation properties of liquid argon allow to perform both spatial and calorimetric measurements by means of an optical detection system capable of collecting the VUV scintillation emission. The two kind of measurements are discussed in Sections 4.3 and 5.1, respectively.

4.1.2   Photon detection system

Conventional SiPMs have a high efficiency peaking at 400–500 nm and in general no sensitivity for VUV light. The sensitivity has been further extended to below 150 nm and now even at the VUV region with quantum efficiency at the level of 17% [21].

The imaging system is composed of 76 cameras, 8 on each elliptical side, 25 on each of the curved faces, and 10 on the top and bottom of the inner volume along the x-axis, five on each side. This number of cameras is the highest that is possible to insert into the vessel, given their dimensions. Each camera is a 32×32 pixel matrix of SiPM sensors, with a size of 3.2 mm and pixels separated by 0.2 mm, resulting in a total detector side length of 102.4 mm. Several detector geometries, with different pixel sizes, have been tested to find the best set-up. The thickness of the detector assembly is 1 mm. The sides of the camera are enclosed by a 1 mm thick layer of a yet to be chosen opaque material. The SiPM sensors should have a Photon Detection Efficiency (PDE) of $\sim 25\%$, however it has still to be measured since the sensors need to be coupled to some wavelength-shifter, such as polyethylene naphthalate (PEN) and tetraPhenyl butadiene (TPB), and the use of Xe-doped LAr (see Section 4.1.1). ProtoDUNE-DP for example, uses PMTs
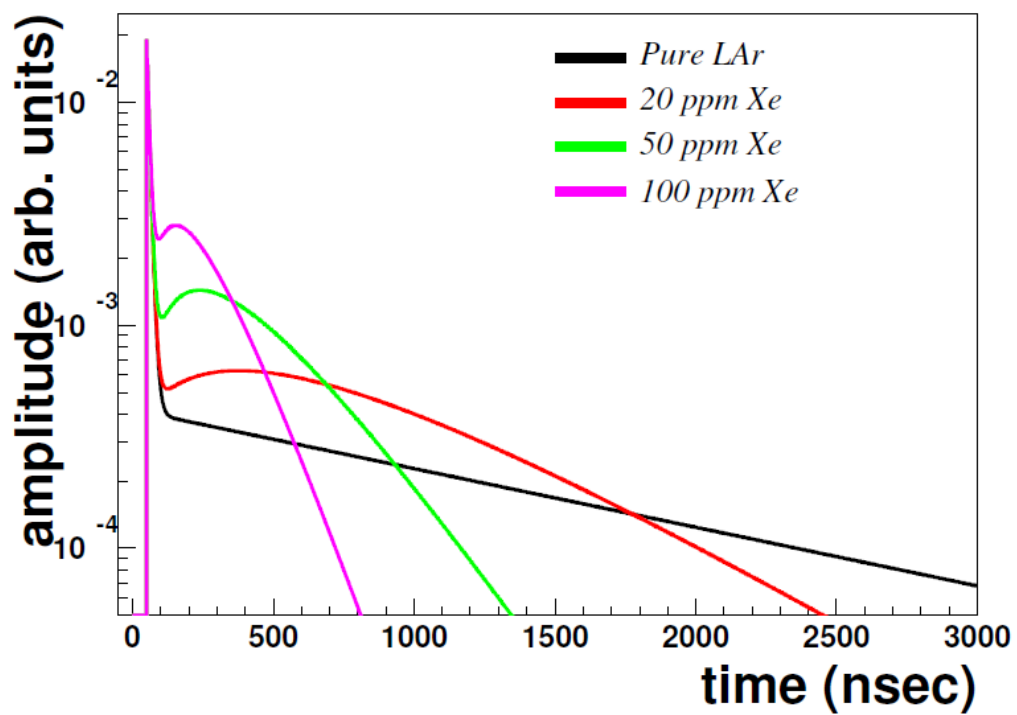
Figure 4.3: Waveforms of xenon doped liquid argon at different xenon concentrations as predicted by the model. The waveforms represent the sum of LAr and xenon shifted light[57].

either covered with PEN foils or directly coated with TPB. While TPB is broadly used, PEN is a novel material, never used before in such a large scale experiment and whose efficiency is not well known. Both PEN and TPB have a maximum of re-emitted photons around a wavelength of 430nm [39, 20].

In Table 4.2 the main parameters of the GRAIN design are shown.

Cryostat dimensions		Detector parameters	
Width	130 cm	Pixels per side	32
Height	147.6 cm	Pixel edge	0.2 mm
Length	47.5 cm	Pixel size	3 mm
Total volume	0.91 m^3	Detector thick.	1 mm
Fiducial vol.	0.49 m^3	Detector side	102.4 mm

Table 4.2: Summary of the relevant dimensions of the design of GRAIN.

4.2   Simulation tools

4.2.1   Monte Carlo simulations of neutrino events with GENIE

Until quite recently, most of the neutrino experiments developed their own neutrino event generator, each optimized for the energies, nuclear targets, detectors and physics topics relevant for the experiment. Today particular importance is given to the neutrino energy region of few GeV, since these energies are relevant for some of the current and future Long-Baseline accelerator experiments such as DUNE.

GENIE is a ROOT-based MC neutrino event generator designed using object-oriented methodologies and developed entirely in C++. It is adopted by the majority of the neutrino experiments [10]. The long-therm goal of GENIE is to be a canonical neutrino-interaction generator whose validity is extended to all nuclear targets and neutrino flavours over a wide spectrum of energies, from a few MeV to some PeV.

GENIE takes as input a neutrino flux and a geometry representation and gives as output a file that records event information regarding the simulated process. In particular, for each event, GENIE returns a list of particles that exit the struck nucleus after the scattering interactions, hadronizations, and final-state interactions.

GENIE and Geant4 takes in input a geometry representation, which for the SAND detector is provided through a Geometry Description Markup Language (GDML) file. Figures 4.4 and 4.5 represent the SAND layout with its main components generated starting from the geometric description.
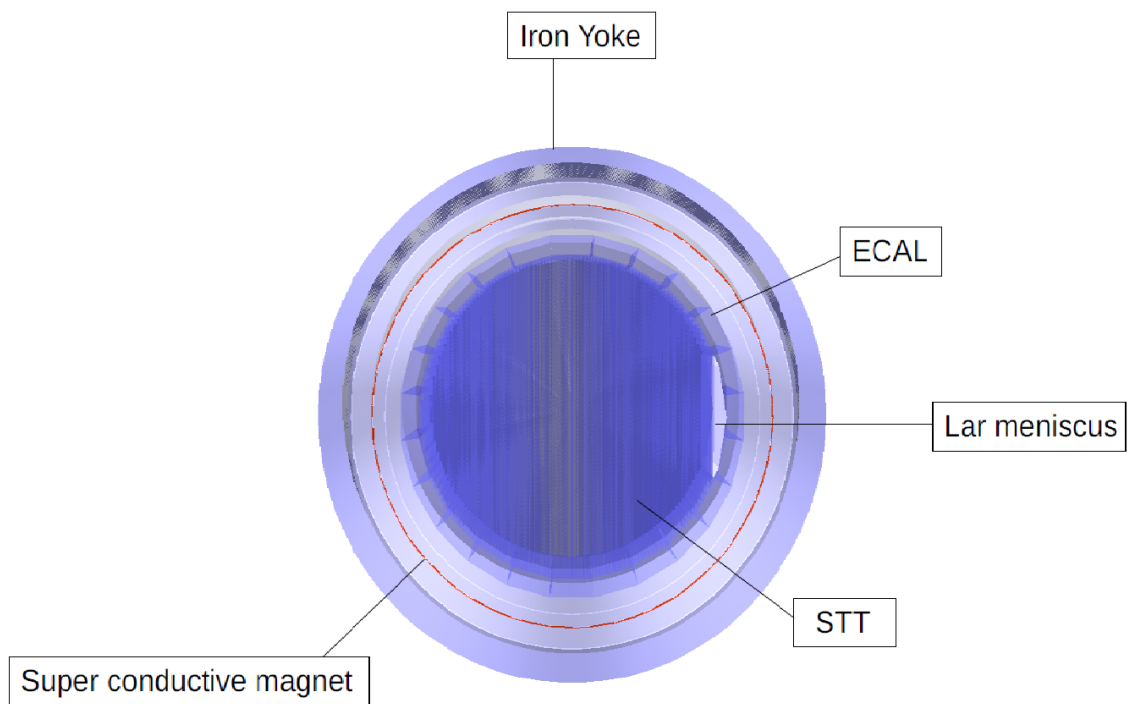
Figure 4.4: Lateral view of SAND geometry with its main components. The neutrino beam direction is from the right to the left.
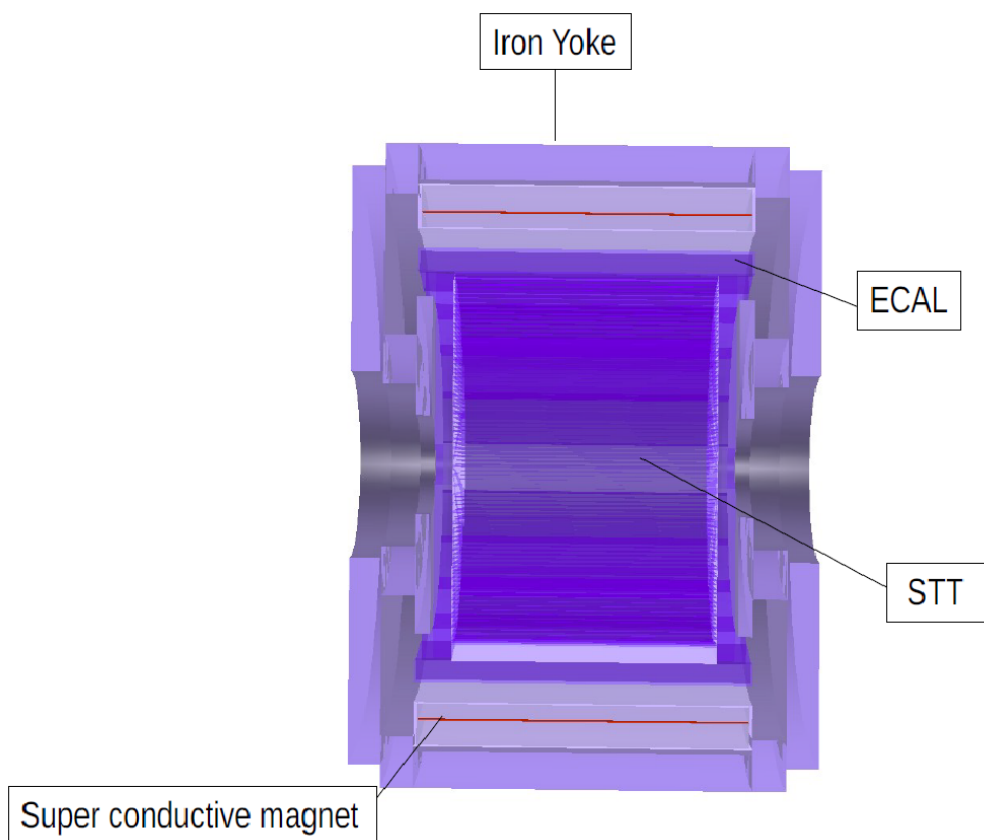
Figure 4.5: Front view of SAND geometry with its main components. The neutrino beam direction is toward the page.

4.2.2 Particle propagation with EDEP-SIM

The energy deposition simulation (edep-sim) is the official program employed by the DUNE collaboration. It is a GEANT4 software package that aims to simulate particle propagation and geometry-related problems [40]. This simulation implements a fairly detailed model of the energy deposited as ionization and scintillation.

Edep-sim takes as input a particle kinematic file and a geometry file, supporting several kinematic particle file format including the ones produced by GENIE. The output is a standard ROOT file containing:

- **TGeoManager object**: with detector geometry;

- **TG4Event tree**: with the event data. It contains all the most relevant information for each event, such as event ID, primary particles, particle trajectories, and energy deposition on the detectors.

4.3 Vertex reconstruction

The expected number of neutrino interactions in the overall SAND detector (yoke, magnet, ECAL, STT, GRAIN) is ~ 90 per spill, while in GRAIN is ~ 0.1.

LArTPC technology uses both the scintillation light emitted by the argon and the electrons produced by ionisation. At the Far Detector, the Vacuum Ultra Violet (VUV) scintillation light is shifted by means of a wavelength shifter and collected to provide information on the deposited energy and the timing of the event, while the drift of the ionization charges is used for the topological reconstruction of the event.

However, because of the relatively slow drift of the electrons, of $\sim 1.5 \, \text{mm}/\mu\text{s}$ at $500 \, \text{V/cm}$ and $85 \, \text{K}$ [59], a set-up similar to the one of the Far Detector will have a time response of the order of some milliseconds and could not be suitable for a high rate of particles due to the pileup of the events. To solve this problem, an alternative and innovative approach, able to provide a much faster response could be to use the scintillation light not only for calorimetric measurements, but also to provide the spatial reconstruction of the event.

LAr can be used for imaging purposes since it is transparent to its own scintillation emission (see Table 4.1). This, in turn, requires an optical system capable of collecting enough light and a fast and segmented photodetector capable of providing adequate resolution.

In the following sections two different imaging techniques are described: the first one makes use of coded aperture masks while the second employs lenses.

MURA 37x37   MURA 43x43

Figure 4.6: Examples of MURA masks of different ranks.

4.3.1 Coded aperture imaging

Coded Aperture Imaging techniques were applied in the 1970s in the field of X-ray imaging, becoming a leading technique in X-ray and gamma ray astronomy [44, 54]. In its original formulation, a *coded aperture mask* is formed by many pinholes arranged according to some specific pattern. A mask coupled to the detector forms a Coded Aperture Camera. Mask designs currently being considered for the GRAIN optical readout system are based on the Modified Uniformly Redundant Array (MURA) family of coded aperture patterns (see Figure 4.6). An important property of MURAs is the throughput of the aperture, i.e. the fraction of open elements with respect to the total number, is always around 50%.

Each point of a light source will project a shadow of the aperture on the detector surface and the overall pattern of lights and shadows can be processed, generating a reconstructed 2D image of the original object [41]. In the case of a point source, a single pinhole counting s photons would have a SNR=$\sqrt{s}$, according to Poisson statistics; for a Coded Aperture with N holes instead, the total average count and variance would be Ns, giving a SNR=$\sqrt{Ns}$.

Using a combination of 2D images from different points of view, it is possible to generate a three-dimensional image. The 3D analytical reconstruction was still being developed at the time of writing this dissertation. The main difficulty for this technique is the formation of fake artifacts during the 2D image deconvolution process, due to the fact that this method was originally created for astrophysical light sources, located at the infinite, while in this case photons are originated at a mean distance of $\sim 50\,\mathrm{cm}$ from the masks, with the particle tracks being almost never parallel to the mask surface. Furthermore the exposure time is much smaller than the one available for an astronomic
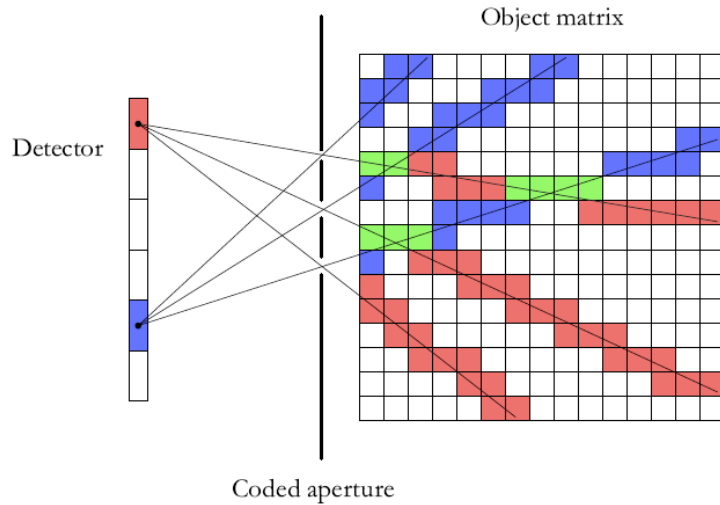
Figure 4.7: Simplified view of the combinatorial approach: for each detected photon, a probability amplitude (red and blue) is projected in the segmented volume through all possible mask holes. The green pixels indicate where the amplitudes sum up.

measurement, so that the low Photon Detection Effciency (PDE) of sensors (just 20-25%) to the VUV scintillation emission is a serious problem.

A reconstruction algorithm that can be employed in conjunction with Coded Aperture Imaging techniques and is able to directly reconstruct a 3D image is currently under development. It adopts a combinatorial approach: for each detected photon, project a probability amplitude in the LAr volume through all possible mask holes (see Figure 4.7). The volume of the vessel is ideally segmented into smaller volumes, called voxels. Each hit is then propagated back into the LAr volume with an appropriate weight assigned to voxels. The probability amplitude of each voxel is computed summing the amplitudes from all the hits.

When a proper cut is applied to the probability amplitude, it should be possible to reconstruct the particle tracks. One of the problem which arises however is the low contrast between signal and background which requires a dedicated algorithm to find the best cut to maximize the S/N ratio.

The combinatorial method can employ any multiple pinhole mask (but some masks patterns may be more effective than others) and it is well-suited to operate with low light-yields, as the probability propagation is done for each photon individually. Its only main drawback is that it is computationally heavy, requiring GPU acceleration for the computation of the amplitude projection weights.
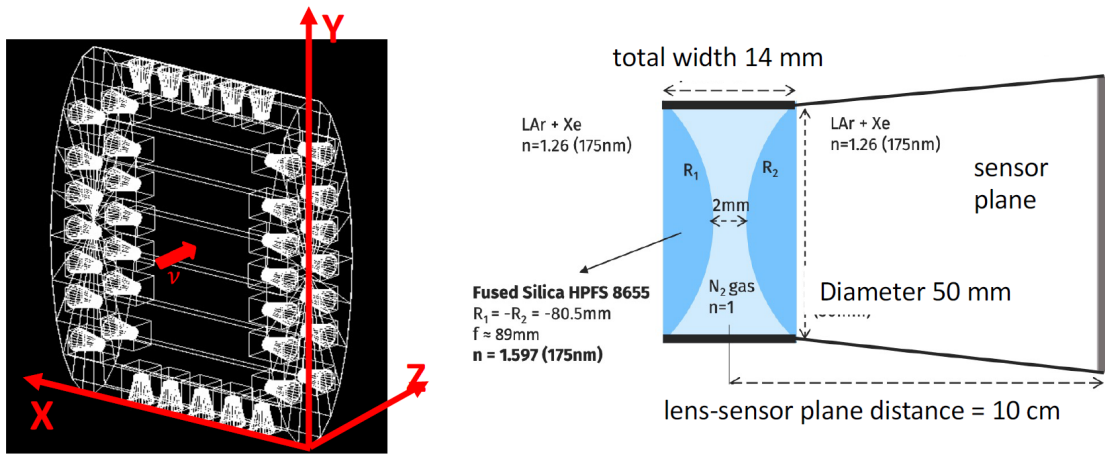
Figure 4.8

4.3.2 Vertex reconstruction with lenses

A more classical approach adopts optical lenses. The liquid argon scintillation light, however, is emitted with a wavelength in the Vacuum-Ultra-Violet region, for which lenses' and mirrors' transmission is highly inefficient. The lens material must therefore:

- have high transmittance;

- have a refractive index different from that of LAr (not known precisely, 1.26-1.4);

- be suitable in cryogenic environment.

A preliminary design envisages 38 pixelated SiPM cameras coupled to optical lenses, as shown in Figure 4.8. Using lenses, the sensor response is already the final image and no other manipulation (such as the deconvolution process performed in the mask case) of the signal is needed.

61

Chapter 5

Energy calibration

5.1 Calorimetry

The main purpose of this thesis work is to investigate the possibility of getting energy information from the scintillation photons collected by the cameras. Reconstruction of the energy released by a charged particle moving in LAr would provide a better constraint on the incoming neutrino energy.

In order to be able to perform an energy reconstruction, the detector must be calibrated using samples of MC events. Knowing the energy deposited in LAr by particles from the simulation, it is possible to compare it with the number of detected photons obtained from the detector response simulation. For this thesis I used 8 million events with the primary interaction vertex uniformly distributed within GRAIN, comprehending all types of neutrino interactions.

The number of photons detected by the cameras depends on *where* the photons have been emitted *i.e.* on the distance between production point and a particular camera. The work for this thesis tried to discover whether or not it is possible to find a unique calibration coefficient for the LAr volume. A first answer may come from Figures 5.1 and 5.2: in the latter a larger spread is visible with respect to the first plot. Therefore, given this apparent impossibility to compute a coefficient for every point of the volume, we choose to divide it into smaller volumes in which we assumed the calibration coefficient to be uniform. Our first choice was $5 \times 5 \times 5\,\mathrm{cm}^3$ cubes, however the $10 \times 10 \times 10\,\mathrm{cm}^3$ possibility has been investigated, too. The possibility of assuming a constant calibration coefficient inside the cube volume is justified by the fact that the attenuation length for light in liquid argon is of $\mathcal{O}(1)\mathrm{m}$.

The emission of Cherenkov light could be a source of asymmetry in light detection, since it is directional; however, the number of emitted Cherenkov photons is negligible with respect to that of scintillation photons, due to the high light yield of LAr.

The analysis of MC events is done through a simulation chain that starts with an
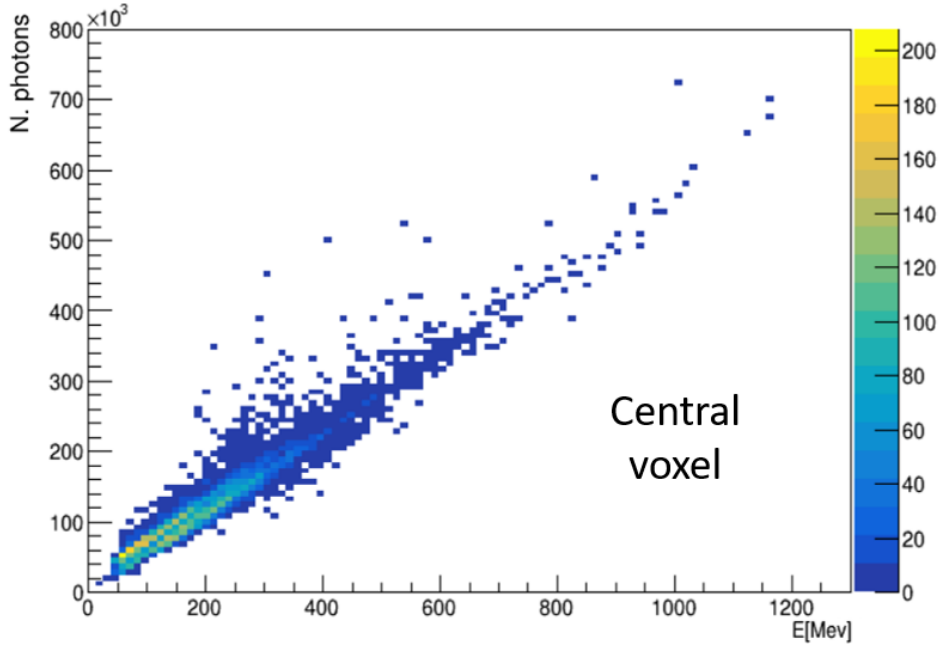
Figure 5.1: Detected photons for ν_μ CCQE interaction in the central cube as a function of deposited energy (from EDepSim). A sample of 10000 events has been used.

edepsim file, simulates the optical photon propagation and the detector response giving as output data which can be analysed to retrieve physical information such as trajectory or energy of particles (see Figure 5.3). In this way it is possible to test the design and the performance of the detector.

5.2 Detector response simulation

The simulation of the detector response is a crucial step in the simulation chain. It emulates the photon detection of SiPMs and the following signal processing which leads to the determination of the number of photons that arrived on each pixel of a camera.

This information then can be used for tracking purposes or, in this case, to determine the total number of photons produced by the passage of a charged particle in LAr. The computation of a calibration coefficient for the LAr volume requires high statistics and hence lots of neutrino events. The current software used for the detector response, called *Full Response*, gives a detailed reconstruction of the read-out system. Because of its accuracy the Full Response simulation takes a lot of time to run.

The simulation of some thousands of events has to be repeated for each cube: the high number of cubes (22906 for a cube side of 5 cm), together with the long computational time of the Full response, would result in an excessively long duration of the entire
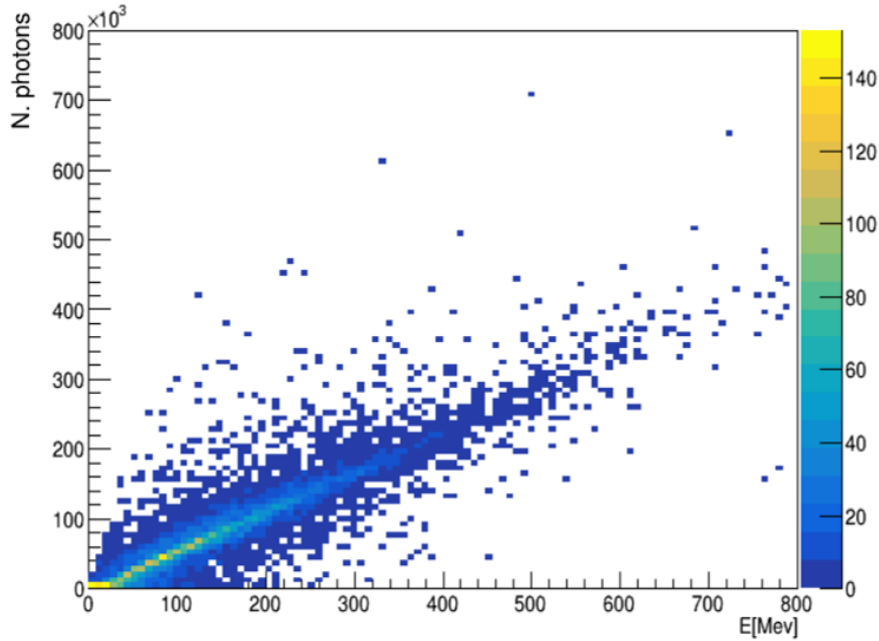
Figure 5.2: Detected photons for ν_μ CCQE interaction uniformly distributed in GRAIN as a function of deposited energy (from EDepSim). A sample of 10000 events has been used.

process. In order to mitigate the problem, the following approach has been adopted:

- Creation of a faster and approximated detector response.

- Calibration of only 1/8 of the LAr volume. As a result of the symmetries of the vessel, the rest of the volume will be calibrated by consequence.

- Reduction of LAr light yield from $40\,000$ photons/MeV to 4000 photons/MeV.

Part of my work for this thesis has been dedicated to the creation of a new detector response, which I called *Fast-Calo Response*, since it is devoted to calorimetric studies, and to its validation, comparing it with the Full Response. Section 5.2.1 describes both the Full and Fast-Calo Responses, highlighting their differences, while Section 5.2.2 shows the studies performed for the Fast-Calo validation.

5.2.1   Full and Fast-Calo Responses

Full Response

Full-Response software emulates the behaviour of a particular Data Acquisition System (DAQ) to photon detection by SiPMs. Since now, different integrated circuit (IC) chips
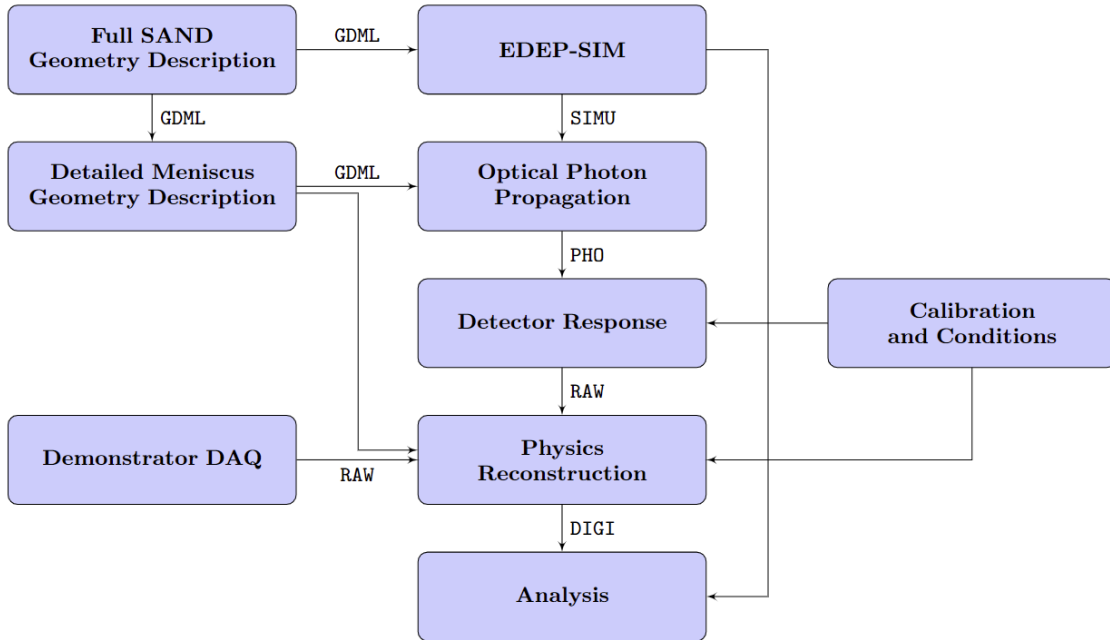
Figure 5.3: Complete data flow diagram.

have been tested, among which it is worth mentioning the *triroc* and *alcor* ASICs. In particular, the first is the one employed for the current simulations, while the second ASIC is going to be refined for future usage. Both alcor and triroc are already existing chips that have been chosen for these simulations only for practical reasons. In the next few years, a dedicated custom ASIC will have to be created for specific use in GRAIN.

For a given electronics, the Full Response simulates waveform signal formation resulting from a photon hitting a SiPM; from the analysis of the signal should be possible to count the number of photons arrived.

Triroc is a highly configurable SiPM readout ASIC intended for PET prototyping with time-of-flight capability. This 64-channel ASIC incorporates a dual triggering system that will flag the arrival photons and provides energy cut-off at a specified level [50]. This chip integrates the signal coming from photoelectrons over a certain time interval with a Time-to-Digital Converter (TDC); the number of photons is extracted by performing a conversion of the integrated charge to the photon number, while the rising edge of the waveform provides the time information.

The choice of a 200 ns integration time allows to exclude most of the slow component of the scintillation light, as can be seen in Figure 4.3. In case of multiple events in fact it would produce the superposition of the signals, preventing their individual analysis. A detailed study on the proper integration time however has still to be carried out, to better understand the effect of the superposition of the slow component emission from
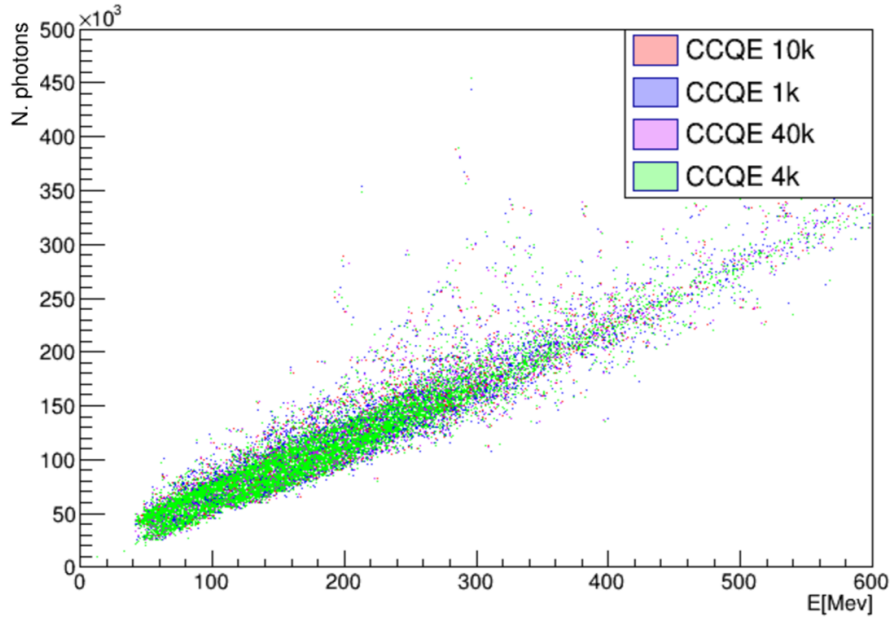
Figure 5.4: Detected photons (scaled to 40 000 photons/MeV) as a function of MC energy for light yields of 40 000 photons/MeV (pink), 10 000 photons/MeV (orange), 4000 photons/MeV (green), and 1000 photons/MeV (violet).

an event with the fast component of the subsequent event.

Alcor instead is a mixed-signal ASIC developed to readout silicon photomultipliers at low temperature. The chip is designed in a 110 nm CMOS technology. The alcor chip will provide both single photon counting and Time-over-Threshold (ToT) modes [3]. The latter can obtain not only trigger timing information as an output signal rise edge but also incident radiation energy as an output signal time width. In single photon counting mode an event rate of up to 5 MHz per channel can be accommodated. The time resolution is 50 ps and the target power consumption is less than 5 mW per channel. For now, this application is under implementation.

Fast-Calo Response

For what concerns the Fast-Calo Response, instead, it is straightforward to check that its functioning is much simpler, avoiding the simulation of the signal waveform and its subsequent elaboration by directly counting the number of photons that arrive on the camera surface. Some operations are then performed on this quantity, trying to take into account the main features of the read-out system:

- Check whether photons hit an active area: between each pixel of a camera there is a dead area of 0.2 mm width. Only photons that hit the active area can be
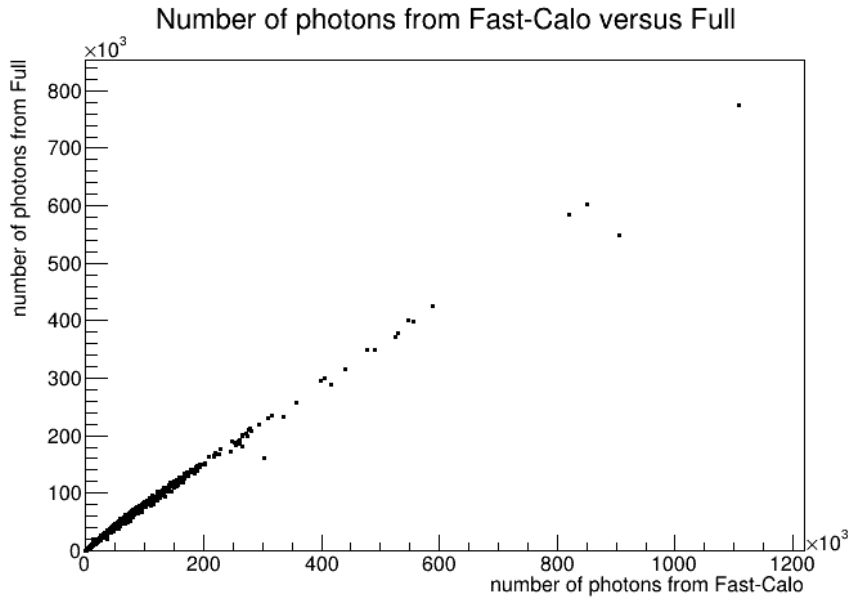
Figure 5.5: Comparison between the total number of detected photons inside the LAr vessel, obtained from Full and Fast-Calo Response simulations. A total amount of 1000 events have been simulated.

detected.

- Apply a PDE: 25% photon detection efficiency for SiPMs has been considered.

- Consider a cross-talk probability of 7% *i.e.* a finite probability for the photoelectrons produced in a sensor pixel to generate an electron-ion avalanche in a nearby pixel.

- Consider a finite integration time: as for the Full Response the integration time has been set to 200 ns.

- Consider an uncertainty on signal amplitude: to better approximate the real situation, each detected photon generates a signal (in arbitrary units) whose amplitude follows a Gaussian distribution peaked at 1 and with a 0.10 standard deviation.

These operations are repeated for each camera of the detector, while PDE and cross-talk probabilities are only preliminary values, waiting for the final choice of SiPM sensors.

The structure of this new detector response allows for a much faster execution time, producing at the same time an output comparable with that from the Full Response. The latter fact being confirmed by the analysis described in Section 5.2.2.
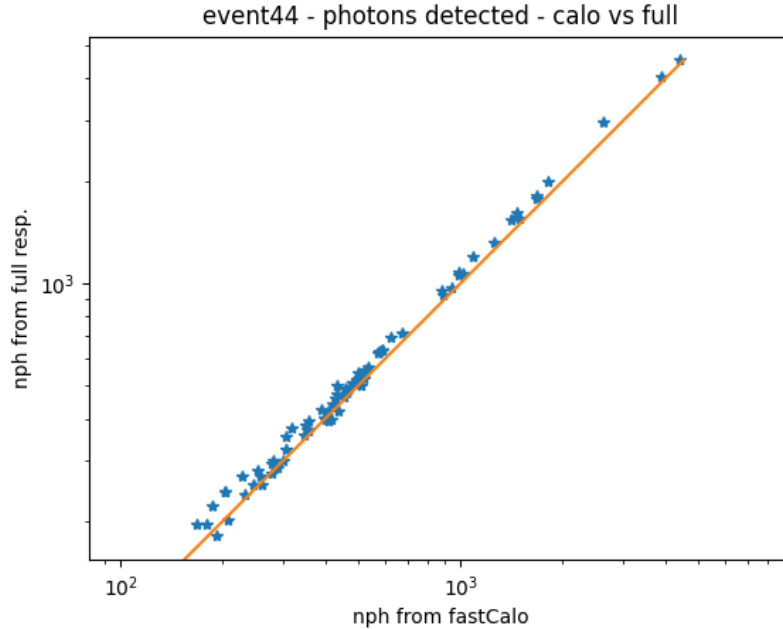
Figure 5.6: Comparison between the number of detected photons by the cameras for event n°44, obtained from Full and Fast-Calo Response simulations. A total amount of 1000 events have been simulated.

5.2.2 Preliminary verification

Before proceeding with the energy calibration of the liquid argon volume, it is mandatory to check the validity of the choices made to speed up the event simulation, which consists of the reduction of the light yield and in the use of the Fast-Calo Response.

Light yield reduction

The long time required to process the propagation of scintillation photons forced the reduction of the LAr light yield (LY), from $40\,000\,\text{photons/MeV}$ to $4000\,\text{photons/MeV}$. Figure 5.4 shows the comparison between the number of photons detected by the cameras using the Full Response simulation as a function of the deposited MC energy for different light yields of LAr; each data set is properly scaled to $40\,000\,\text{photons/MeV}$.

This result clearly highlights a good proportionality between the two simulations, and LY reduction leads only to a scaling in the number of detected photons. The choice of $4000\,\text{photons/MeV}$ LY is the best compromise between a fast simulation time and a sufficient number of photons detected by SiPMs, to provide enough statistics for the subsequent analysis.
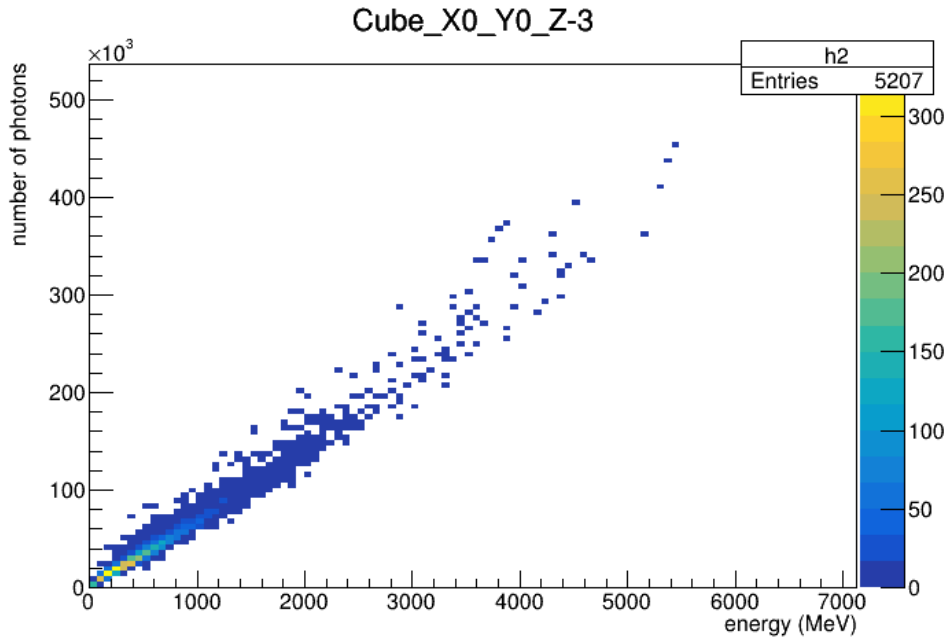
Figure 5.7: Number of photons detected as a function of deposited MC energy, from the Fast-Calo Response simulation.

Fast-Calo Response validation

The validation of the Fast-Calo Response aims to find a proportionality between the output of the Full and Fast-Calo Responses. In this way, one is authorised at using this faster but approximated simulation. For this purpose, 1000 events have been analysed with the two software and the result is shown in Figure 5.5, where the total number of photons collected by the cameras of the LAr vessel is used.

Obviously, for a correct comparison, the parameters of the two simulations, in particular the integration time, PDE, and cross-talk probability, have to be the same.

This kind of comparison has also been performed for each camera of the detector, plotting the number of photons from Fast-Calo and Full Response. Figure 5.6 reports as an example the photons detected by the cameras for Event 44.

5.3   Fit and results

After these preliminary steps, it is possible to proceed with the calibration of the GRAIN volume. In order to be as clear as possible, Cube_X0_Y0_Z-3 is taken as an example. In Figure 5.7 the number of photons detected is displayed as a function of the energy deposit. The calibration coefficient is extracted fitting this distribution with a straight line, shown
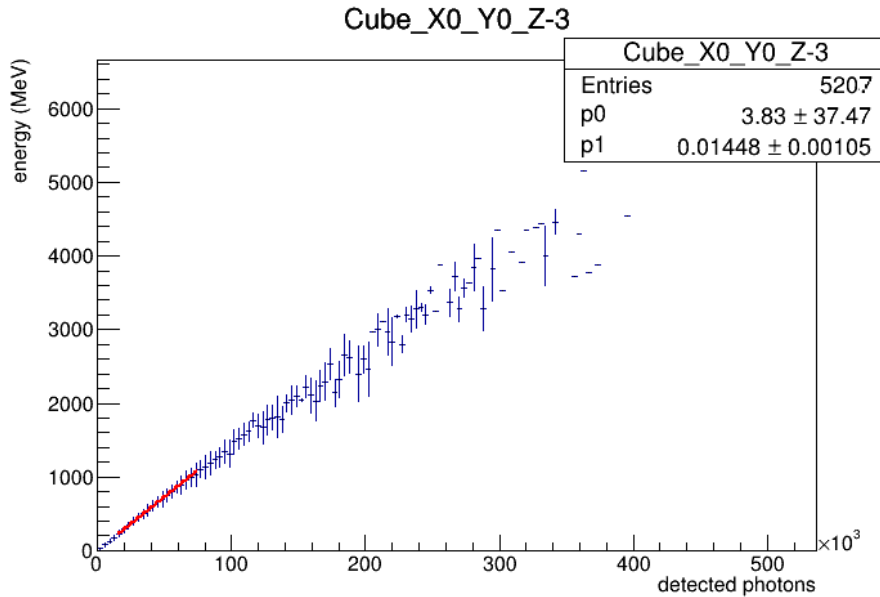
Figure 5.8: Number of photons detected as a function of deposited MC energy, from the Fast-Calo Response simulation. The distribution is fitted with a linear model in which $p0$ is the slope and $p1$ the intercept.

in Figure 5.8. The range of the fit was chosen to avoid the change in slope that occurs at higher energies (in this case around 1.6 GeV). Its origin has to be investigated since it could be due to a leakage of statistics or to a different phenomenon.

At this point, it is possible to verify whether the calibration succeeded by trying to reconstruct the energy deposited by the charged particles using the number of detected photons. Figure 5.9 provide a comparison between the reconstructed energy deposit and the Monte Carlo information from edep-sim which, to a first degree, display a good linear dependence.

A more detailed analysis of the energy reconstruction can be performed by plotting the difference between the reconstructed and Monte Carlo energy, normalised to the MC energy: $(E_{MC} - E_{reco})/E_{MC}$ (see Figure 5.10).

Figure 5.11 instead contains the 1-dimensional residual histogram, with the following characteristics:

- the distribution is peaked at around zero;

- the distribution is asymmetric with respect to negative values, which means that in this case the deposited energy has a higher probability of being overestimated;

The energy resolution of the GRAIN detector can be calculated by fitting the distribution of σ_E/E as a function of the reconstructed energy, where σ_E is the uncertainty about
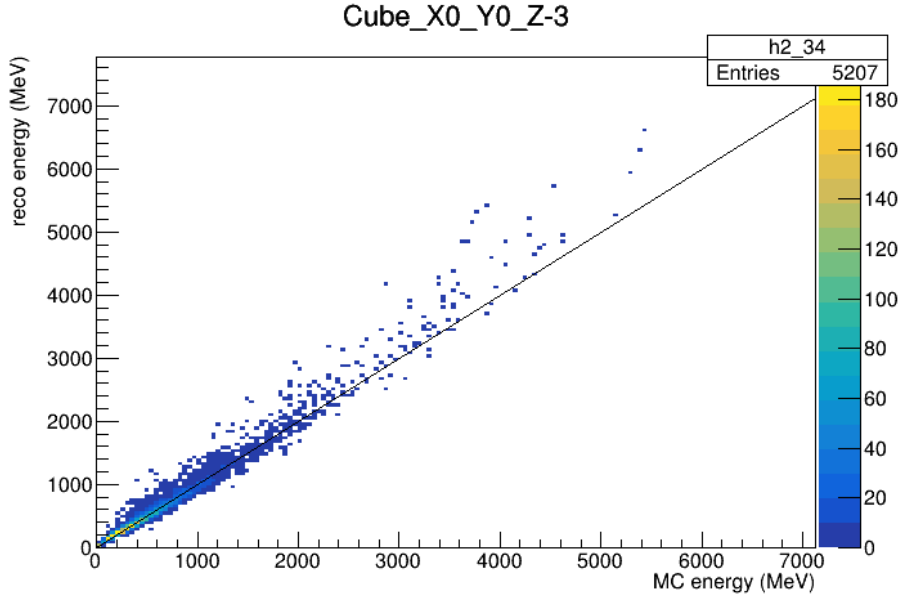
70

Figure 5.9: Reconstructed energy deposit as a function of Monte Carlo energy deposit. The straight line indicates the bisector of the quadrant.

the reconstructed energy. Once again the range of the fit was chosen to avoid the region in which a non-linearity between the number of detected photons and the MC deposited energy was found. The general expression for the energy resolution of a calorimeter is:

$$\frac{\sigma_E}{E} = \frac{a}{\sqrt{E}} \oplus \frac{b}{E} \oplus c \tag{5.1}$$

where a is the stochastic term, due to fluctuations in the number of signal generating processes, b represents the noise in readout electronics, and c is a constant term resulting from imperfections in calorimeter construction (dimension variations) and non-uniform detector response. Figure 5.12 shows the energy resolution calculated for Cube_X0_Y0_Z-3.

10 cm cube side

Despite the good results for energy resolution, one of the problems encountered during the analysis is the not excessively high number of events in each cube, which ranges from a few thousands down to a few hundreds, leading to poor statistics in some cubes. To amend this statistics leakage, calibration has also been performed on larger cubes of 10 cm side, applying the same procedures. Figures 5.13, 5.14, and 5.15 show the results of the energy calibration for the $10 \times 10 \times 10\,\mathrm{cm}^3$ Cube_X1_Y1_Z-2, since it encompasses the 5 cm side Cube_X0_Y0_Z-3.
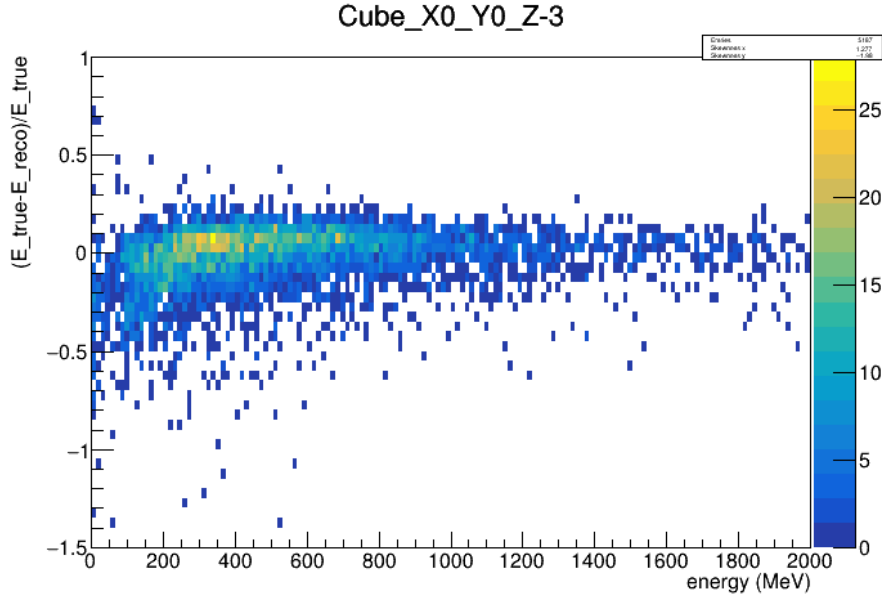
Figure 5.10: 2D plot of $(E_{MC} - E_{reco})/E_{MC}$ as a function of deposited MC energy.

General results on energy calibration

The residual plot highlights an overestimation of the energy deposit at low energies. A possible explanation could be due to the so called "blinded" cameras, which are those matrices traversed by a charged particle as it travel inside the LAr vessel. Their energy deposition on the camera pixels causes the latter to saturate. In this case the signal produced is higher than the energy deposited by the particle in LAr. The verification of this hypothesis will require further studies.

Indeed, the foreseen pathway will be the development of a machine learning algorithm able to identify blinded cameras from the photon distribution on the camera, without using the edep-sim information.

From the energy calibration of 1/8 of the GRAIN volume, a distribution of the calibration coefficient has finally been extracted. Figure 5.16 display the distributions obtained from cubes of 5 cm and 10 cm side.

These results show a non-negligible spread in the coefficient values, for both the two kinds of cubes. The mean values of the two distributions almost coincide, even if the number of the analysed 10 cm cubes is not so high. Despite these drawbacks, an attempt to calculate the energy resolution for the whole LAr vessel can be made: using the mean value of the calibration coefficient from the 5 cm cubes distribution, the plot of Figure 5.17 is created. This choice is supported by the fact that small spread of the coefficient values allows one to ignore the spatial information of the neutrino event.
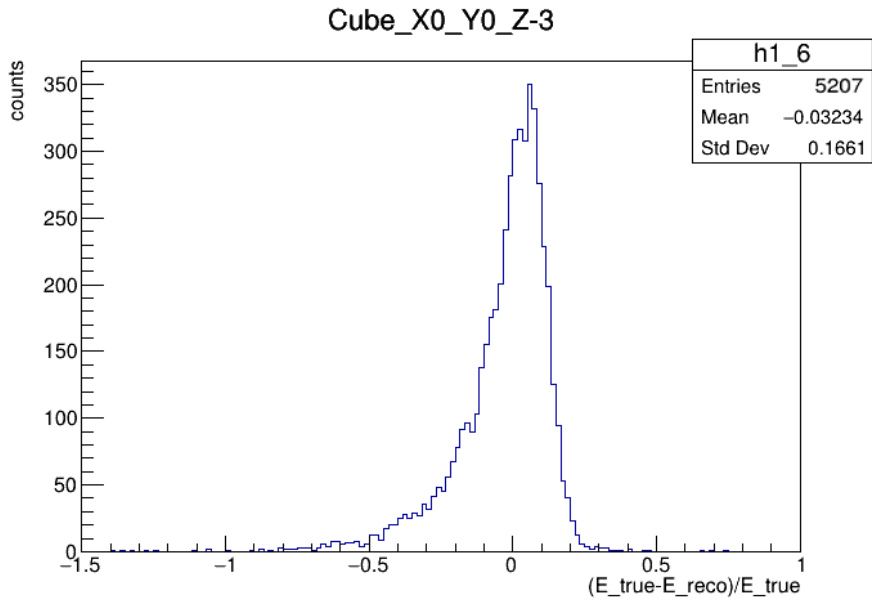
72

Figure 5.11: Histogram of the residuals, normalised to Monte Carlo energy $(E_{MC} - E_{reco})/E_{MC}$.

Figure 5.12: Energy resolution σ_E/E plotted as a function of the reconstructed energy deposit, for Cube_X0_Y0_Z-3. The points are fitted with the general expression for the energy resolution of eq. 5.3, in the range of linearity found between number of detected photons and MC energy. The parameters $p0$, $p1$ and $p2$ correspond to factors a, b and c, respectively.
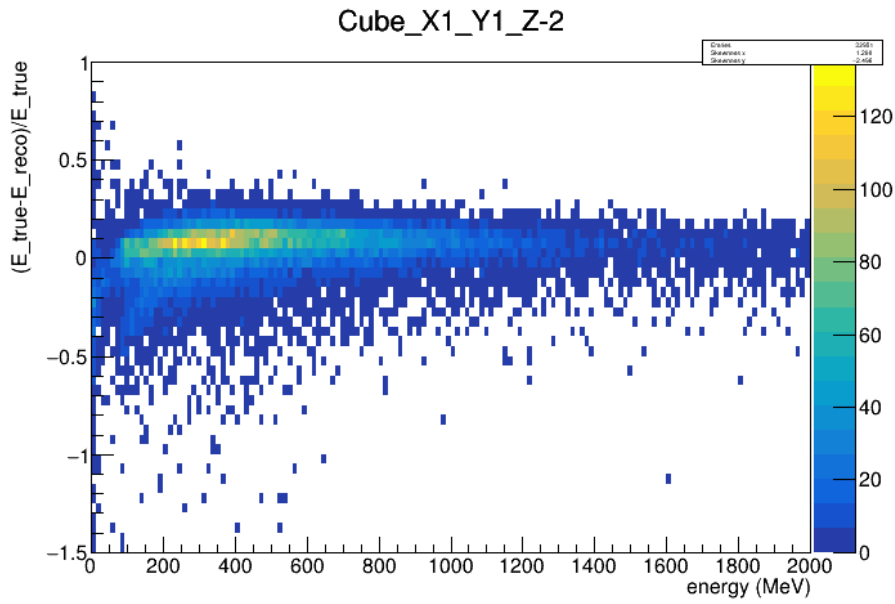
Figure 5.13: 2D plot of $(E_{MC} - E_{reco})/E_{MC}$ as a function of deposited MC energy for $10 \times 10 \times 10\,\text{cm}^3$ cubes.
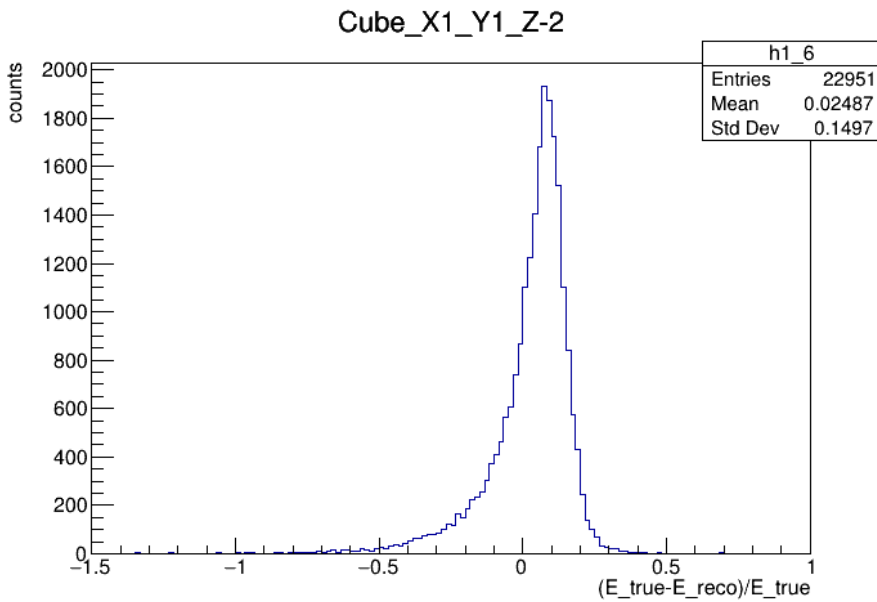
Figure 5.14: Histogram of the residuals, normalised to Monte Carlo energy $(E_{MC} - E_{reco})/E_{MC}$ for $10 \times 10 \times 10\,\text{cm}^3$ cubes.
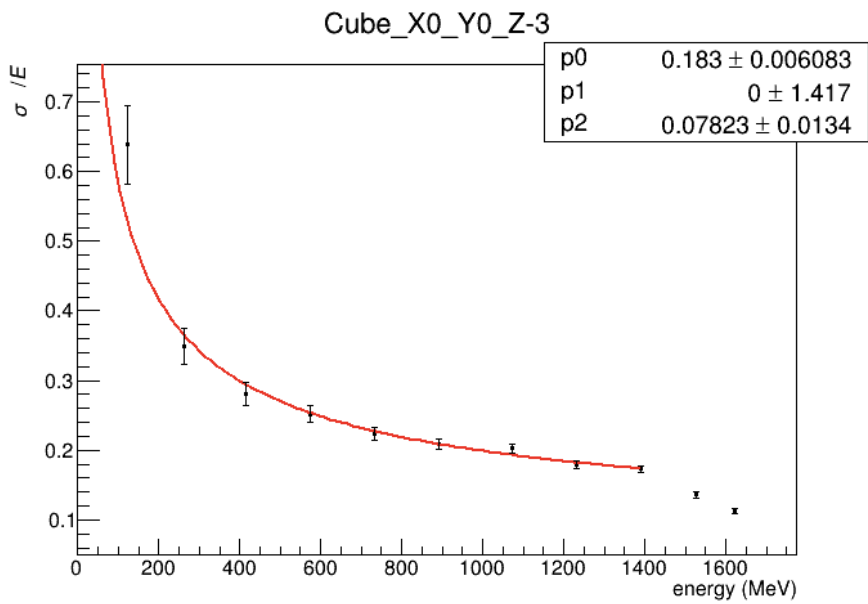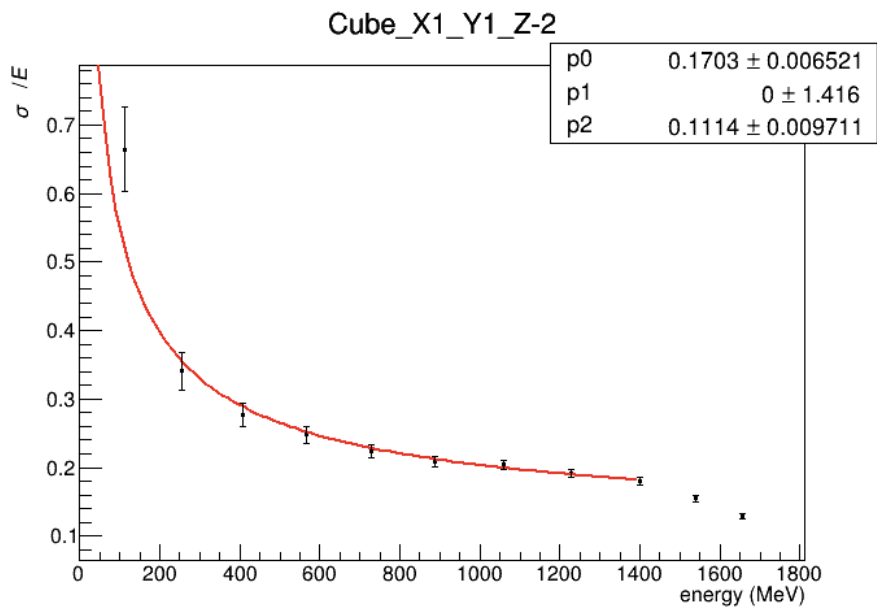
Figure 5.15: Energy resolution σ_E/E plotted as a function of the reconstructed energy deposit, for Cube_X1_Y1_Z-2. The points are fitted with the general expression for the energy resolution of eq. 5.3. The parameters $p0$, $p1$ and $p2$ correspond to factors a, b and c, respectively.
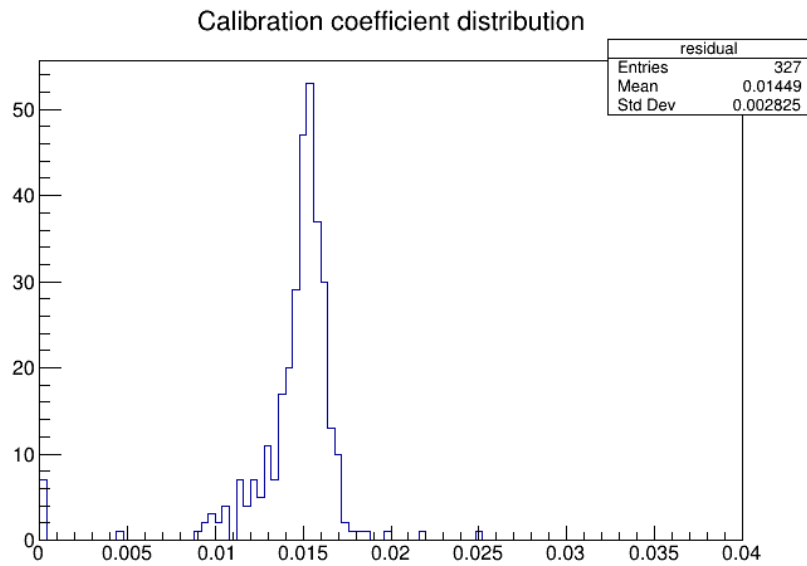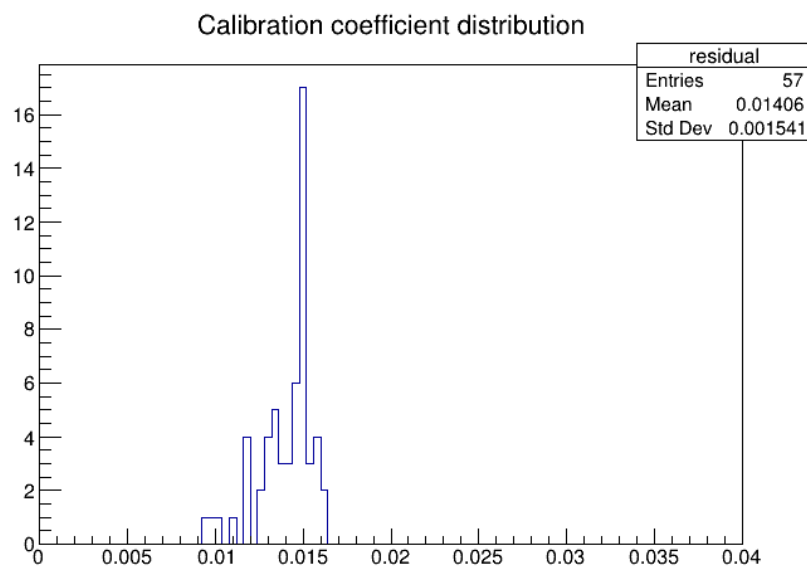
Figure 5.16: Distribution of the calibration coefficients in case of 5 cm side cubes (a) and 10 cm side cubes (b).

Figure 5.17: Overall GRAIN energy resolution σ_E/E plotted as a function of the reconstructed energy deposit. The points are fitted with the general expression for the energy resolution of eq. 5.3. The parameters $p0$, $p1$ and $p2$ correspond to factors a, b and c, respectively
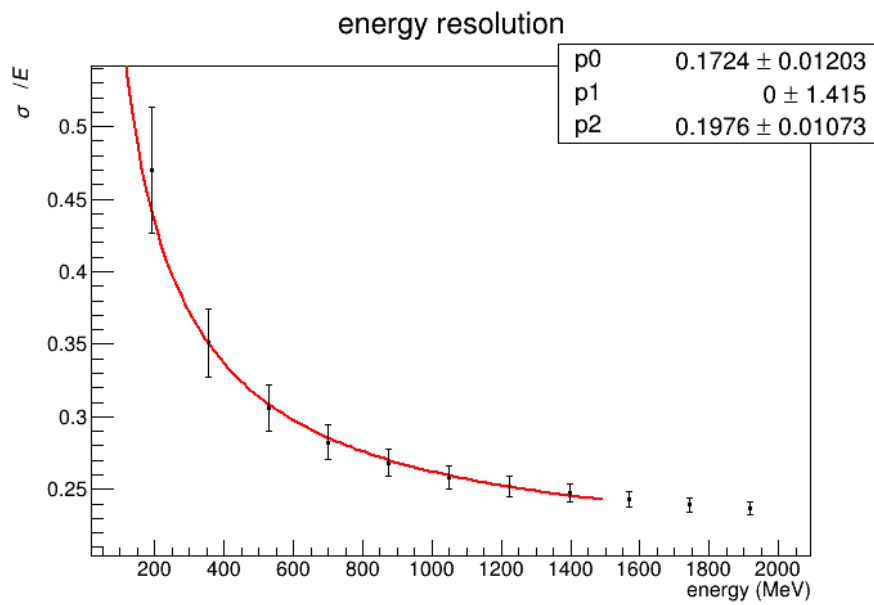
Conclusions and prospects

The next generation of long baseline neutrino experiments will play a key role in our understanding of the neutrino physics. One of them is DUNE, a dual-site experiment, which will study neutrino oscillations, having the main purpose of measuring the potential CP violating phase of the neutrino mixing matrix, together with the ordering of neutrino masses, the first of which would have a profound impact on the whole lepton sector of particle physics.

As part of the SAND detector of the DUNE ND complex, GRAIN will play an important role in the characterisation of the neutrino beam and in the improvement of LAr interaction models. GRAIN will take advantage of its granularity and fast response and contribute to the SAND physics case.

In this paper, a first quantitative assessment of neutrino event energy reconstruction performance for the mask system in GRAIN was performed. The possibilities of light yield reduction and usage of a new detector response software were first studied, comparing the output of each simulation with that of the Full Detector Response. The good agreement found between the Full and Fast-Calo responses allowed for a faster event simulation using the latter software.

The division of the GRAIN LAr volume into small cubes has been necessary to overcome the spatial dependence of the calibration coefficient. In particular, two different cube sizes were investigated: cubes of $5 \, \mathrm{cm}$ side allowed for a better spatial resolution, but with the limited data sample available, the measurement leaks from statistics; conversely, the $10 \, \mathrm{cm}$ cube side has been found to provide a much higher event number.

The validity of the reconstructed energy deposit by charged particles generated from neutrino events was tested and compared with the Monte Carlo truth taking into account the residual distribution, and a correspondence was found within 16%-18%. A detailed study on the effect of blinded cameras on the energy reconstruction, however, needs to be performed. Furthermore, a possible deviation from linearity has been found around $\sim 1.6 \, \mathrm{GeV}$ between the number of detected photons and the energy deposited in LAr. Its existence and origin will have to be carefully investigated.

The spatial dependence of the calibration coefficients has shown to be not so prominent, with a mean value of $0.014 \pm 0.003 \mathrm{MeV/photons}$. This opens up the possibility of an energy reconstruction independent of the track reconstruction *i.e.* from knowledge of

the trajectory of the particles and/or the location of the interaction vertex in the LAr vessel.

From these consideration, an overall energy resolution for the GRAIN detector has been finally computed:

$$\frac{\sigma_E}{E} = \frac{17\%}{\sqrt{E}} \oplus 20\%, \tag{5.2}$$

where the noise term is negligible.

The next steps to take to better analyse this reconstruction technique will be:

- study of the effect of blinded cameras on the energy reconstruction;

- investigation of the possible deviation from linearity between the number of detected photons and the energy deposited;

- use of the spatial information obtained from the 3D tracking algorithm to choose the exact calibration coefficient for the energy reconstruction.

Appendix A

Brief history of neutrinos

The neutrino was first theorised in 1930 by Wolfgang Pauli in order to account for the conservation of energy and momentum in beta decays. At the beginning, this process was thought to proceed as

$$_Z^A X \to_{Z+1}^A Y + e^-$$
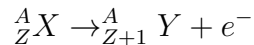
However looking at the energy spectrum of emitted electrons (Fig. A.1) it was clear that it was due to a three body process, but then a particle was missing. For a two body decay the electrons' energy spectrum should form a sharp peak around

$$E = \left(\frac{m_A^2 - m_B^2 + m_e^2}{2m_A} \right) c^2 \tag{A.1}$$

Instead, this energy corresponds only to the maximum electron energy in Figure A.1.

The problem of missing energy could be solved by introducing a new particle, which had to be neutral to conserve electric charge and extremely light, due to the fact that the observed electron energies range up to the value given in Equation (A.1). Fermi called this particle *neutrino*. A first estimate of the cross section of the inverse interaction was (Bethe and Peierls)[48]:

$$\sigma(\bar{\nu}p \to ne^+) \leq 10^{-44} \text{cm}^2, \quad E_\nu \simeq 2\,\text{MeV} \tag{A.2}$$

The smallness of the cross section led physicists to conclude that it would be almost impossible to detect such an interaction. Bruno Pontecorvo was the first to realise that with a neutrino flux of about $10^{11}\text{cm}^2/\text{s}$, on the order of the one produced by an average nuclear reactor, and a ton mass scale detector, one could obtain a rate of a few events per day [25].

Indeed, in 1956 Cowan and Reines discovered the antineutrino at the Savannah River nuclear reactor in South Carolina [42]. Their technique for the identification of the antineutrino inverse beta decay interactions relied on the detection of the light produced
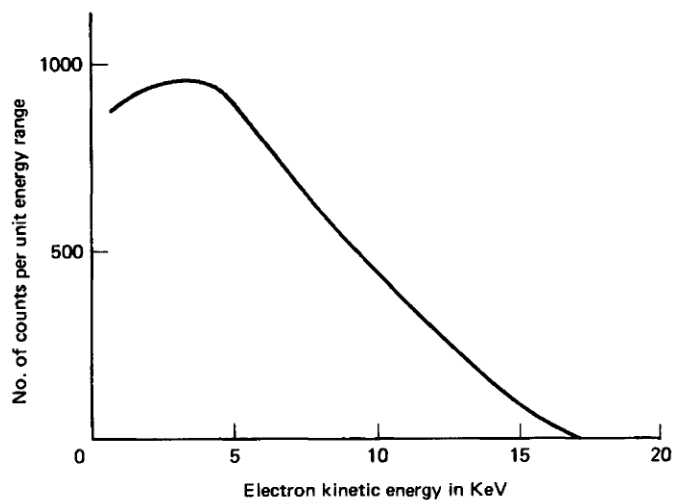
Figure A.1: The beta decay spectrum of tritium ($^3_1 H \rightarrow ^3_2 He$). *Source*: G.M. Lewis, *Neutrinos* (London: Wykeham, 1970)

by the neutron capture in delay with respect to the annihilation of the positron, a signature still in use today.

Nowadays we know the existence of three flavours of neutrinos, associated with the corresponding charged leptons, as shown in Table A.1 [37]. Leptons in the table above

Lepton	Charge	Mean life (s)	Mass (MeV)
e^-	$-e$	∞	0.511
ν_e	0		0
μ^-	$-e$	$2.197 \cdot 10^{-6}$	105.658
ν_μ	0		0
τ^-	$-e$	$(291.0 \pm 1.5) \cdot 10^{-15}$	1777
ν_τ	0		0

Table A.1: Leptons.

all have Total Lepton Number $L = +1$, while their antiparticles have $L = -1$, together with opposite electric charge.

An interesting feature of weak interactions is that parity is not conserved. Indeed, it was demonstrated by Madame Wu in 1957 that only left-handed components of electrons and neutrinos participate in weak processes, and the same is true for other flavours. Conversely antiparticles enter in interactions with right-handed components.

According to the Standard Model (SM) neutrinos are *massless* fermions. On the other hand, as we will discuss in more detail in Section 1.2, the observations of Neutrino Flavour

81

Oscillations by experiments operating in many different regimes have since proven that the mass of these particles is indeed non-zero. While the measurement of the absolute values of neutrino masses is still an open problem, the available upper limits are so much smaller than the masses of the other fundamental fermions that their *natural* production mechanism is thought to be of a non-Standard Model origin.

Neutrinos can thus be an handle with which to probe beyond the Standard Model physics: flavour oscillations represent the first hint for such a theory, and the searches for neutrinoless double β-decay might provide additional evidence by proving the Majorana nature of neutrinos and the non Standard Model origin of their masses.

Appendix B

Origin of neutrino masses

The SM Lagrangian does not allow for a mass term such as $\bar{e}_L e_R + h.c.$, since it would spoil the symmetry invariance under $SU(2)_L \times U(1)_Y$. However, when this group symmetry is broken, masses can be produced through the Brout-Englert-Higgs (BEH) mechanism. Considering a Yukawa-type coupling of the lepton $SU_L(2)$ doublet to a scalar field Φ, when the field acquires a vacuum expectation value v it is possible to built the Lagrangian

$$\mathcal{L}_H = - \sum_{\alpha,\beta=e,\mu,\tau} Y^{\prime l}_{\alpha\beta} \bar{\psi}_{\alpha L} \Phi l'_{\beta R} + h.c., \tag{B.1}$$

where $\psi_{\alpha L}$ are the left-handed lepton isospin doublets while

$$\Phi = \frac{1}{\sqrt{2}} \begin{pmatrix} 0 \\ v+h \end{pmatrix}. \tag{B.2}$$

Rewriting the Lagrangian, one gets

$$\mathcal{L}_H = -\frac{v+h}{\sqrt{2}} \left(\bar{l}'_L Y'^l l'_R + h.c \right). \tag{B.3}$$

with $l'_{L,R}$ being the chiral lepton array.

The matrices of Yukawa couplings $Y i^l$ and Y'^ν can then be diagonalized:

$$V_L^{l\dagger} Y'^l V_R^l = Y^l, \quad \text{with} \quad Y^l_{\alpha\beta} = y^l_\alpha \delta_{\alpha\beta} \quad (\alpha, \beta = e, \mu, \tau)$$

with real and positive y^l_α and y^l_k and V_L^l, V_R^l being appropriate 3×3 unitary matrices. In order to be definite mass states, the lepton fields must have a diagonalized Yukawa Lagrangian; thus, *massive lepton fields* can be defined as:

$$l_L = V_L^{l\dagger} l'_L = \begin{pmatrix} e_L \\ \mu_L \\ \tau_L \end{pmatrix}, \qquad\qquad l_R = V_R^{l\dagger} l'_R = \begin{pmatrix} e_R \\ \mu_R \\ \tau_R \end{pmatrix}$$

leading to the diagonalized Higgs-lepton Yukawa Lagrangian:

$$
\begin{aligned}
\mathcal{L}_H &= -\frac{v+h}{\sqrt{2}}\left(\bar{l}_L Y^l l_R + h.c.\right) \\
&= -\frac{v+h}{\sqrt{2}} \sum_{\alpha,\beta=e,\mu,\tau} y_\alpha^l\left(\bar{l}_{\alpha L} l_{\alpha R} + h.c\right).
\end{aligned}
\tag{B.4}
$$

which contains the Dirac mass term m_α for the charged lepton fields $l_\alpha = l_{\alpha L} + l_{\alpha R}$:

$$
m_\alpha = \frac{y_\alpha^l v}{\sqrt{2}} \quad (\alpha = e, \mu, \tau).
\tag{B.5}
$$

The discovery of neutrino oscillations has additionally established one of the core aspects of neutrino physics: neutrinos have a non-zero mass. Indeed flavour mixing and thus oscillations require neutrino mass terms that feature the flavour fields or a combination of them.

B.1 Dirac neutrinos

The simplest extension to the Standard Model that can accommodate neutrino mixing is the introduction of the right-handed components of the flavour neutrino fields, $\nu_{\alpha R}$. They are called *sterile* neutrinos, since they are singlets under the whole gauge group and are not interacting with all other particles. In this so-called minimally extended Standard Model the asymmetry between the lepton and quark sector due to the absence of RH neutrino fields is eliminated, and Dirac mass terms for neutrinos are generated through the Brout-Englert-Higgs mechanism as with the other fundamental fermions.

$$
\mathcal{L}_{mass}^{Dirac} = m_D(\bar{\psi}_L \psi_R + \bar{\psi}_R \psi_L)
\tag{B.6}
$$

where $\psi_{L(R)}$ is the left(right)-handed chiral component of the Dirac spinor ψ. The SM Higgs-lepton Yukawa Lagrangian now takes the form:

$$
\mathcal{L}_H = -\sum_{\alpha,\beta=e,\mu,\tau} Y_{\alpha\beta}'^l \bar{\psi}_{\alpha L} \Phi l_{\beta R}' - \sum_{\alpha,\beta=e,\mu,\tau} Y_{\alpha\beta}'^\nu \bar{\psi}_{\alpha L} \tilde{\Phi} \nu_{\beta R}' + h.c.,
\tag{B.7}
$$

where $\psi_{\alpha L}$ are the left-handed lepton isospin doublets while

$$
\tilde{\Phi} = i\sigma_2 \Phi^* = \frac{1}{\sqrt{2}}\begin{pmatrix} v+h \\ 0 \end{pmatrix}.
\tag{B.8}
$$

Performing the same operations as before the matrices of Yukawa couplings Yi^l and Y'^ν can be diagonalized:

$$
V_L^{l\dagger} Y'^l V_R^l = Y^l, \quad \text{with} \quad Y_{\alpha\beta}^l = y_\alpha^l \delta_{\alpha\beta} \quad (\alpha,\beta = e,\mu,\tau)
$$

and
$$V_L^{\nu\dagger} Y'^\nu V_R^\nu = Y^\nu, \quad \text{with} \quad Y_{\alpha\beta}^\nu = y_\alpha^\nu \delta_{\alpha\beta} \quad (k,j = 1,2,3).$$

Transforming the leptonic fields as follows,

$$l_L = V_L^{l\dagger} l_L' = \begin{pmatrix} e_L \\ \mu_L \\ \tau_L \end{pmatrix}, \qquad\qquad l_R = V_R^{l\dagger} l_R' = \begin{pmatrix} e_R \\ \mu_R \\ \tau_R \end{pmatrix}$$

$$n_L = V_L^{\nu\dagger} \nu_L' = \begin{pmatrix} \nu_{1L} \\ \nu_{2L} \\ \nu_{3L} \end{pmatrix}, \qquad\qquad n_R = V_R^{\nu\dagger} \nu_R' = \begin{pmatrix} \nu_{1R} \\ \nu_{2R} \\ \nu_{3R} \end{pmatrix}$$

leads to the diagonalized Higgs-lepton Yukawa Lagrangian:

$$\begin{aligned}
\mathcal{L}_H &= -\left(\frac{v+h}{\sqrt{2}}\right)\left[\bar{l}_L Y^l l_R + \bar{n}_L Y^\nu n_R\right] + h.c. \\
&= -\left(\frac{v+h}{\sqrt{2}}\right)\left[\sum_{\alpha,\beta=e,\mu,\tau} y_\alpha^l \bar{l}_{\alpha L} l_{\alpha R} + \sum_{k=1}^3 y_K^\nu \bar{\nu}_{kL} \nu_{kR}\right] + h.c..
\end{aligned} \tag{B.9}$$

The neutrino masses for the fields $\nu_k = \nu_{kL} + \nu_{kR}$ are given by:

$$m_k = \frac{y_k^l v}{\sqrt{2}} \quad (k = 1,2,3). \tag{B.10}$$

Although this mechanism of generation of neutrino masses is legitimate, if we look at the value of the Yukawa coupling g_{ν_e}, it is many orders of magnitude smaller than the couplings for the other fermions [58]:

$$2 \cdot 10^{-13} \leq g_{\nu_e} \leq 10^{-12} \qquad \text{while} \quad g_t \simeq 7 \cdot 10^{-1}, \quad g_b \simeq 2 \cdot 10^{-2}, \quad g_\tau \simeq 7 \cdot 10^{-3}$$

It looks extremely implausible that they have a common origin. This is also true if we think about smallness of neutrino masses: even if their absolute values are still unknown from neutrino oscillation and cosmological data the mass of the heaviest neutrino has been estimated to be

$$5 \cdot 10^{-2} eV \simeq \left(\sqrt{\Delta m_A^2}\right) \leq m_3 \leq \left(\frac{1}{3}\sum_i m_i\right) \simeq 3 \cdot 10^{-1} eV$$

where Δm_A^2 is the atmosphere neutrino mass-squared difference [58]. Another possibility is the method of the effective Lagrangian which, after SSB generates Majorana neutrinos with definite masses and suppression via seesaw mechanism of neutrino masses with respect to SM masses of leptons and quarks.

B.2 Majorana Neutrinos

As we saw, Dirac mechanism for neutrino masses is not a completely exhaustive model. A new beyond-the-Standard Model theory has been developed trying to account for neutrino masses generation in a more natural way. To be precise there is not a single theory but many [26, 58, 29]. One of the most popular is the Weinberg effective Lagrangian: it allows the introduction of neutrino masses using only left-handed (Majorana) neutrino fields.

In order to build a Lorentz invariant mass term, a product of left-handed and right-handed components is required; this is achieved by the fact that the charge conjugated field

$$\nu_{eL}^c = C\bar{\nu}_{eL}^T \tag{B.11}$$

is right-handed. A generic Majorana mass term may be written as

$$-\frac{1}{2}m_M\bar{\nu}_{eL}\nu_{eL}^c + h.c. \tag{B.12}$$

It is straightforward to see that the above mass term is not invariant under a global $U(1)$ transformation

$$\nu_{eL} \to e^{-i\theta}\nu_{eL} \tag{B.13}$$

corresponding to the non conservation of lepton number L. Considering all neutrino flavors the Majorana mass term has the form

$$\mathcal{L}^M = -\frac{1}{2}\bar{\nu}_L M^M \nu_L^c + h.c. \tag{B.14}$$

where M^M is a complex 3×3 matrix. It can be diagonalized by the transformation $M^M = UmU^T$, with $UU^\dagger = 1$ and $m_{ik} = m_i\delta_{ik}$, $m_i > 0$. Lagrangian B.14 thus becomes

$$\mathcal{L}^M = -\frac{1}{2}\sum_{i=1}^{3} m_i\bar{\nu}_i\nu_i \tag{B.15}$$

where ν_i are mass eigenstates with eigenvalues m_i.

$$\nu_i = \sum_l U_{il}^\dagger \nu_{lL} + \sum_l \left(U_{il}^\dagger \nu_{lL}\right)^c \tag{B.16}$$

It's straightforward to verify that the field ν_i satisfies Majorana condition $\nu_i = \nu_i^c$, and that the flavor neutrino fields ν_{lL} are given by a superposition of mass eigenstates ν_i, whose contributions are weighted by coefficients U_{il}.

$$\nu_{lL} = \sum_{i=1}^{3} U_{li}\nu_{iL} \tag{B.17}$$

The matrix U is called Pontecorvo-Maki-Nakagawa-Sakata (PMNS) matrix.

B.2.1 Type-I seesaw mechanism

The Standard Model for three generations of neutrinos can be extended to contain m right-handed neutrinos ν_R building a gauge invariant renormalizable Lagrangian $\mathcal{L} = \mathcal{L}_{SM} + \mathcal{L}_{\nu_R}$

$$\mathcal{L} = i\bar{\nu}_L\gamma^\mu\partial_\mu\nu_L + i\bar{\nu}_R\gamma^\mu\partial_\mu\nu_R - \bar{\nu}_L M_D \nu_R - \frac{1}{2}\bar{\nu}_L^c M_L \nu_L - \frac{1}{2}\bar{\nu}_R^c M_R \nu_R + h.c. \qquad (B.18)$$

It contains a $m\times 3$ complex Dirac mass matrix M_D together with Majorana mass matrices M_L and M_R for left-handed and right-handed neutrinos, which are respectively $m \times m$ and 3×3 symmetric matrices [49]. Notice that Majorana mass terms are not produced through SM Higgs mechanism and SSB. Writing the complete mass term for $3 + m$ neutrino generations results in

$$\mathcal{L}_{mass} = -\frac{1}{2}\begin{pmatrix} \bar{\nu}_L & \bar{\nu}_R^c \end{pmatrix} \begin{pmatrix} M_L & M_D \\ M_D^T & M_N \end{pmatrix} \begin{pmatrix} \nu_L^c \\ \nu_R \end{pmatrix} + h.c. \qquad (B.19)$$

where $\nu = (\nu_L, \nu_R^c)^T$ is a $(3 + m)$-dimensional vector. Since the Majorana mass term for LH neutrinos is forbidden from SM gauge invariance, it is physically reasonable to choose $M_L = 0$.

The mass matrix can be diagonalized by unitary matrix U to give $3 + m$ mass eigenstates. If the mass eigenvalues of M_R are much higher than the scale of electroweak symmetry breaking v, we obtain three light neutrinos ν_l and m heavy neutrinos, N.

$$U^T \begin{pmatrix} 0 & M_D \\ M_D^T & M_R \end{pmatrix} U = \begin{pmatrix} M_l & 0 \\ 0 & M_h \end{pmatrix} \qquad (B.20)$$

$$\mathcal{L}_{mass} = -\frac{1}{2}\bar{\nu}_l M^l \nu_l - \frac{1}{2}\bar{N} M^h N \qquad (B.21)$$

where M_l and M_h are 3×3 and $m \times m$ real diagonal matrices.

In this way values for LH neutrino masses compatible with experimental bounds are obtained.

The main experimental technique used today to confirm whether neutrinos are Majorana particles or more canonical Dirac fermions is the search for the neutrino-less double beta decay, a process which is possible only if neutrinos and antineutrinos are the same particle. Some of the experiments now active in the field include CUORE, CUPID and Gerda. [38, 4, 30].

Appendix C

Neutrino oscillation experiments: an insight

C.1 Solar experiments

The Sun produces an intense flux of neutrinos as a sub-product of some of the thermonuclear reactions that produce energy burning hydrogen into helium. The main reactions which can produce neutrinos are displayed in Table C.1. Neutrinos can travel directly

Reaction	Label	Flux($cm^{-2}s^{-1}$)
$p + p \longrightarrow {}^2H + e^- + \nu_e$	pp	5.95×10^{10}
$p + e^- + p \longrightarrow {}^2H + \nu_e$	pep	1.40×10^8
${}^3He + p \longrightarrow {}^4He + e^+ + \nu_e$	hep	29.3×10^3
${}^7Be + e^- \longrightarrow {}^7Li + \nu_e$	${}^7Be$	4.77×10^9
${}^8B \longrightarrow {}^8Be^* + e^+ + \nu_e$	${}^8B$	5.05×10^6

Table C.1: Neutrino production from fusion reactions in the Sun. The total solar flux at the Earth is 6.5×10^{10} neutrinos per cm^2 and per second.

from the core of the Sun to the Earth in a few minutes and hence provide a direct way to study processes by which protons form helium in the Sun. Despite the huge neutrino flux (almost 10^{11}!) the detection proved a formidable challenge because of the very small scattering cross section of neutrinos on ordinary matter.

The detailed prediction of the electron neutrino flux created by the thermonuclear reactions in the interior of the Sun follows the Standard Solar Model (SSM). The solar neutrino spectra predicted by the SSM are shown in Figure C.1.

Solar neutrino experiments are sensitive to the Δm_{12}^2 squared mass difference and to $sin2\theta_{12}$, which for this reason are referred to as *solar* mass difference and *solar* mixing
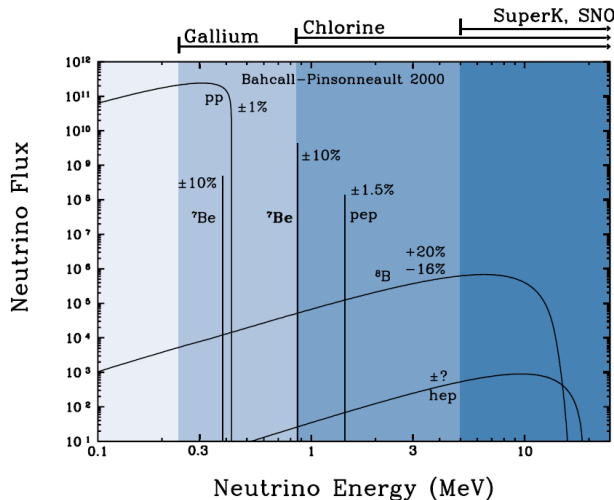
88

Figure C.1: The solar neutrino spectra predicted by the SSM. Courtesy of J.N. Bahcall from http://www.sns.ias.edu/ jnb/.

angle. These experiments can be divided into two main categories depending on the revelation techniques: radiochemical and Cherenkov.

To the first field belong experiments such as Homestake, Gallex/GNO [12, 15] and Sage, which exploit the Inverse Beta Decay reaction of solar neutrino with ^{37}Cl, ^{71}Ga and ^{71}Ge respectively. These experiments have a quite low energy threshold but they are not able to give any information on direction, energy or time of events. Among the experiments which use the Cherenkov technique we can find Kamiokande and Super-Kamiokande [22, 11], together with SNO [5, 6].

The Kamiokande experiment has been the first to exploit the Cherenkov technique. It consisted of a tank of about 3000 tons of pure water and 1000 photomultipliers positioned on the inner walls. The experiment observed the Cherenkov light produced by recoil electrons in elastic scattering (ES) interactions $\nu_x + e^- \to \nu_x + e^-$, which have an energy threshold of $E \geq 5\,\mathrm{MeV}$. Light water detectors are mainly sensitive to ν_e, but also to ν_μ and ν_τ, with a reduced cross section ($\sigma(\nu_\mu, \nu_\tau) \simeq 0.15\sigma(\nu_e)$).

The main advantage of the Kamiokande detector is the real-time nature of the neutrino interactions viewed in the active fiducial volume together with the possibility of reconstructing direction and energy, since neutrino elastic scattering processes preserve directionality.

The Kamiokande Collaboration demonstrated that solar neutrinos actually come from the direction of the Sun by reconstructing the direction of flight of the incident neutrinos. The data collected also confirmed the existence of the so called *solar neutrino problem*, a deficit in the number of neutrinos arriving from the Sun between 1/2 and 2/3 with respect to the predictions of the SSM, measured by the earlier radiochemical experiments.

The SNO experiment improved ν detection capability using heavy-water (d_2O) rather than purified water as target. This allowed to have access to two more reactions [18]:

$$(\text{CC}) \qquad \nu_e + d \rightarrow p + p + e^-; \qquad E \geq 5\,\text{MeV} \tag{C.1}$$

$$(\text{NC}) \qquad \nu_x + d \rightarrow p + n + \nu_x; \qquad f = e, \mu, \tau \qquad E \geq 2.2\,\text{MeV} \tag{C.2}$$

The first reaction being sensitive only to ν_e while the second to all flavours.

The important result of SNO was the that the combined tau and mu fluxes were found to be two times more intense than the ν_e one and that the total flux was in agreement with the predictions from the SSM. This is shown in Figure 1.6.

Another important and more recent Solar experiment is Borexino, which was the first with an energy threshold low enough to measure the monochromatic flux of ^{7}Be and *pep* neutrinos.

C.2 Atmospheric experiments

Atmospheric experiments exploit the production of neutrinos form the decay of mesons (pions and Kaons) resulting from cosmic ray interactions with the atmosphere. K and π decays give mainly ν_μ's while μ decay gives both ν_μ's and ν_e's. At low energy (below $2\,\text{GeV}$ where all of the muons decay before hitting the earth), the flux of each flavour neutrino occurs in the ratio

$$R = \frac{\Phi(\nu_\mu + \bar{\nu}_\mu)}{\Phi(\nu_e + \bar{\nu}_e)} \sim 2 \tag{C.3}$$

It is possible to distinguish two types of experimental set-up to detect atmospheric neutrinos. Experiments such as Soudan2 and Macro use iron calorimeters, constituted of layers of iron, acting as a passive material and active plastic scintillators layers. The active layers are able to track either the electromagnetic showers produced by $e^\pm$ or long muon tracks. The Super Kamiokande experiment instead exploit Cherenkov emission. A large tank of water of the order of $1\,\text{t}$ is surrounded by photomultipliers; analysing the rings produced by Cherenkov light it is possible to discriminate the flavour of the incoming neutrino.

The measurements of the iron calorimeters performed in the 80's and 90's noticed a noticeable ν_μ deficit and a value of R below unity. These observations were later confirmed in 1998 by Super Kamiokande. In the Multi-GeV data of SK, there was also a zenith angle distribution consistent with neutrino oscillation, since the variation of the flux is a function of the energy and zenith angle or, equivalently, of the L/E travelled by the parent neutrino.

Super Kamiokande showed that while electron events had no reduction, the muon events had a deficit of almost 50% for up-going neutrinos. These results can be explained if they are considered due to neutrino oscillation phenomena driven by the parameters
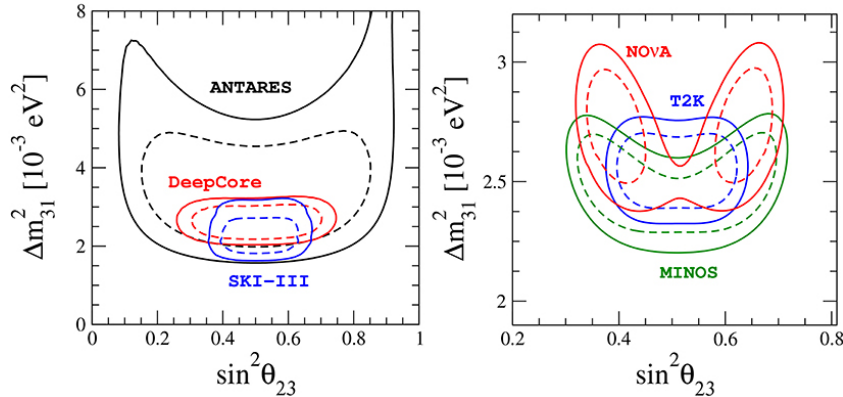
Figure C.2: 90% C.L. (straight line) and 99% (dashed line) C.L. allowed regions at the $\sin 2\theta_{23}$ - Δm_{31}^2 plane obtained from the atmospheric (left) and long–baseline accelerator experiments (right). Both plots correspond to the normal ordered neutrino mass spectrum [17].

Δm_{23}^2 and θ_{23} which, for this reason, are often referred to as *atmospheric* oscillation parameters. The best fit values for these parameters are today given by combining the results of Super Kamiokande with the ones from modern neutrino telescopes ANTARES and IceCube (Figure C.2).

C.3 Reactor experiments

Reactor neutrinos have been an important tool for both the discovery and precision measurement in the history of neutrino studies. Since the first generation of reactor neutrino experiments in the 1950s, the detector technology has been greatly advanced. The current reactor experiments have led neutrino physics into the precision era. Among them we can count Long Baseline Experiments, like KamLAND, and Short Baseline Experiments such as Daya Bay, Double Chooz, and RENO.

Neutrinos from nuclear reactors are $\bar{\nu}_e$ with energy of the order of the MeV. This makes the particles above threshold for electronic CC interactions, but not for other flavours, which means that, if the neutrino oscillates, CC interactions cannot happen. Reactor experiments can then measure the disappearance probability of the $\bar{\nu}_e$ and they are usually sensitive to small values of Δm^2 due to the low energy spectrum of the neutrinos.

In KamLAND, the 1000 t liquid scintillator detector measured the interactions of $\bar{\nu}_e$ from a cluster of nuclear reactors located $\simeq 175$ km far away. The antineutrinos interact via inverse beta decay at an energy threshold of $E > 2.6$ MeV:

$$\bar{\nu}_e + p \rightarrow e^+ + n \quad E > 2.7\,\text{MeV} \tag{C.4}$$

Short Baseline Experiments have been able to measure the disappearance of reactor electron antineutrinos at distances of about 1 km. Their characteristics made them sensitive to the measurement of the θ_{13} mixing angle.

In the next future reactor experiment will be a key player in determining neutrino mass ordering and precision measurement of θ_{12}, Δm_{32}^2, and Δm_{31}^2 to sub-percent level.

C.4 Accelerator experiments

In this kind of experiments neutrinos are generated using a proton beam impinging on a target producing secondary mesons (pions and Kaons) which are let decay to obtain a beam of neutrinos (mainly ν_μ). The produced beam is monitored by a near detector, usually few tents of meters far apart from the production hall.

Among accelerator experiments, K2K (KEK to Kamioka) in Japan and MINOS at Fermilab were the first to confirm the atmospheric oscillation results. K2K used a beam of about 98% ν_μ with a mean energy of about 1.3 GeV produced from 12 GeV protons accelerated at the KEK synchrotron. The experiment had a near detector at about 300 m from the proton target, and used Super-Kamiokande as its far detector at about 250 km. MINOS also looked for ν_μ disappearance using the NuMi neutrino beam at $E \sim 3\,\text{GeV}$. Similarly to K2K it had a near detector at about 1 km from the source and a second detector in the Soudan mines at about 735 km away as its far detector. The first results published in 2006, combined with the ones from K2K first confirmed neutrino oscillations at 5σ.

The successor of K2K, T2K (Tokai to Kamioka) used a muon neutrino ($E \simeq 0.6\,\text{GeV}$) beam and, together with the NoVA experiment, was able to perform precision measurements on atmospheric parameters $\sin 2\theta_{23}$ and Δm_{31}^2, in both appearance and disappearance channels.

T2K in particular strongly restricted the range of values of the CP-violating phase δ, excluding the values of 0 and π values at 95% confidence level (see Figure 1.7).

Bibliography

[1] A. Himpsl et al. A. Neumeier T. Dandl. "Attenuation of vacuum ultraviolet light in pure and xenon-doped liquid argon —an approach to an assignment of the near-infrared emission from the mixture". In: *EPL (Europhysics Letters)* 111 (2015), p. 12001. URL: https://doi.org/10.1209/0295-5075/111/12001.

[2] S.L. Adler. "Tests of the Conserved Vector Current and Partially Conserved Axial-Vector Current Hypotheses in High-Energy Neutrino Reactions". In: *Phys. Rev.* 136 (1964), B963–B966.

[3] A. Salleh et al. "Triroc, a versatile 64-channel SiPM readout ASIC for time-of-flight PET". In: *2016 IEEE Nuclear Science Symposium, Medical Imaging Conference and Room-Temperature Semiconductor Detector Workshop (NSS/MIC/RTSD)*. 2016, pp. 1–5. DOI: 10.1109/NSSMIC.2016.8069882.

[4] Azzolini O. et al. *Final result of CUPID-0 phase-I in the search for the ^{82}Se*. 2019. arXiv: 1906.05001v1.

[5] B. Aharmim et al. "Electron energy spectra, fluxes, and day-night asymmetries of B-8 solar neutrinos from measurements with NaCl dissolved in the heavy-water detector at the Sudbury Neutrino Observatory". In: *Phys. Rev. C* 72 (2005), p. 055502. DOI: 10.1103/PhysRevC.72.055502.

[6] B. Aharmim et al. "Measurement of the ν_e and Total ^{8}B Solar Neutrino Fluxes with the Sudbury Neutrino Observatory Phase-III Data Set". In: *Phys. Rev. C* 87.1 (2013), p. 015502. DOI: 10.1103/PhysRevC.87.015502.

[7] B. Aimard et al. "A 4 tonne demonstrator for large-scale dual-phase liquid argon time projection chambers". In: *Journal of Instrumentation* 13.11 (2018), P11003–P11003. DOI: 10.1088/1748-0221/13/11/p11003. URL: https://doi.org/10.1088/1748-0221/13/11/p11003.

[8] B.T. Cleveland et al. "Measurement of the Solar Electron Neutrino Flux with the Homestake Chlorine Detector". In: *Astrophysical Journal* 496 (1998), pp. 505–526.

[9] C. Adams et al. "The Long-Baseline Neutrino Experiment: Exploring Fundamental Symmetries of the Universe". In: *Snowmass 2013*. Workshop on Energy Frontier. June 30-July 3, 2013.

[10] Costas Andreopoulos et al. *The GENIE Neutrino Monte Carlo Generator: Physics and User Manual*. 2015. arXiv: 1510.05494 [hep-ph].

[11] J. Hosaka et al. "Solar neutrino measurements in super-Kamiokande-I". In: *Phys. Rev. D* 73 (2006), p. 112001. DOI: 10.1103/PhysRevD.73.112001.

[12] J.N. Abdurashitov et al. "Solar neutrino flux measurements by the Soviet-American Gallium Experiment (SAGE) for half the 22 year solar cycle". In: *J. Exp. Theor. Phys.* 95 (2002), pp. 181–193. DOI: 10.1134/1.1506424.

[13] K.S. Babu et al. "Working Group Report: Baryon Number Violation". In: *Snowmass on the Mississippi*. Proceedings, 2013 Community Summer Study on the Future of U.S. Particle Physics. July 29-August 6, 2013. arXiv: 1311.5285 [hep-ph]. URL: http://www.slac.stanford.edu/econf/C1307292/docs/IntensityFrontier/BaryonNo-13.pdf.

[14] M. Adinolfi et al. "The KLOE electromagnetic calorimeter". In: *Nucl. Instrum. Meth.* A482 (2002), pp. 364–386.

[15] M. Altmann et al. "Complete results for ve years of GNO solar neutrino observations". In: *Phys. Lett. B* 616 (2005), pp. 174–190. DOI: 10.1016/j.physletb.2005.04.068.

[16] M. Babicz et al. "A measurement of the group velocity of scintillation light in liquid argon". In: *Journal of Instrumentation* 15.09 (2020), P09009–P09009. DOI: 10.1088/1748-0221/15/09/p09009. URL: https://doi.org/10.1088%2F1748-0221%2F15%2F09%2Fp09009.

[17] P.F. de Salas et al. "Status of neutrino oscillations". In: (2017). arXiv: 1708.01186.

[18] Q.R. Ahmad et al. "Direct evidence for neutrino flavor transformation from neutral current interactions in the Sudbury Neutrino Observatory". In: *Phys. Rev. Lett.* 89 (2002), p. 011301.

[19] R. Acciarri et al. *Long-Baseline Neutrino Facility (LBNF) and Deep Underground Neutrino Experiment (DUNE), Conceptual Design Report Volume 2: The Physics Program for DUNE at LBNF*. 2015.

[20] R. Francini et al. "VUV-Vis optical characterization of Tetraphenyl-butadiene films on glass and specular reflector substrates from room to liquid Argon temperature". In: *Journal of Instrumentation* 8.09 (2013), P09006–P09006. DOI: 10.1088/1748-0221/8/09/p09006. URL: https://doi.org/10.1088/1748-0221/8/09/p09006.

[21] T. Pershing et al. "Performance of Hamamatsu VUV4 SiPMs for detecting liquid argon scintillation". In: *Journal of Instrumentation* 17.04 (2022), P04017. DOI: 10.1088/1748-0221/17/04/p04017. URL: https://doi.org/10.1088/1748-0221/17/04/P04017.

[22] Y. Fukuda et al. "Solar neutrino data covering solar cycle 22". In: *Phys. Rev. D* 77 (1996), pp. 1683–1686. DOI: 10.1103/PhysRevLett.77.1683.

[23] D.Decamp et al. ALEPH Collaboration. In: *Phys. Lett. B* 235 (1990), p. 399.

[24] J. Calvo et al. ArDM collaboration. "Measurement of the attenuation length of argon scintillation light in the ArDM LAr TPC". In: *Astropart. Phys.* 97 (2018), pp. 186–196. URL: https://doi.org/10.1016/j.astropartphys.2017.11.009.

[25] B.Pontecorvo. "Inverse beta process". In: *Camb. Monogr. Part. Phys. Nucl. Phys. Cosmol.* 1 (1991), pp. 25–31.

[26] Gavela M.B. Broncano A. and Jenkins E. *The Effective Lagrangian for the Seesaw Model of Neutrino Mass and Leptogenesis.* 2006.

[27] G.O. Gann C. Benson and V. Gehman. "Measurements of the intrinsic quantum efficiency and absorption length of tetraphenyl butadiene thin films in the vacuum ultra-violet regime". In: *Eur. Phys. J. C* 78.329 (2018).

[28] C.W. Kim C. Giunti. *Fundamentals of Neutrino Physics and Astrophysics.* 2007.

[29] Li T. Cai Y. Han T. and Ruiz R. In: *Front. Phys.* 6 (2018), p. 40.

[30] Agostini M. (GERDA Collaboration). In: *Phys. Rev. Lett.* 125 (2020), p. 252502.

[31] DUNE Collaboration. *Deep Underground Neutrino Experiment (DUNE) Far Detector Technical Design Report Volume 1: Introduction to DUNE.* 2020. arXiv: 2002.02967v3 [physics.ins-det].

[32] DUNE Collaboration. *Deep Underground Neutrino Experiment (DUNE) Near Detector Conceptual Design Report.* 2021. arXiv: 2103.13910v1 [physics.ins-det].

[33] DUNE Collaboration. *Long-Baseline Neutrino Facility (LBNF) and Deep Underground Neutrino Experiment (DUNE) Conceptual Design Report Volume 3: Long-Baseline Neutrino Facility for DUNE.* 2015. arXiv: 1601.05823 [physics.ins-det].

[34] LBNE Collaboration. *The Long-Baseline Neutrino Experiment: Exploring Fundamental Symmetries of the Universe.* 2014. arXiv: 1307.7335 [hep-ex].

[35] The PIP-II Collaboration. *The PIP-II Reference Design Report.* 2015. URL: http://projectx-docdb.fnal.gov/cgi-bin/ShowDocument?docid=1370.

[36] The T2K Collaboration. In: *Nature* 580 (2020), p. 340.

[37] Greenwood D.A. Cottingham W.N. *An introduction to the Standard Model of Particle Physics. Second edition.* Cambridge University Press, 2007.

[38] Adams D.Q. et al. (CUORE Collaboration). *Improved Limit on Neutrinoless Double Beta Decay in ^{130}Te with CUORE.* 2019. arXiv: 1912.10966v1.

[39] M. Albertini D. Mary and C. Laurent. "Understanding optical emissions from electrically stressed insulating polymers: electroluminescence in poly(ethylene terephthalate) and poly(ethylene 2,6-naphthalate) films". In: *Journal of Physics D: Applied Physics* 30.2 (1997), pp. 171–184. DOI: 10.1088/0022-3727/30/2/004. URL: https://doi.org/10.1088/0022-3727/30/2/004.

[40] *edep-sim : An Energy Deposition Simulation.* https://github.com/ClarkMcGrew/edep-sim.

[41] E.E. Fenimore and T.M. Cannon. "Coded aperture imaging with uniformly redundant arrays". In: *Appl. Opt.* 17.3 (1978), pp. 337–347. DOI: 10.1364/AO.17.000337.

[42] F.Reines and C.L.Cowan. "The Neutrino". In: *Nature* 178 (1956), pp. 446–449.

[43] R. Lanou G. Seidel and W. Yao. "Rayleigh scattering in rare-gas liquids". In: *Nucl. Instrum. Meth.* A489 (2002), pp. 189–194. URL: https://doi.org/10.1016/S0168-9002(02)00890-2.

[44] Stephen Gottesman and E. Fenimore. "New family of binary arrays for coded aperture imaging". In: *Applied optics* 28 (1989), pp. 4344–4352. DOI: 10.1364/AO.28.004344.

[45] E. Grace and J.A. Nikkel. "Index of refraction, Rayleigh scattering length, and Sellmeier coefficients in solid and liquid argon and xenon". In: *Nucl. Instrum. Meth.* A867 (2017), pp. 204–208. URL: https://doi.org/10.1016/j.nima.2017.06.031.

[46] D.J. Gross and C.H. Llewellyn Smith. "High-energy neutrino - nucleon scattering, current algebra and partons". In: *Nucl. Phys.* B14 (1969), pp. 337–347.

[47] S.J. Parke H. Nunokawa and J.W. Valle. "CP Violation and Neutrino Oscillations". In: *Prog. Part. Nucl. Phys.* 60 (2008), pp. 338–402. arXiv: 0710.0554 [hep-ph].

[48] H.Bethe and R.Peierls. "The Neutrino". In: *Nature* 133 (1934), p. 532.

[49] Fujikawa K. In: *Eur. Phys. J. C* 80 (2020), p. 285.

[50] Ramshan Kugathasan. "A low-power mixed-signal ASIC for readout of SiPM at cryogenic temperature". In: *PoS* TWEPP2019 (2020), p. 011. DOI: 10.22323/1.370.0011.

[51] C. Lastoria. "Analysis of the light production and propagation in the 4-tonne dual-phase demonstrator". In: *Journal of Instrumentation* 15.06 (2020), pp. C06029–C06029. DOI: 10.1088/1748-0221/15/06/c06029. URL: https://doi.org/10.1088/1748-0221/15/06/c06029.

[52] W.J. Marciano and Z. Parsa. "Neutrino electron scattering theory". In: *J. Phys.* G29 (2003), pp. 2629–2645.

[53] S.P. Mikhaev and A.Y. Smirnov. In: *Sov.J.Nucl.Phys* 42 (1985), p. 913.

[54] K.A.A. Gamage M.J. Cieślak and Robert Glover. "Coded-aperture imaging systems: Past, present and future development - A review". In: *Radiation Measurements* 92 (2016), pp. 59–71. URL: https://doi.org/10.1016/j.radmeas.2016.08.002.

[55] M. Chen et al. N. Ishida. "Attenuation length measurements of scintillation light in liquid rare gases and their mixtures using an improved reflection suppresser". In: *Nucl. Instrum. Meth.* A384 (1997), pp. 204–208. URL: https://doi.org/10.1016/S0168-9002(96)00740-1.

[56] E. Segreto. "Evidence of delayed light emission of tetraphenyl-butadiene excited by liquid-argon scintillation light". In: *Phys. Rev. C* 91 (3 2015), p. 035503. DOI: 10.1103/PhysRevC.91.035503. URL: https://link.aps.org/doi/10.1103/PhysRevC.91.035503.

[57] E. Segreto. "Properties of Liquid Argon Scintillation Light Emission". In: *Phys. Rev. D* 103 (2021), p. 043001. arXiv: 2012.06527 [physics.ins-det]. URL: https://doi.org/10.1103/PhysRevD.103.043001.

[58] Bilenky S.M. *Neutrinos: Majorana or Dirac?* 2020. arXiv: 2008.02110v1.

[59] W. Walkowiak. "Drift velocity of free electrons in liquid argon". In: *Nuclear Instruments and Methods in Physics Research Section A: Accelerators, Spectrometers, Detectors and Associated Equipment* 449.1 (2000), pp. 288–294. ISSN: 0168-9002. DOI: https://doi.org/10.1016/S0168-9002(99)01301-7. URL: https://www.sciencedirect.com/science/article/pii/S0168900299013017.

[60] L. Wolfenstein. In: *Phys. Rev. D17* 2369 (1978).

[61] K. Zuber. *Neutrino Physics. Second edition.* 2011.